
Optical Characterisation of Metallic and Biological Nanoparticles

A PhD Thesis

by:

Fionnuala McGrath

Supervisor:

Prof. Louise Bradley



School of Physics

Trinity College Dublin

March 2023

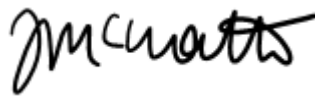
Declaration

I declare that this thesis has not been submitted as an exercise for a degree at this or any other university and it is entirely my own work with the exception of assistance and collaboration recognised in the acknowledgements and throughout the thesis where applicable.

I agree to deposit this thesis in the University's open access institutional repository or allow the library to do so on my behalf, subject to Irish Copyright Legislation and Trinity College Library conditions of use and acknowledgement.

I have read and I understand the plagiarism provisions in the General Regulations of the University Calendar for the current year, found at <http://www.tcd.ie/calendar>.

I have also completed the Online Tutorial on avoiding plagiarism "Ready Steady Write", located at <http://tcd-ie.libguides.com/plagiarism/ready-steady-write>.



Fionnuala McGrath

Acknowledgement

Firstly, I would like to thank my supervisor, Prof. Louise Bradley, for her support, encouragement and guidance, and for giving me the opportunity to finish my PhD. I would also like to thank all past and present member of her research group.

I would like to thank Prof. Deirdre O'Carroll of Rutgers University, New Jersey, for her input and expertise in metallic nanoparticles.

A special thanks to my office mates, Jing and Julia, and our honorary office mate, Carolyn. Thank you for all the lunch time laughs.

I would like to thank everyone in the School of Physics that made it possible for me to continue with my PhD.

Thank you to the Laboratory for Biological Characterisation of Advanced Materials (LBCAM), especially Prof. Adriele Prina-Mello, and Dr Melissa Anne Tutty, for their guidance and sample preparation.

Thank you to the staff in the Advanced Microscopy Lab for their technical support and assistance. Thank you to Alan O'Meara for his help with computer problems and Ken Concannon for always having a spare key whenever I put mine "somewhere safe".

I want to thank Ciara for keeping me supplied with coffee every week, and for all of our chats.

I would like to thank my family who have supported me throughout the years, and are always there for me.

Finally, I want to thank Andrew for his patience, support and encouragement over the last few years. I wouldn't have made it to the end of this PhD without him!

Thank you.

List of Publications and Conference Contributions

McGrath, F., O'Carroll, D., *"Green Photonic: Metasurface Photonic Materials for Thin-Film Energy Efficiency and Energy Harvesting Applications"*, presented at Rutgers University, New Brunswick, New Jersey, USA, March 2019.

McGrath, F., O'Carroll, D., *"Fabrication of metasurface thin films from silver ink and vacuum deposited silver"*, poster presentation at EMRS Spring Meeting, Nice, France, May 2019.

McGrath, F., O'Carroll, D. *"Fabrication and characterisation of metasurface thin films from silver inks and vacuum deposited silver"*, poster presentation at SPIE Optics + Photonics, San Diego, August 2019.

McGrath, F., et al., *"Structural, optical, and electrical properties of silver gratings prepared by nanoimprint lithography of nanoparticle ink"* Appl. Surf. Sci., vol. 537, p. 147892, Jan. 2021, doi: 10.1016/j.apsusc.2020.147892.

McGrath, F., Tutty, MA., Prina-Mello, A., Bradley, AL., *"Analysis of the Distribution of IR-Nanoparticles in 2D Monolayers and 3D Spheroids"*, Oral Presentation at Photonics Ireland 2021, online, June 2021.

McGrath, F., Bradley, AL., *"Optical Characterisation of Metallic and Biological Nanoparticles"*, Oral Presentation, Postgraduate Semain, School of Physics and CRANN, Trinity College Dublin, November 2021

McGrath, F., et al., *"Assessing Nanobiomaterial (NBM) Interaction and Internalisation in Three-Dimensional Hepatic Spheroid over Time Using Confocal Microscopy"*, Publication in preparation

List of Abbreviations and Conventions

2D	2-dimensional
3D	3-dimensional
Ab	Antibody
AFM	Atomic Force Microscopy
Ag	Silver
AgNPI	Silver Nanoparticle Ink
AuNP	Gold Nanoparticle
BFM	Bright-field Microscopy
BSE	Backscatter Electrons
CCD	Charged Couple Device
CD	Compact Disc
CTCF	Corrected Total Cell Fluorescence
DI	Deionised Water
DLS	Dynamic Light Scattering
DMEM	Dulbecco's Modified Eagle Medium
EEO	Electroendosmosis
EM	Electromagnetic
ESEM	Environmental Scanning Electron Microscopy
EtOH	Ethanol
EUNCL	European Nanomedicine Characterisation Laboratory
FBS	Foetal Bovine Serum
FIB	Focused Ion Beam
Flrpic	bis[2-(4,6-difluorophenyl)pyridinato-C ₂ N](picolinato)iridium(III)
FLIM	fluorescence lifetime imaging microscopy
GPC	Gas Permeation Chromatography
H&E	Haematoxylin and Eosin
HCL	Hydrochloric acid
HepG2	Hepatocellular Carcinoma Cell Line
HPLC	High-Performance Liquid Chromatography
IMS	Industrial Methylated Spirits
IPA	Isopropanol
IR780	Infrared 780
LBCAM	Laboratory for Biological Characterization of Advanced Materials
LSPR	Localised Surface Plasmon Resonance
NA	Numerical Aperture
NBM	Nanobiomaterial
NIL	Nanoimprint Lithography
NP	Nanoparticle
NR668	Nile Red 668
NTA	Nanoparticle Tracking Analysis
PACA	Poly(ethyl-butyl cyanoacrylate)
PBS	Phosphate Buffer Saline
PDMS	Polydimethylsiloxane

PEBCA	Poly(ethyl-butyl cyanoacrylate)
PFA	Paraformaldehyde
PL	Photoluminescence
PMMA	Poly(methylmethacrylate)
P-OLED	P-Organic Light Emitting Diode
PTFE	Polytetrafluoroethylene
PVK	Poly(9-vinylcarbazole)
PX	Pixel
RPM	Revolutions per Minute
RT	Room Temperature
SE	Secondary Electrons
SEM	Scanning Electron Microscope
SPAD	Single Photon Avalanche Diode
TCSPC	Time correlated
TE	Thermal evaporation
UV	Ultra violet

Abstract

Nanotechnology is a rapidly growing technology with applications that affect many industries in the global economy. Two such industries are optoelectronics and healthcare.

With the increased demand for smaller, more efficient, and more affordable device, there is also an increased need for smaller optoelectronic components. In this work, fabrication of metasurfaces using a solution-based nanoimprint lithography process is investigated. The properties of silver nanoparticle ink grating and planar samples, with and without a PMMA layers, are compared with thermally evaporated silver on a nanoimprinted PMMA layers. The grating pattern is successfully fabricated using nanoimprint lithography with the silver nanoparticle ink directly on a glass substrate and on a PMMA layer. The use of PMMA was found to adversely affect the structural, optical and electrical properties of the silver nanoparticle planar surfaces and gratings. Gratings nanoimprinted directly into silver nanoparticle ink on a glass substrate were found to have similar performance to gratings produced by thermal evaporation of silver on nanoimprinted PMMA and benefit from an easier fabrication process. The silver nanoparticle ink shows promise for the fabrication of patterned silver thin films and may be useful for upscaling and roll-to-roll processes.

The application of nanotechnology in medicine, nanomedicine, is an area of technology where there have been significant breakthroughs. Nanobiomaterials (NBM) are studied extensively within nanomedicine with applications in drug delivery, contact tracing, deep-tissue imaging, and the detection and treatment of diseases. Pre-clinical assessment is an important step in the development of new NBMs to examine the toxicity of the NBMs. The current state-of-the-art to assess toxicity is to use two-dimensional (2D) cell cultures. These *in vitro* 2D assays lack the physiological process present in *in vivo* models. However, toxicity observed in *in vivo* animal models is not always observed in humans, and can make predicting possible interactions difficult. Three-dimensional (3D) *in vitro* models are currently being investigated as possible alternatives to 2D *in vitro* and *in vivo* animal models. These 3D models, or spheroids, are more biological relevant than their 2D predecessors, with some studies using them in pre-clinical investigations to examine dosing effects of nanoparticles.

In this work, two NBMs, LipImage™815, a liposome loaded with a near infrared dye (IR780), and PACA(NR668), a polymeric shell loaded with far red dye (NR668), are investigated. Using confocal microscopy, a powerful fluorescence imaging modality, the translocation and penetration of the NBMs into the spheroid is assessed. The initial work is carried out over a 72 h period using one concentration for each NBM. Fluorescence intensity is observed decreasing at treatments times of up to 72 h, for both NBMs. However, the rate at which they penetrate to the core, and become homogenous differs for both NBMs. Fluorescence Lifetime Imaging Microscopy (FLIM) also showed that concentration, treatment time and translocation have no effect on the lifetime of the NBMs, suggesting the decrease in intensity observed at longer treatment times is due to degradation of the liposome or polymeric shell, and quenching of the encapsulated dyes.

Contents

Declaration	i
Acknowledgement	iii
List of Publications and Conference Contributions	iv
List of Abbreviations and Conventions	v
Abstract	vii
Contents	ix
List of Figures.....	xii
List of Tables	xv
List of Equations	xvi
Chapter 1 Introduction	1
1.1. Metallic Nanoparticles	2
1.2. Nanobiomaterials	4
1.3. Thesis Structure	6
Chapter 2 Techniques and Methods	9
2.1. Nanoimprint Lithography	10
2.2. Scanning Electron Microscopy (SEM).....	12
2.3. Atomic Force Microscopy	13
2.4. UV/Visible Spectroscopy	15
2.5. Localised Surface Plasmon Resonance.....	15
2.6. Nanobiomaterials	15
2.7. Spheroids	17
2.8. Fluorescence.....	18
Chapter 3 Structural, optical, and electrical properties of silver grating prepared by nanoimprint lithography of nanoparticle ink	23
3.1. Materials and Methods	23
3.1.1. Materials for fabrication of gratings and planar silver nanostructures	23

3.1.2. Methods.....	24
3.2. Characterisation.....	36
3.3. Results and Discussion.....	40
3.3.1. Structural Characterisation.....	40
3.3.2. Optical Characterisation.....	45
3.3.3. Electrical Characterisation.....	50
3.4. Conclusion.....	51

Chapter 4 Assessing Nanobiomaterial (NBM) Interactions and Trafficking in Three-Dimensional Hepatic Spheroids over Time Using Confocal Microscopy . 53

4.1. Materials and Methods.....	54
4.1.1. Chemicals.....	55
4.1.2. NBM Preparation.....	55
4.1.3. NBM Characterisation.....	56
4.1.4. Cell Culture.....	56
4.1.5. Cultivation of HepG2 Cells and Preparation of HepG2 Spheroids.....	57
4.1.6. Morphological Assessment of HepG2 Spheroids.....	57
4.1.7. Exposure to NBMs.....	59
4.1.8. Immunofluorescent Staining.....	59
4.1.9. Confocal Microscopy.....	60
4.1.10. Fluorescence Lifetime Imaging Microscopy.....	63
4.2. Results and Discussion.....	64
4.2.1. Characterization of NBMs.....	64
4.2.1.1. Hydrodynamic Diameter.....	65
4.2.1.2. HepG2 spheroid culture and characterisation.....	66
4.2.3. Liposome Stability.....	67
4.2.4. Direct Imaging Method Validation.....	70
4.2.5. Confocal Images.....	73
4.2.6. Distribution of NBMs in HepG2 Spheroids.....	75

4.2.7. Fluorescence Lifetime Imaging Microscopy	81
4.3. Conclusion	84
Chapter 5 Assessing the Effects of Concentration on Nanobiomaterial (NBM) Interactions and Trafficking in Three-Dimensional Hepatic Spheroids	87
5.1. Materials and Methods	88
5.2. Results and Discussion	88
5.2.1. Bright-field microscopy.....	88
5.2.2. Confocal Microscopy.....	89
5.2.3. Distribution of NBMs in HepG2 Spheroids	94
5.2.4. Fluorescence Lifetime Imaging Microscopy.....	101
5.3. Diffusion	107
5.4. Conclusion	110
Chapter 6 Conclusion and Future Work.....	113
6.1. Future Work.....	115
References	117
Appendix A.....	137
1. A.1 – Text file to Tiff Image (Intensity and Lifetime).....	137
2. A.2 – Image Stitcher	140

List of Figures

Figure 1.1. Nanoparticle size comparison to common molecules.....	1
Figure 1.2. Nanoparticles and nanobiomaterials.....	2
Figure 2.1. Optical metasurfaces	9
Figure 2.2. Schematic of a nanoimprint lithography process.....	10
Figure 2.3. Schematic of a top-emitting, inverted P-OLED.....	11
Figure 2.4. Scanning Electron Microscope (SEM).....	12
Figure 2.5. Schematic of Atomic Force Microscopy.....	14
Figure 2.6. Schematic of localised plasmon resonance in a metallic nanoparticle.	15
Figure 2.7. The electromagnetic (EM) spectrum.....	18
Figure 2.8. The Jablonski diagram.	19
Figure 2.9. Normalised absorption/emission spectra of the NMB LipImage.....	20
Figure 2.10. Schematic of MicroTime200	21
Figure 2.11. A schematic of time-correlated single photon counting (TCSPC)	22
Figure 3.1. Schematic of a cross-section of a CD.....	25
Figure 3.2. Bright-field microscopy.....	26
Figure 3.3. Fabrication of PDMS mould.	26
Figure 3.4. Schematic of NIL process for fabrication of AgNPI gratings, using method (1).....	27
Figure 3.5. Bright-field images of grating patterns during testing phase.....	29
Figure 3.6. Thermal shock of AgNPI thin film.....	30
Figure 3.7. Silver ink grating on a glass substrate	30
Figure 3.8. Schematic of the NIL process for fabrication of an AgNPI planar surface using method (1).....	31
Figure 3.9. Schematic of the NIL process for fabrication of an AgNPI grating, using method (2).....	32
Figure 3.10. Schematic of the NIL process for fabrication of an AgNPI planar surface, using method (2).....	33
Figure 3.11. Schematic of the conventional NIL process for fabrication of an Ag grating using method (3).....	34
Figure 3.12. Schematic of the conventional NIL process for fabrication of an Ag planar surface using method (3).....	35
Figure 3.13. Optical characterisation	37

Figure 3.14. UV/Visible set up.....	38
Figure 3.15. Structural characterisation.....	39
Figure 3.16. Electrical characterisation.....	40
Figure 3.17. Scanning Electron Microscopy.....	42
Figure 3.18. Focused Ion Beam (FIB)	42
Figure 3.19. AFM 3D Representations.....	43
Figure 3.20. AFM Line Profiles	44
Figure 3.21. Schematic of Silver Grating on a glass substrate.....	44
Figure 3.22. UV/Visible Reflectance and Absorbance spectra.....	46
Figure 3.23. Angle Resolved Reflectance Spectroscopy.	48
Figure 3.24. Photoluminescence Maps.....	49
Figure 3.25. Photoluminescence Spectra.....	50
Figure 4.1. Schematic of HepG2 spheroid formation in CellStar® cell repellent plates.	57
Figure 4.2. Internal spheroid structure and morphology	59
Figure 4.3. Schematic of spheroid (blue), and imaging plane (orange)	61
Figure 4.4. Flow Chart describing the treatment of images.....	62
Figure 4.5. Photobleaching effect on LipImage.....	63
Figure 4.6. Residual trace from exponential decay nonlinear curve fit.....	64
Figure 4.7. Representative Bright-field microscopy image of HepG2 spheroid.....	67
Figure 4.8. Custom built slide position locator	69
Figure 4.9. Fluorescence intensity measurements of 2D monolayers of HepG2 cells	70
Figure 4.10. Fluorescent Labelling vs Direct Imaging.....	71
Figure 4.11. Excitation and emission spectra for Alexa Fluor-488 and LipImage.	72
Figure 4.12. Validation of direct imaging	73
Figure 4.13. Colour confocal images	74
Figure 4.14. Colour confocal images	75
Figure 4.15. Stitched, normalised intensity images of LipImage and PACA.....	77
Figure 4.16. Fluorescence intensity of whole spheroid.....	78
Figure 4.17. A line plot from periphery through the core of the spheroid.....	79
Figure 4.18. Colour maps representing normalised NBM translocation and penetration.....	81
Figure 4.19. Fluorescence Lifetime Decay Curves	82
Figure 4.20. Fluorescence lifetime decay curves	83

Figure 5.1. Representative bright-field images of HepG2 spheroids.....	89
Figure 5.2. Colour confocal images of spheroids.....	90
Figure 5.3. Colour confocal images of spheroids.....	91
Figure 5.4. Colour confocal images of spheroids.....	92
Figure 5.5. Colour confocal images of spheroids.....	93
Figure 5.6. Stitched, normalised intensity images of LipImage treated spheroids.....	95
Figure 5.7. Stitched, normalised intensity images of PACA treated spheroids	96
Figure 5.8. Integrated intensity for LipImage, and PACA	97
Figure 5.9. Colourmaps representing normalised LipImage translocation.....	98
Figure 5.10. Colourmaps representing normalised PACA translocation.....	100
Figure 5.11. Fluorescence lifetime decay curves	103
Figure 5.12. Fluorescence Lifetime Decay Curves for LipImage at the core and periphery.....	104
Figure 5.13. Fluorescence Lifetime Decay Curves for PACA at the core and periphery	106

List of Tables

Table 3.1. Parameters explored for ideal annealing conditions of AgNPI.....	28
Table 3.2 Average Measurements for Grating Obtained from Line Profiles.....	45
Table 3.3. Conductivity Measurements for surfaces fabricated using AgNPI and NIL.	50
Table 3.4. Conductivity measurements for surfaces fabricated using a conventional method.	51
Table 4.1 Immunofluorescent Stains used for confocal microscopy.	60
Table 4.2 Summary and comparison of characterization data by NTA and DLS for LipImage.	65
Table 4.3. Summary and comparison of characterization data by NTA and DLS for PACA.	66
Table 4.4. Table of Data obtained from fitted graphs.	82
Table 5.1. NBMs used in this work. Spheroids were exposed to each NBM for up to 72 h, at different concentrations.	88
Table 5.2. Table of data obtained from normalised fitted fluorescence lifetime decay graphs for LipImage, using a one-exponential fit, where τ_1 is the average decay.	102
Table 5.3. Table of data obtained from normalised, fitted fluorescence lifetime decay graphs for PACA.....	102
Table 5.4. Table of data obtained from normalised, fitted fluorescence lifetime decay graphs for LipImage	105
Table 5.5. Table of data obtained from normalised, fitted fluorescence lifetime decay graphs for PACA.....	107

List of Equations

$F = k\Delta z$	Equation 2.1	13
$Dt = TkB3\pi\eta d$	Equation 2.2.....	16
$\Delta\lambda = \lambda_{\text{em}} - \lambda_{\text{ab}}$	Equation 2.3	19
Airy Disc (μm) = $0.8\lambda \times \text{N.A.}$	Equation 2.4.....	21
$A = 1 - (R + T)$	Equation 3.1.....	38
$R = n - 12 + k2n + 12 + k2$	Equation 3.2	45
$y = y_0 + A_1e^{-x\tau_1}$	Equation 4.1	63
$y = y_0 + A_1e^{-x\tau_1} + A_2e^{-x\tau_2}$	Equation 4.2	63
$\tau_{\text{average}} = A_1\tau_1 + A_2\tau_2$	Equation 4.3.....	64
$\tau_{\text{average}} = A_1\tau_1^2 + A_2\tau_2^2$	Equation 4.4	64
$\text{CTCF} = \text{IC} - \text{ACIB}$	Equation 4.5	68

Chapter 1 Introduction

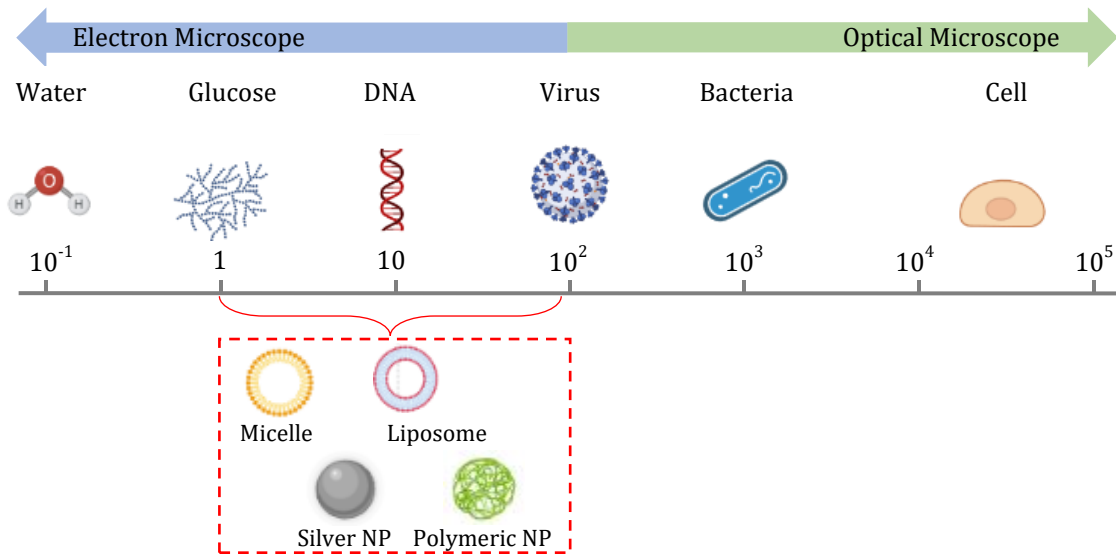


Figure 1.1. Nanoparticle size comparison to common molecules. The NPs and NBMs used in this body of work, i.e., silver NP, liposomes and polymeric NPs, compared to the size of other, common molecules, such as DNA, viruses, cells and bacteria. Figure created using Biorender.

Nanotechnology is a rapidly growing technology with applications that affect many industries in the global economy. The current market value of nanotechnology is expected to exceed \$125 billion by 2024 [1]. Nanomaterials, which includes nanoparticles (NPs) and nanobiomaterials (NBMs) account for \$7.3 billion of the market, with the expectation that it will grow to \$16.8 billion by the end of 2022, due to the demand for smaller, more efficient and more affordable devices and materials [2]. NPs, and NBMs are small particles, their sizes compared to common molecules which can be seen in Figure 1.1. NPs and NBMs have precise nanoarchitectures and nanostructures that allow their magnetic, biological, optical, electrical, and mechanical properties to be tuned, allowing them to be used in a wide variety of fields, from engineering to food science, and cosmetics to medicine, as described in Figure 1.2 [3–5]. Two types of nanoparticles are studied in this thesis: Silver nanoparticle ink (AgNPI) is used to investigate a solution-processed method for the fabrication of

structured metallic which can be incorporated into optoelectronic devices; and dye loaded NBMs are examined in a three-dimensional (3D) in vitro model.

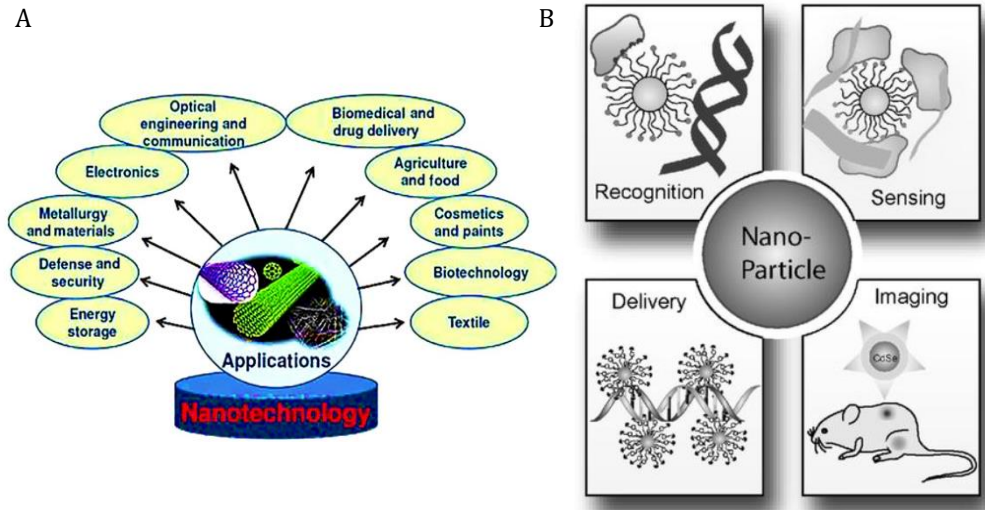


Figure 1.2. Nanoparticles and nanobiomaterials can be used in many different industries, from energy storage, to optical engineering to biomedical imaging and drug delivery. (A) taken from [3] and (B) taken from [4].

1.1. Metallic Nanoparticles

Controlling light, heat, and electricity has occupied human kind for most of our history. The knowledge that has been acquired in this quest has become the foundation of modern electrical and electromagnetic technology. Wireless technology, computers, lasers, and biosensors could not have been developed without the manipulation of light [6]. To achieve this, metasurfaces, which are lightweight, ultra-compact, and ultrathin, can be fabricated and incorporated into optoelectronic devices and biosensors, e.g., novel wave-guiding structures, solar cells, miniaturised cavity resonators, electronic switches, and biosensors to detect blood oxygen and glucose levels. The metasurfaces can be used to improve their efficiency, and overcome limitations of conventional optical devices [7–9]. A crucial part of achieving solar cells with efficiencies approaching the Shockley-Queisser limit, the theoretical upper limit of a solar cell, is efficient light trapping and harvesting. Textured surfaces and microlenses are used for both light trapping and light extraction, but these conventional methods are not suitable for use in organic optoelectronic devices due to the extreme thinness of the active layer used. In order to manage light within such thin active layers, the

development of appropriate plasmonic and photonic nanostructures is important. Currently there are few examples of light-trapping structures, other than randomly textured backreflectors, that are incorporated into commercially available solar cells. By fabricating metasurfaces from metallic nanoparticles and integrating the metasurfaces into thin-film, polymer photovoltaic devices, the LSPR can improve light absorption [10].

Metasurfaces are novel, nanostructured, thin-film, synthetic materials that can be used to manipulate and confine electromagnetic radiation. They are typically composed of arrays of subwavelength metallic or dielectric nanostructures [7,11]. The electromagnetic properties of the surfaces arise from the collective response of the individual nanostructures, which has led to some important optical phenomena, including negative refractive index, phase control and localised electromagnetic field enhancement. For practical applications it is important to understand how the properties of these metasurfaces can affect reflection, transmission and absorption in thin-film coatings.

To make metasurfaces commercially viable, using low-cost, and low-embodied energy materials to fabricate them is important. Current methods of fabrication can be expensive, time consuming, energy inefficient, and require specialised equipment, i.e., vacuum chamber, clean rooms, high precision, and highly trained personnel. These methods can also cause damage to surrounding areas of the surface. Fabrication methods include direct-write (electron-beam, focused ion beam, and laser), and pattern-transfer lithography [12–17]. Nanoimprint lithography (NIL) was introduced by Chou *et al.* [18] as a low-cost, high throughput alternative to UV-lithography, and other direct-write lithography processes for the fabrication of metasurfaces [19].

The conventional method of using NIL involves imprinting a mould into PMMA, and coating the transferred pattern with a thermally evaporated metal. However, this is not without challenges. It can be difficult to fabricate the high-resolution mould required for the pattern transfer, and a residual imprint layer can be left behind on the nanostructures.

To overcome some of these limitations, inkjet printing was introduced [20–22], using metallic inks to build up the desired patterns. Inkjet printing, like NIL, can be considered a cheap process. However, it is also not without its limitations, e.g., particles

can easily agglomerate, the nozzle can get plugged with larger particles, and the printed metal films can have high contact resistance due to poor film surface flatness. NIL has previously been used for the fabrication of nanostructures using metallic ink. However, in the past, the silver ink has been spin coated onto the mould, and imprinted onto the substrate using pressure. The sample is then demoulded and heat treated [23,24].

Metallic nanoparticles, such as gold, platinum, and silver, are interesting due to their unique properties, such as high thermal and electrical conductivity. Typically, the NPs have a spherical shape with diameters ranging from 5 nm to 100 nm, and can be suspended in aqueous or organic solvents, when used as inks. These inks can be used to print different shapes, periodic arrays, or high resolution electrodes [25–28] for use in complex electronic circuits, thin film resistors, solar cells [29], and are very useful for printed and flexible electronics [30].

In this thesis, a less intensive method for fabrication of silver gratings using silver nanoparticle ink and nanoimprint lithography was investigated. The properties of silver nanoparticle ink gratings and planar samples, with and without a PMMA layer, were compared with thermally evaporated silver on nanoimprinted PMMA. The grating pattern was successfully fabricated using nanoimprint lithography with the silver nanoparticle ink directly on a glass substrate and on a PMMA layer. It was found that the use of PMMA adversely affects the structural optical, and electrical properties of the silver nanoparticle planar surfaces and gratings. Gratings nanoimprinted directly into silver nanoparticle ink on a glass substrate are found to have similar performance to gratings produced by thermal evaporation of silver on nanoimprinted PMMA and incorporating a significantly easier fabrication process. The silver nanoparticle ink shows promise for the fabrication of patterned silver thin films and may be useful for upscaling and roll-to-roll processes, a process that could potentially meet the demands of the global nanotechnology industry's need for more affordable devices and materials.

1.2. Nanobiomaterials

Healthcare is an area where the application of nanotechnology has made significant breakthroughs. The application of nanotechnology in medicine, or nanomedicine, has been defined by the European Science Foundation as “the science and technology of diagnosing, treating, and preventing disease and traumatic injury, of relieving pain, and

of preserving and improving human health, using molecular tools and molecular knowledge of the human body” [31,32].

NBMs are studied extensively and widely used within nanomedicine, with applications ranging from drug delivery, to contact tracing and deep-tissue imaging [33–38]. NBMs can be synthesised from a vast array of materials, and in various morphologies and sizes, making them extremely diverse. However, despite this, a main limitation in nanomedicine research is the ability of NBMs to penetrate solid tumours. This is something which greatly limits their success in the clinic as antitumour agents and compromises their translation to viable medical products.

Another major obstacle in nanomedicine research to date has been the fact that the pre-clinical assessment of NBMs is mostly limited to conventional two-dimensional (2D) cell cultures, and whilst *in vitro* 2D cell-based assays have been the gold standard for nanomedicines for decades [39], they are highly simplistic and fall short in predicting not only toxicity, but also the fate of the NBMs in the body. This is due to their absence of physiological processes. For example, for *in vivo* models it is crucial to understand how NBMs are transported through the cell [40–43]. Significant cytotoxicity has been seen in 2D *in vitro* models after treatment with carbon nanotubes, quantum dots, and magnetic NPs. However, the same toxicity is not observed in animal models [44–46]. Consequently, there is a pressing need for a more biologically relevant and advanced models that can assess for cytotoxicity, and predict possible interactions in humans [47–49].

In recent years there has been a move toward three-dimensional (3D) *in vitro* models as an alternative to traditional 2D cell cultures. These models not only overcome some of the limitations observed with 2D cultures, but they are also far more biologically relevant and can potentially bridge the gap between the traditional 2D *in vitro* model, and *in vivo* animal work [48]. This also allows for compliance with the 3Rs concept of reduction, refinement, and replacement with regard to *in vivo* animal experimentation. Much work is being undertaken to standardise and validate 3D models for assessing NBM toxicity. Some studies have used them in pre-clinical investigations where it was shown that spheroids are a useful tool to examine dosing effects of nanoparticles, and show great promise to assess the cytotoxicity of different metallic NPs [50–53].

When used for biomedical applications NBMs are required to undergo rigorous testing before being introduced to the human body, to evaluate their potential for causing adverse effects. As NBMs can be administered via several methods, e.g., IV injection, inhalation, ingestions, or dermal application, they have the potential to travel throughout the whole body, before accumulating in crucial secondary organs, such as the liver and spleen [54,55], where they may cause off-target side effects. As a consequence, their toxicity needs to be carefully examined. The liver is a heterogenous organ that has many functions, including protecting individuals from xenobiotic compound induced cellular injury or death. The liver's ability to perform these functions is due to its role in metabolism, clearance, and biotransformation of xenobiotic compounds, including NBMs. Therefore, an importance should be placed on 3D liver models for use in predicting human toxicity [56–58]. For these reasons, HepG2 cell, a hepatocellular carcinoma cell line, was used in this work, to culture 3D/hepatic spheroids.

In this work, confocal microscopy was used to investigate two NBMs representing candidates for specific application of medical technology, that is, their ability to penetrate and extravasate 3D *in vitro* models, or, spheroids. LipImage™815 (a liposome loaded with IR780), and PACANR668 (a polymeric NBM loaded with Nile Red 668) are the two selected NBMs. From single spheroids, without the need to fluorescently label the NBMs, quantitative localisation and penetrative information was obtained. Being able to image LipImage™815 without fluorescently labelling the NBM allows full advantage of the infrared-window to be facilitated, such as low signal to noise, low auto fluorescence and minimal damage to surrounding tissue, and suitability for deep tissue imaging.

Toxicity, although an important aspect of the NMB pre-clinical assessment, is outside the scope of this work.

1.3. Thesis Structure

The structure of this thesis is as follows: Chapter 1 begins with a general introduction into nanoparticles (NPs), and explores the different areas and industries where they are currently used and the two areas of interest in the work: thin film fabrication, and pre-clinical assessment using bioimaging.

Chapter 2, is a literature review of the techniques and methods used to characterise NPs and NBMs.

Chapter 3 examines metasurfaces fabricated from AgNPI. The structural, optical, and electrical properties of these surfaces are characterised and compared to conventionally fabricated surfaces of the same dimensions.

Chapter 4 focuses on bioimaging, by assessing the penetration and translocation of two NBMs in a 3D *in vitro* model.

Chapter 5 expands on the experimental design of Chapter 4 to evaluate if similar results can be obtained using a lower and higher concentration of the NBMs.

A summary of the results is presented in Chapter 6, with comments on suggested future work.

Chapter 2 Techniques and Methods

With increasing demand for smaller, more efficient, and more affordable devices, there is also an increased need for smaller optoelectronic components. Metasurfaces (two-dimensional nanostructured photonic materials) are emerging as a likely candidate to solve this problem. Metasurfaces are comprised of arrays of nanostructures which make it possible for them to manipulate light on the nanoscale, shown in Figure 2.1. Nanostructure arrays are typically composed of metallic or dielectric materials [6,7,59,60]. Phase control, negative refractive index, and localised electromagnetic field enhancements have been reported using their collective response [61–64]. To make metasurfaces commercially viable, using low-cost, low-embodied-energy materials and fabrication processes is important. Using plasmonic, i.e., metallic, metasurfaces has been proposed for improving light management in thin-film semiconductor optoelectronic devices, with some recent research showing promise [65–67], e.g., light-emitting transistors [68], and solar cells [69,70].

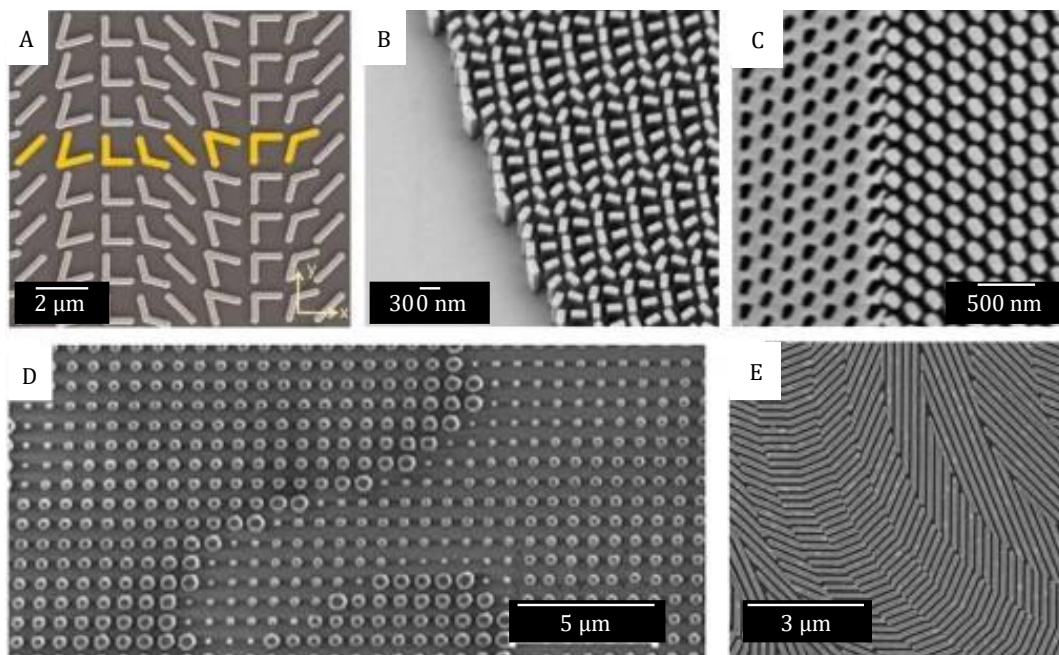


Figure 2.1. Optical metasurfaces. These are some examples of different optical metasurfaces that have been used for different applications: (A) Gold antenna array, (B) TiO_2 nanofins on a glass substrate, (C) Achromatic metalens, (D) Silicon posts on SiO_2 , and (E) Silicon nanobeams. Image modified from [59].

The use of metallic ink has been previously used in the fabrication of metasurfaces using different techniques, such as ink jet printing and direct imprint using ultraviolet curing [71–73]. Nanoimprint Lithography (NIL) uses a direct imprint method, and address the need for low-cost, low-energy fabrication process. Using a metallic ink allows for a solution-based metasurface fabrication method and in combination with NIL can produce a scalable, high-throughput technique, with potential use in a roll-to-roll fabrication method, making it a commercially viable technique [74–76].

2.1. Nanoimprint Lithography

NIL was introduced by Chou et. al. [77] as a low-cost, high-throughput alternative to UV-lithography. Figure 2.2 shows a schematic illustration of the NIL process. Here, an SiO₂ grating pattern is attached to a Silicon surface (1. Initial Setup). The pattern is then embedded into a poly(methylmethacrylate) (PMMA) surface, and thereafter cured (2. Nanoimprinting). The mould is then removed and a PMMA metasurface is exposed (3. Mould Removal). The PMMA is then coated, under vacuum, with a thermally evaporated metal, creating plasmonic metasurfaces.

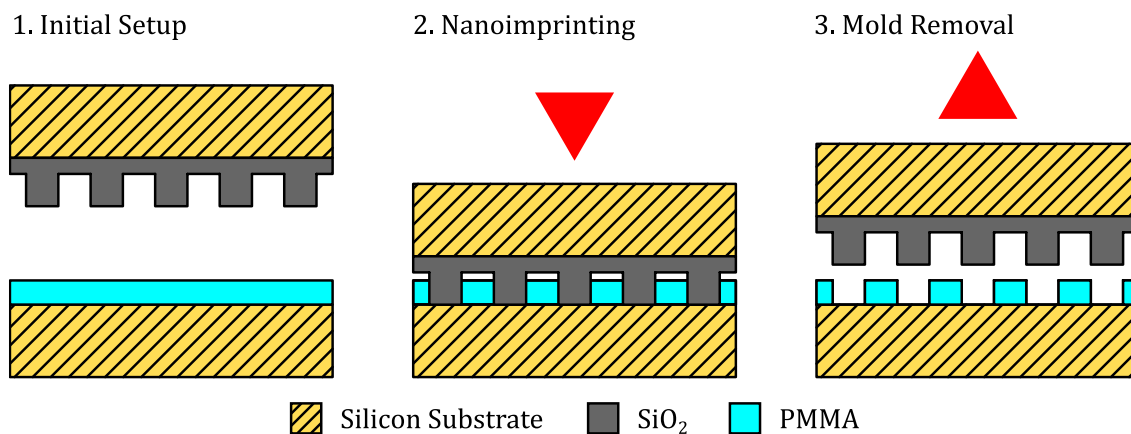


Figure 2.2. Schematic of a nanoimprint lithography process. A mould with (1) a metasurface pattern is (2) embedded in a PMMA layer, heat treated, and (3) the mould is removed. To create plasmonic metasurfaces the PMMA mould is subsequently subjected to thermal evaporation of a metal.

To make this fabrication low-cost, a metallic ink can replace the PMMA layer. The patterned mould can then be imprinted directly into the metallic ink to produce plasmonic metasurfaces [78–81]. The advantage of using a metallic ink over PMMA and thermal evaporation is to eliminate the vacuum requirements from manufacturing [82]. Using nanoparticle ink allows for control over the absorption of the surface, with

larger nanoparticles absorbing more light than smaller nanoparticles [83]. In this work, silver nanoparticle ink (AgNPI) is used. Although Ag can tarnish over time, it is anticipated that the surfaces fabricated using NIL and AgNPI will be inserted into optoelectronic devices that will be encapsulated, limiting exposure to air [84]. Figure 2.3 shows a schematic illustration of a top-emitting P-Organic Light Emitting Diode (P-OLED). The P-OLED shows an example of how the Ag layer can be incorporated into a device, with an encapsulation layer on the top of the device to limit the exposure of the Ag layer to air.

Metasurfaces can influence the absorption and emission of light, therefore, the properties of metasurfaces need to be fully understood. Characterisation of the structure and the optical properties of the plasmonic metasurfaces should be carried out. Current state-of-the-art structural characterisation techniques include scanning electron microscopy (SEM), atomic force microscopy (AFM), and focused ion beam (FIB) milling.

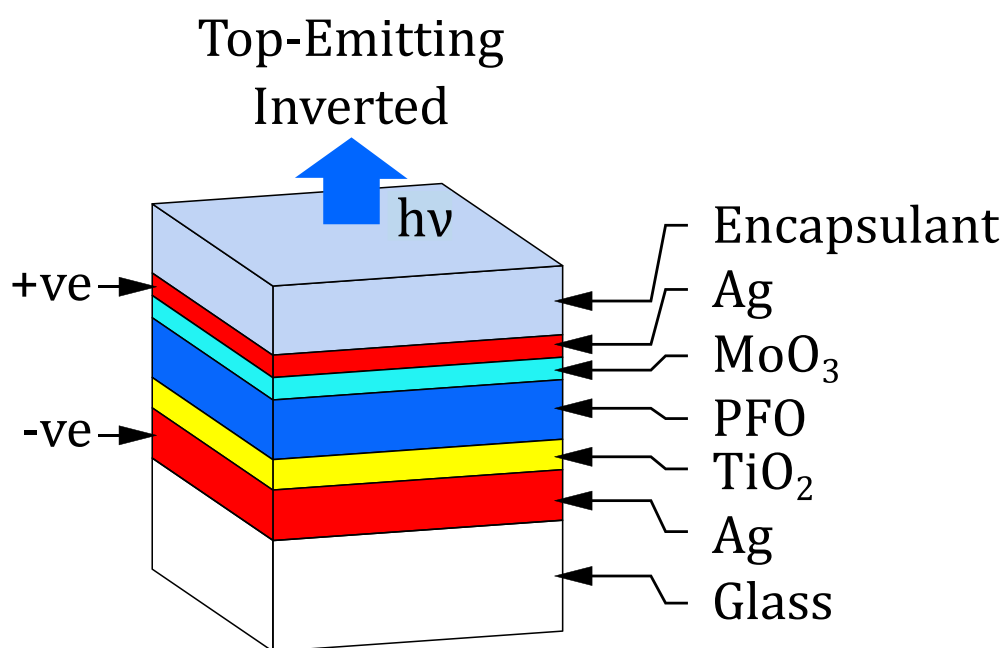


Figure 2.3. Schematic of a top-emitting, inverted P-OLED. The P-OLED is an example of a thin film optoelectronic, that has an Ag layer. In this work, the Ag layer is fabricated using a metallic AgNPI. The encapsulation layer at the top prevents the silver layer from tarnishing. Schematic taken and amended from [84].

2.2. Scanning Electron Microscopy (SEM)

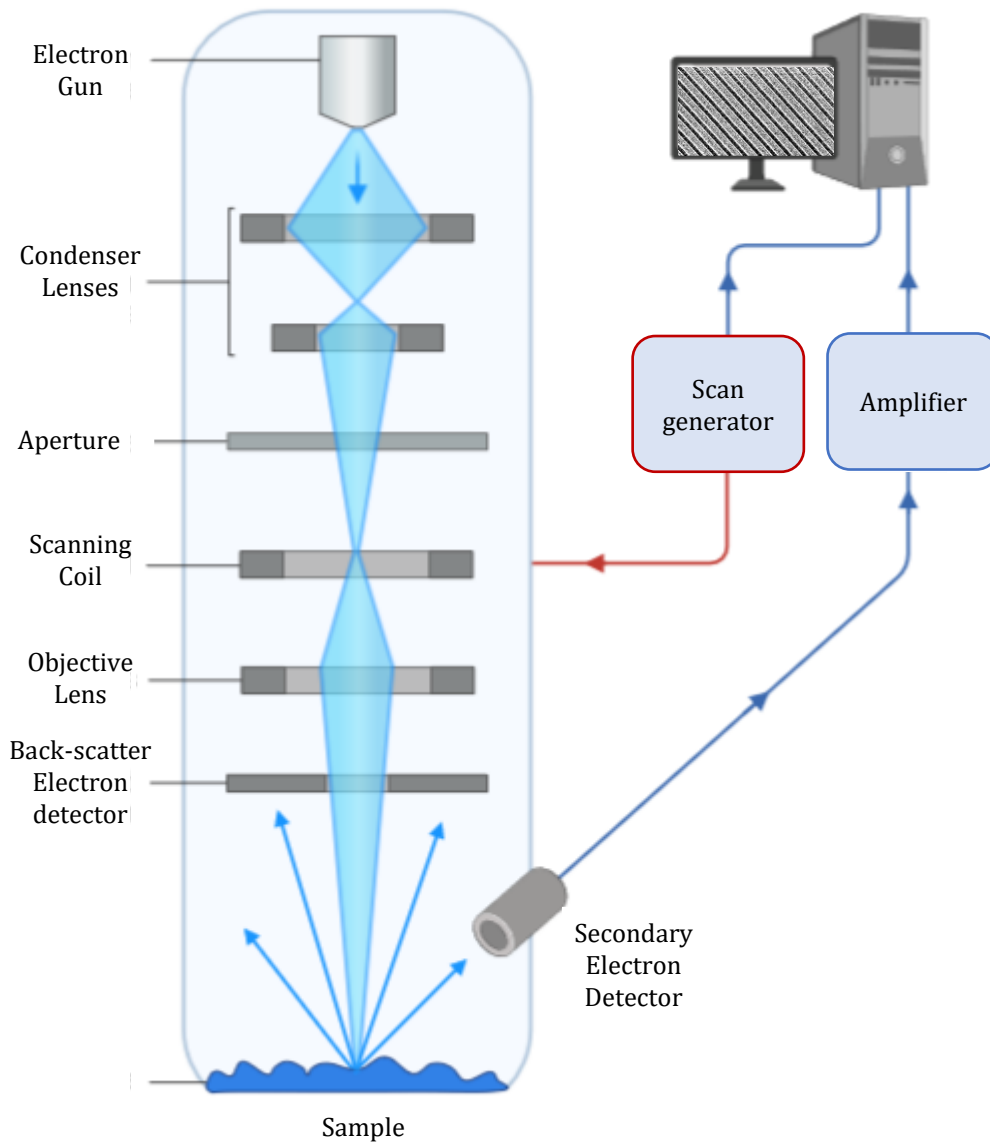


Figure 2.4. Scanning Electron Microscope (SEM). A sample is placed in a vacuum chamber, where, using a focused electron beam, an image is generated by detecting the secondary or back-scatter electrons, emitted from the sample, with a resolution down to the nanometre scale. Samples must be conductive. This image was taken from Biorender and modified.

Structural characterisation is important when assessing the performance of a plasmonic metasurface. State of the art structural characterisation of surfaces is carried out using SEM [85–89], which has a resolution on the nanometre scale.

To create an image using SEM (Zeiss Ultra *plus*), the sample must have a conductive surface. The SEM uses electrons from an electron gun guided towards the sample surface. When the beam reaches the sample surface they produce X-rays, backscattered

electrons (BSE), and secondary electrons (SE), all of which can be detected and analysed, depending on the information required from the sample. X-ray detection is used for chemical composition of the sample. For image analysis backscattered electron detection and secondary electron detection is used. Backscattered electrons are elastic interactions between the electron beam and the sample, that come from relatively deep within the sample. Secondary electrons are inelastic interactions between the beam and the sample, which originate from the surface of the sample [90]. Figure 2.4 shows a schematic of an SEM, the different lenses and detectors, and the backscatter and secondary electrons that are used to form images.

2.3. Atomic Force Microscopy

Another high resolution scanning technique is atomic force microscopy (AFM) (AFM Asylum MFP-3D). AFM can be used for measuring, and manipulating matter at the nanoscale. It is mainly used to obtain spatially resolved data on surface features, such as the topography of the surface atomic layer [65,91]. The principle behind the operation of an AFM is the detection of the deflection of a cantilever spring, which is equipped with a sharp tip. The tip has a radius of curvature of the order of nanometres, and is typically made of silicon, or silicon nitride, and is placed in proximity of the sample surface, where forces between the tip and the sample cause the deflection in the cantilever, as shown in Figure 2.5. The deflection of the cantilever is detected using a laser spot reflected off the top of the surface of the cantilever, into an array of photodiodes, generating an image of the topography of the sample. There is a direct connection between the displacement of the cantilever, and the forces acting upon it, known as Hooke's Law, where:

$$F = k\Delta z \qquad \text{Equation 2.1}$$

where:

k is the spring constant

Δz is the cantilever deflection

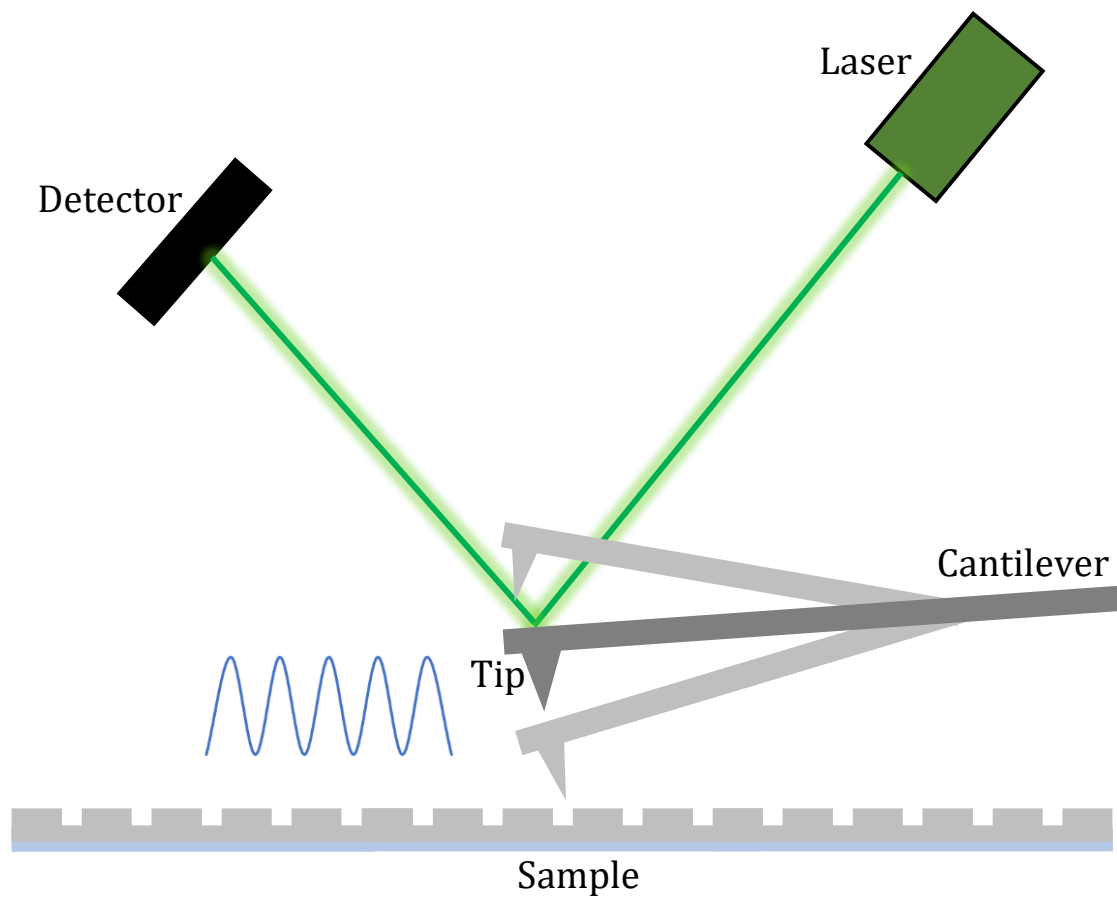


Figure 2.5. Schematic of Atomic Force Microscopy, in tapping mode. The tip oscillates over the sample surface causing a deflecting in the cantilever. The deflection is detected by a laser, focused on the back of the tip, and relayed to a photodiode array, where it is converted into an image of the topography of the sample surface.

In tapping mode the cantilever is driven at, or close to its resonance frequency. A feedback loop maintains the constant oscillation frequency by changing z-height using a piezo-scanner in the AFM stage. A set-point, close to the resonance, is selected, which will maintain a small force between the sample and the tip. Tapping mode offers advantages over other AFM imaging modes, i.e., contact, non-contact, as it prevents the sample and the tip from being destroyed, and prevents the tips from becoming trapped by adhesive forces of a contaminant layer [92,93].

While structural characterisation is important, optical characterisation of plasmonic metasurfaces is highly important and is used to understand how the properties of the metasurface can influence the absorption and emission of light in optoelectronic devices.

2.4. UV/Visible Spectroscopy

UV/Visible spectroscopy (PE Lambda 650 S) is a low-cost, fast, and simple technique used to characterise the absorption of a surface or solution [94]. By measuring the reflectance and transmittance of light through a sample, the absorption can be calculated.

Another useful technique for characterising the optical properties of plasmonic metasurfaces is angle resolved reflectance spectroscopy (Lab-built set up). Keeping the incident angle equal to the detection angle, reflectance spectra can yield interesting information, such as a Localised Surface Plasmon Resonance (LSPR), shown in Figure 2.6

2.5. Localised Surface Plasmon Resonance

LSPRs are electron oscillations at the interface of a metallic surface that occur when metallic nanoparticles are excited with incident light. LSPRs are the non-propagating oscillation of an electron cloud within a metallic NP that occur when the size of the NP is smaller than the wavelength of the incident light. The oscillations of the electron cloud within the NP are driven by the incident light causing the displacement of the electrons from their ground state. The Coulomb force acts as a restoring force between the electron cloud and the nuclei of the atom [95,96].

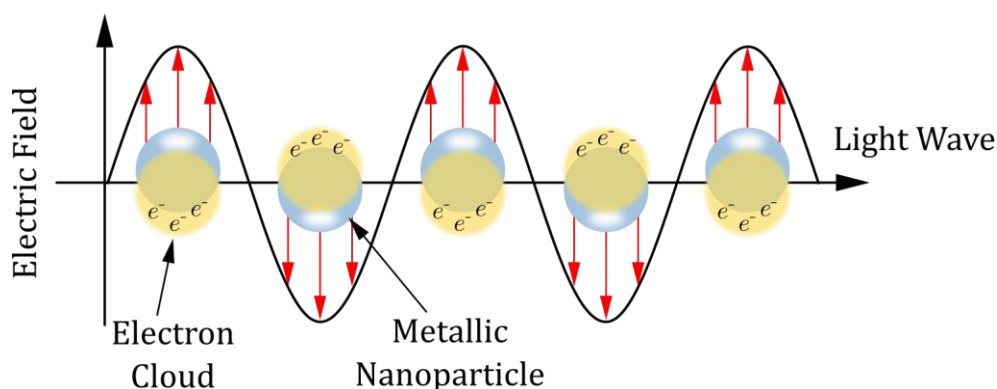


Figure 2.6. Schematic of localised plasmon resonance in a metallic nanoparticle.

2.6. Nanobiomaterials

Nanobiomaterials (NBMs) are used in biomedical research in both *in vivo* and *in vitro* models for drug delivery studies, disease detection and treatment, as well as in tissue engineering [97–101]. The European Commission defines a nanomaterial as NPs where 50% or more are between 1 – 100 nm [102]. While the characterisation techniques previously mentioned are useful for characterising metallic nanoparticles, not all of

them are useful for characterisation of NBMs. SEM, ESEM and AFM can provide useful information about the physical dimensions of NBMs, however, they do not generate data on the properties of the NBMs when they are in solution [103]. The current state-of-the-art for characterising NBMs in solution is NP tracking analysis (NTA), and dynamic light scattering (DLS) [104]. The hydrodynamic diameter of the NBM is a commonly determined particle parameter, arrived at by calculating the Stokes-Einstein equation:

$$D_t = \frac{Tk_B}{3\pi\eta d} \quad \text{Equation 2.2}$$

where:

T is the sample temperature (K),

η is the solvent viscosity (kg/m s),

k_B is Boltzmann's constant ($1.38 \times 10^{-23} \text{ m}^2\text{kg s}^{-2}\text{K}^{-1}$),

d is the hydrodynamic diameter (m),

D_t is the diffusion coefficient (m^2/s).

Chapter 1 discussed the current state-of-the-art used in the pre-clinical assessment of NBMs, and its limitations, necessitating the need for a more robust method of assessing NBM toxicity. Three-dimensional *in vitro* models, or spheroids, have the potential to replace the current state-of-the-art. As NBMs are used as drug delivery systems, monitoring the biodistribution and translocation within a 3D model is important. In the case of NBMs within a spheroid, trafficking and biodistribution refer to the homogeneous (or not) distribution of the NBM through the focal plane of the spheroid; translocation refers to the location of the NBM in the focal plane, whether observed at the core or the periphery of the spheroid. SEM, ESEM, and TEM are useful microscopies for looking into the core of the spheroid, however, they are destructive techniques, with complicated sample preparation techniques. Flow cytometry is an alternative technique that uses fluorescence to characterise the uptake and penetration of NBMs in spheroids [105,106]. While flow cytometry is a useful technique that can rapidly quantify the uptake of NBMs in cells, and differentiate between cells and NBMs, the information acquired is limited to histograms and dot plots. This data is obtained by

distinguishing the forward and side scatter properties of populations of cells. These properties give an estimation of the size (forward scatter) and granularity (side scatter) of the cells [107].

2.7. Spheroids

Spheroids are comprised of a 3D structure of layers of cells, that mimic the function of cells, and the biological and physical structure of cells in the *in vivo* environment. In an *in vivo* environment, cells receive stimuli that has been noted in the 3D configuration [108,109]. During a cells life cycle the cell goes through many phases:

1. Proliferating: the cells divide and there is a growth in the number of cells.
2. Quiescence: cells are no longer dividing, but remain metabolically active, with the ability to restart proliferating.
3. Apoptosis (programmed cell death): damaged cells die.
4. Hypoxia: the cells do not receive enough oxygen and
5. Necrosis: uncontrolled cell death.

A 2D cell culture is comprised mostly of proliferating cells. During cell culture, the culture media requires replenishment, and during this media change necrotic cells are washed away. In a 3D culture, however, the necrotic cells are not washed away during culture media changes. As the 3D culture is made up of layers of cells, these cells will be in different stages of their life cycle [110]. Closer to the core of the spheroid, cells will lack nutrients and oxygen, and will become hypoxic and quiescent, whereas cells closer to the edge of the spheroid will have easy access to the nutrients provided by the culture media and therefore remain viable and proliferating [109,111]. This configuration of proliferating, hypoxic and quiescent cells mimics *in vivo* tissues, and tumours, making spheroids a good alternative to *in vivo* studies.

As previously mentioned, NBMs can be used as drug delivery systems. They can also be used for deep tissue imaging by loading them with fluorescent molecules. In this work, two NBMs were chosen: A dye-loaded liposome, emitting in the near infrared region of the electromagnetic spectrum, at 780 nm, and a polymeric shell loaded with a fluorescent dye that emits in the red region, 625 nm – 740 nm, of the visible spectrum, indicated on Figure 2.7.

2.8. Fluorescence

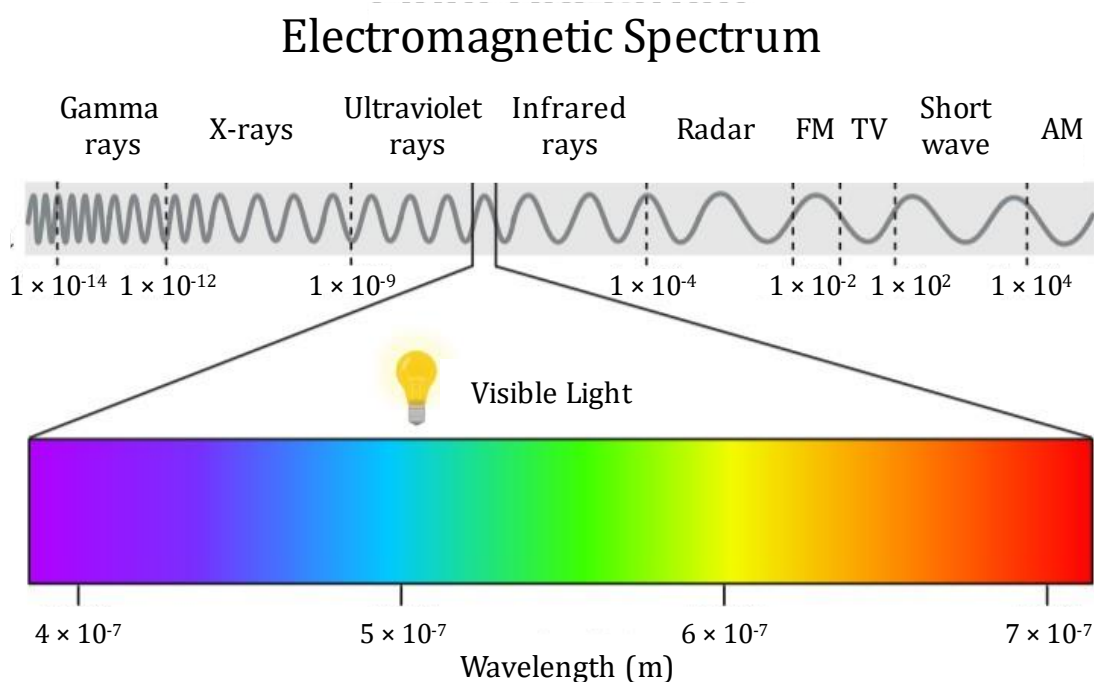


Figure 2.7. The electromagnetic (EM) spectrum showing the range of EM radiation, highlighting the visible spectrum.

The fluorescent molecules used were IR780, and Nile Red 668. Fluorescence can be explained using the Jablonski diagram shown in Figure 2.8. Absorption of light by a fluorophore, a fluorescent molecule, causes the electrons to become excited, and move from their ground state to a higher energy state. The high energy electrons will drop to a lower energy level through vibration relaxation, and from there they will decay back to the ground state. As this happens, the electrons will release energy in the form of a photon. This is known as fluorescence.

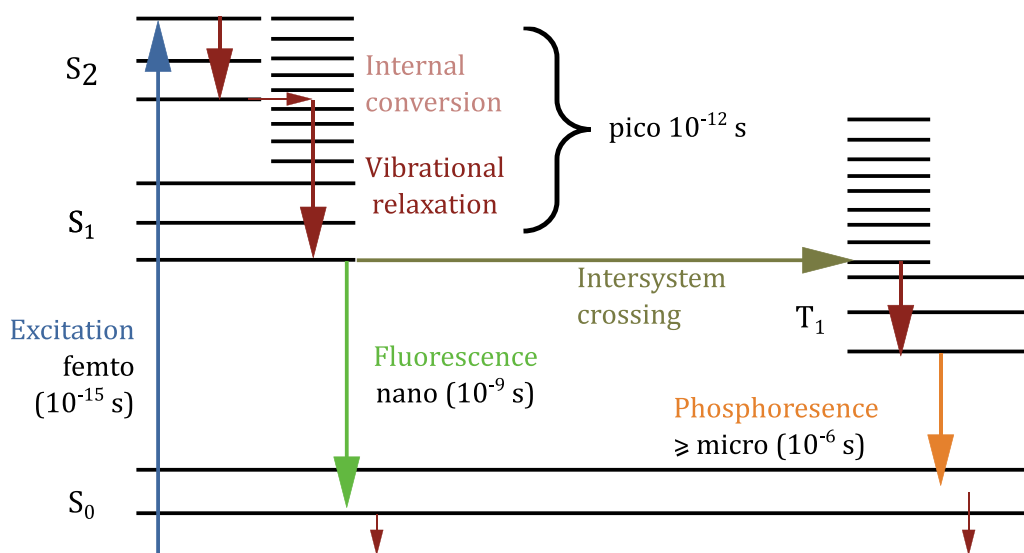


Figure 2.8. The Jablonski diagram. This diagram describes what happens to an electron when it absorbs light. The electron will move from its ground state to a higher energy state. Through vibrational relaxation, the electrons will decay to a lower energy state, from which they will return to their ground state. At this point they will release energy in the form of a photon. This is known as fluorescence. Intersystem crossing can also occur, which will lead to phosphorescence [112].

The wavelengths at which fluorophores absorb and emit light can be seen in UV/Visible spectra, shown in Figure 2.9. The difference in the peak absorption wavelength and the peak emission wavelength is known as Stokes Shift, named after Irish physicist George Gabriel Stokes, which can be expressed as follows:

$$\Delta\lambda = \lambda_{ems}^{max} - \lambda_{abs}^{max} \quad \text{Equation 2.3}$$

where

$\Delta\lambda$ is the Stokes shift (nm)

λ_{ems}^{max} is the peak emission wavelength (nm) and

λ_{abs}^{max} is the peak absorption wavelength (nm).

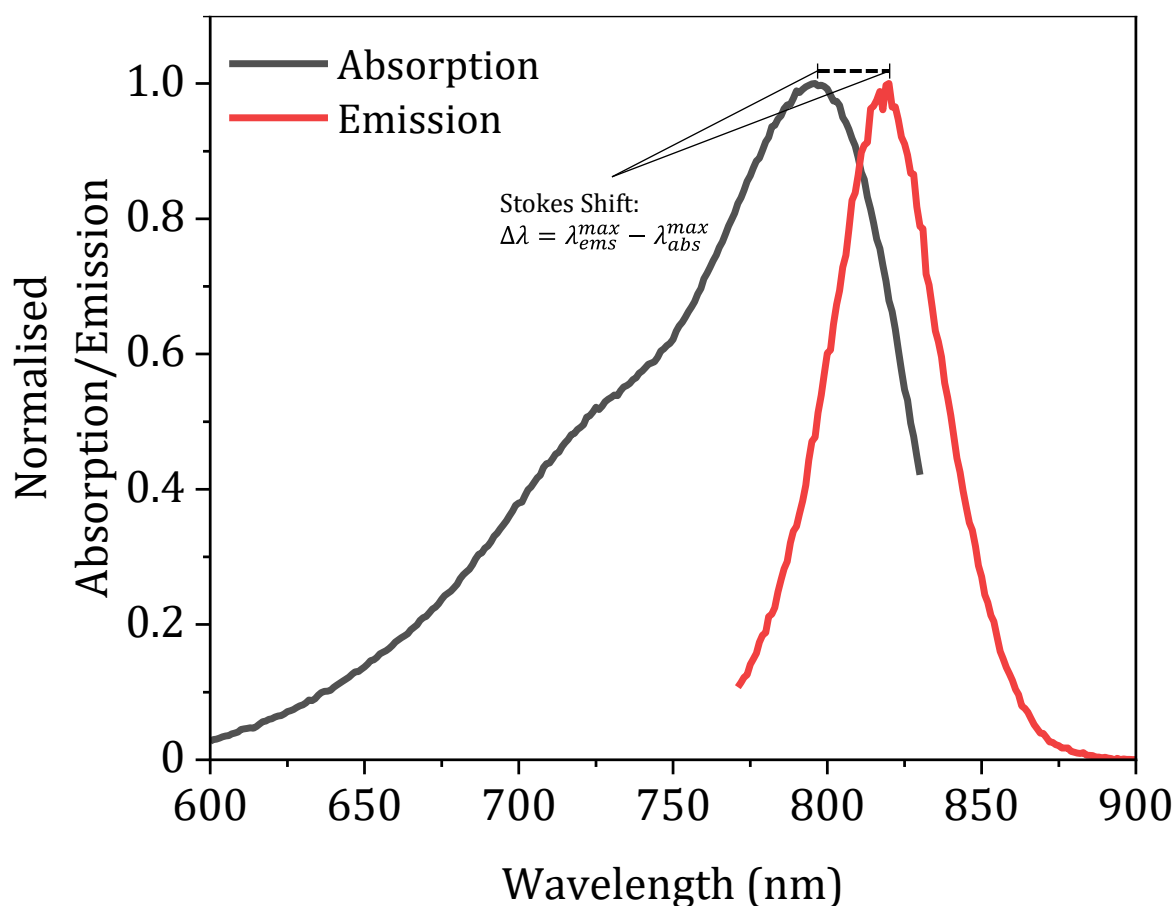


Figure 2.9. Normalised absorption/emission spectra of the NMB LipImage taken using UV/Visible spectroscopy using PE Lambda 650S UV/Visible spectrometer. Stokes shift is the wavelength difference between the max emission wavelength, and the max absorption wavelength.

In this work, the fluorescence techniques used are confocal microscopy, and fluorescence lifetime imaging microscopy.

Confocal microscopy is a powerful fluorescence microscopy technique. Unlike epifluorescent microscopy, where the entire sample is evenly flooded with light, confocal microscopy only exposes small areas at a time by scanning across the sample. Confocal microscopy uses a spatial pinhole to block out of focus light, which also allows for **z**-stack imaging, which can then be used to create a three-dimensional (3D) rendering of the sample being imaged [113]. Selecting the correct pinhole depends on two things: (1) the excitation wavelength (λ), and (2) the numerical aperture (N.A.) of the objective lens. This allows the Airy disc size to be calculated, shown by Equation 2.4.

$$\text{Airy Disc } (\mu\text{m}) = \frac{0.8\lambda}{2 \times \text{N.A.}}$$

Equation 2.4

The viability of spheroids, i.e., assessing the distribution of live and dead cells has been done using confocal microscopy [114], as well as using 3D stacks to measure distribution through a spheroid [115]. Using spheroids grown from liver cells, confocal microscopy has been used to evaluate drug-induced liver injury [116].

Figure 2.10 shows a schematic illustration of the MicroTime200 from PicoQuant, a powerful and versatile time-resolved confocal microscope. The MicroTime200 is the fluorescence microscope that was used in this work.

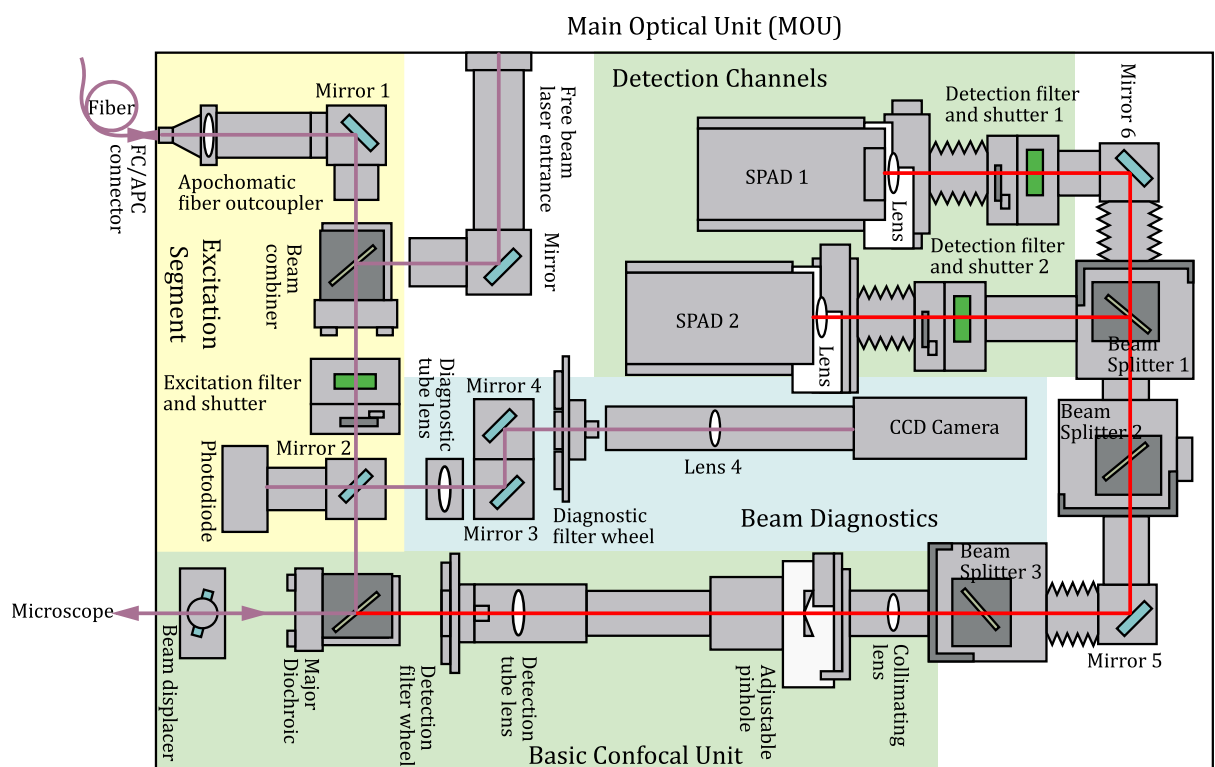


Figure 2.10. Schematic of MicroTime200. This schematic, based on the MicroTime200 manual, shows the optics and the light path for the main optical unit of the microscope, i.e., the excitation segment, the confocal unit, the detection channels. Pulsed laser light enters the MOU at the fibre, where it is directed to a beam splitter. This beam splitter directs the light into the microscope where the sample is excited. Fluorescence light emitted from the sample follows the light path back to the beam splitter, through the tube lens to the pinhole. The beam is then directed towards the emission filter, before being detected by the single photo-avalanche detector.

The MicroTime200 can also perform Fluorescence Lifetime Imaging Microscopy (FLIM). In this work, FLIM has been coupled with confocal microscopy, but it can also be coupled with two-photon excitation microscopy, and multiphoton tomography.

FLIM is an imaging technique that measures the fluorescence decay rate from a fluorophore. As previously mentioned, when a fluorescent molecule is excited it moves from its ground state to a higher energy level. The length of time it remains at the higher energy before returning to the ground state is known as its fluorescence lifetime. FLIM uses Time-Correlated Single Photon Counting (TCSPC). The schematic in figure 2.11 demonstrates the mechanism of TCSPC. The laser pulse starts a start-stop-timer, and when a fluorescence photon is detected by the Single Photon Avalanche Diodes (SPADS) the timer stops. This is repeated over and over, to account for the statistical nature of fluorophore emission. The times are then sorted into a histogram that plots the number of counts versus time.

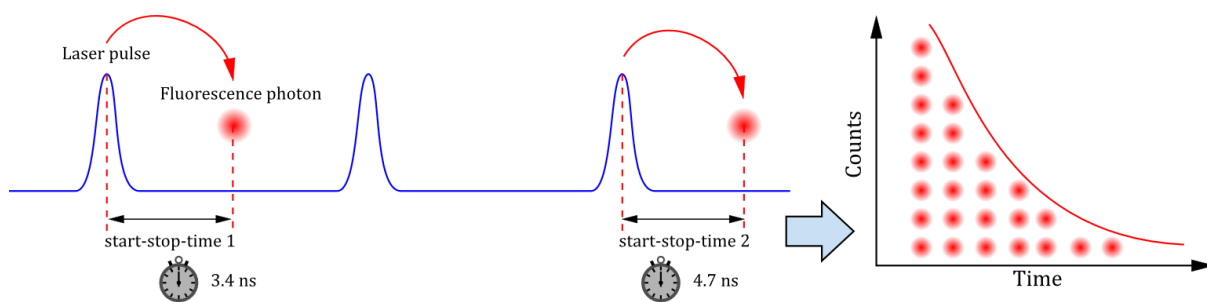


Figure 2.11. A schematic of time-correlated single photon counting (TCSPC). During confocal microscopy, TCSPC takes place. After the first laser pulse a timer is started and once a fluorescent photon is detected the timer is stopped. This is carried out repeatedly. The fluorescent photons detected are plotted in a graph, from which the average lifetime of the NBM can be calculated.

FLIM has been successfully used to monitor the release of doxorubicin from particles following their uptake into cells [117], the uptake of diagnostic and therapeutic nanoparticles in spheroids [118], and the distribution of metallic nanoparticles in spheroids [119].

This chapter has introduced a range of fabrication and characterisation techniques that are used for the research report in this thesis. The structural and optical properties of different types of NPs determine their functionality and suitability for applications in optoelectronic and nanomedicine applications.

Chapter 3 Structural, optical, and electrical properties of silver grating prepared by nanoimprint lithography of nanoparticle ink

This chapter examines the use of nanoparticles, in the form of a metallic ink, to fabricate metasurfaces that have the potential for incorporation into optoelectronic devices such as solar cells. § 3.1 describes the process of fabrication, how the parameters of nanoimprint lithography (NIL) were determined, and were compared to a conventional method for fabricating metasurfaces. The structural, optical and electrical properties of the NIL fabricated surfaces are examined in detail, and compared to the conventional method, using multiple microscopy modalities. Finally, the structural characterisations are compared to planar surfaces, fabricated using the same techniques.

3.1. Materials and Methods

3.1.1. Materials for fabrication of gratings and planar silver nanostructures

The following materials were purchased from Sigma-Aldrich:

- Silver ink with nanoparticle size < 10 nm in diameter, in a solution of 50 – 60 wt. % tetradecane
- Poly (methylmethacrylate) (PMMA), with a molecular weight (M_w) $\sim 120,000$ g/mol by Gel Permeation Chromatography (GPC)
- Methanol (HPLC grade)
- Corning cover glass, no. 1 thickness, 22×22 mm
- Deionised (DI) water
- Isopropanol (IPA) (HPLC grade)
- Polydimethylsiloxane (PDMS; Sylgard®184)

Hydrochloric acid was purchased from Merck, and compact discs (CD) (Verbatim CD-R) purchased from Radionics.

3.1.2. Methods

To create the grating, a blank CD, a cross-section of which is depicted in Figure 3.1, was cleaned by removing the foil using Sellotape, and then submerging the CD in a methanol:HCl 10:1 mixture for 10 minutes. This allowed time for the acrylic layer to dissolve. The CD was then rinsed in DI water three times to ensure all traces of the acrylic layer, and the methanol:HCl solution were removed, before finally rinsing in IPA. To ensure all of the foil and acrylic layer was removed, the CD surface was inspected using bright-field microscopy (BFM). Figure 3.2 shows a CD with some of the CD label, or foil layer still present. The pits and lands are also visible in this image. Once cleaned, the CD was placed, grating side up, in a glass dish. PDMS was mixed by hand, continuously for ten minutes, to ensure effective cross-linking, and subsequently, the viscous PDMS was poured on the CD (Figure 3.3). The PDMS-coated CD was then placed in a pre-heated ambient condition oven at 130 °C for 30 minutes to cure the mould. The Pyrex dish was removed from the oven, and allowed to cool to room temperature before a section of PDMS was cut using a scalpel and carefully peeled from the CD using a tweezers. At the same time, a planar, or flat, PDMS mould was also fabricated by pouring the viscous PDMS onto a microscope slide. The planar mould was cured under the same conditions.

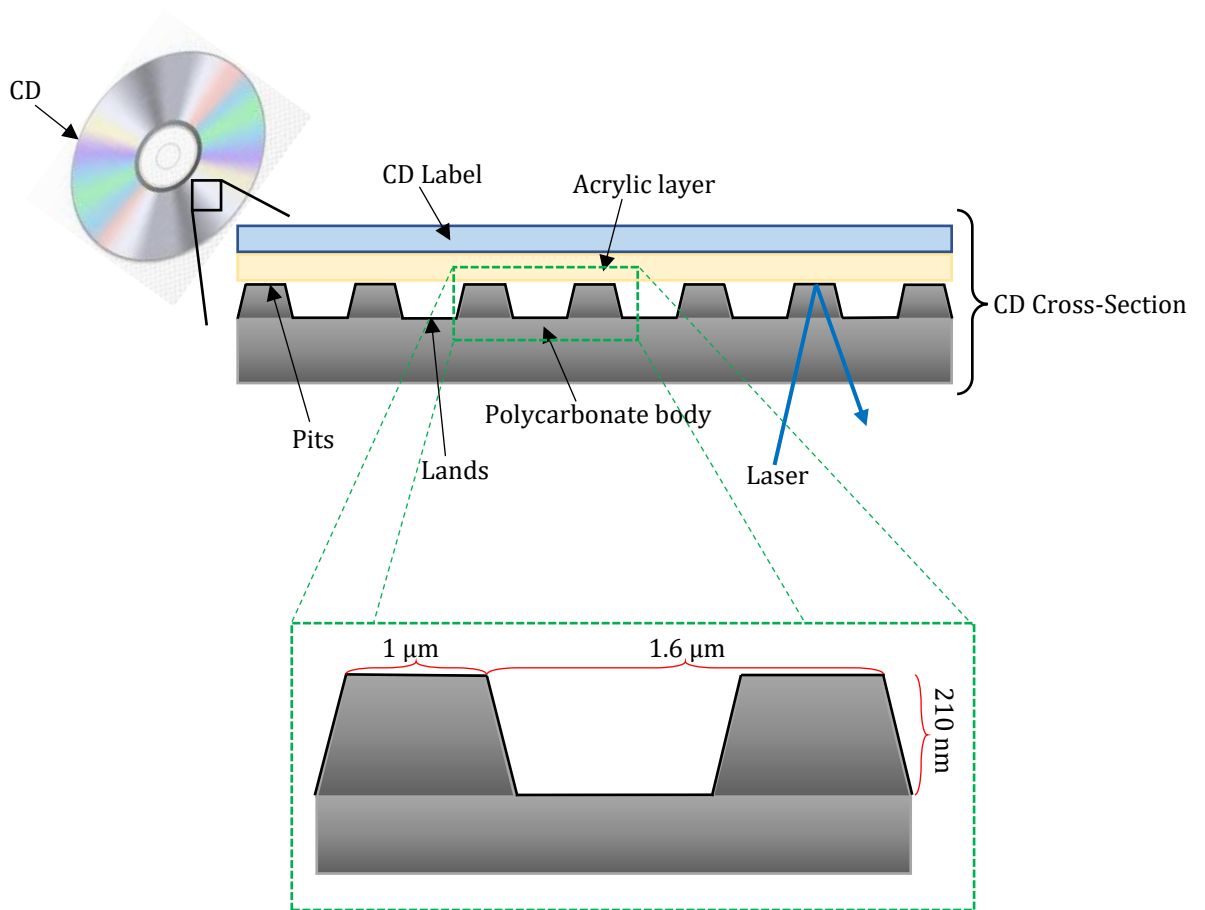


Figure 3.1. Schematic of a cross-section of a CD. To fabricate the grating pattern mould, the label was removed from the CD. The CD was then submerged in a methanol:HCl solution to remove the acrylic layer, revealing pits and lands a grating pattern. Not to scale.

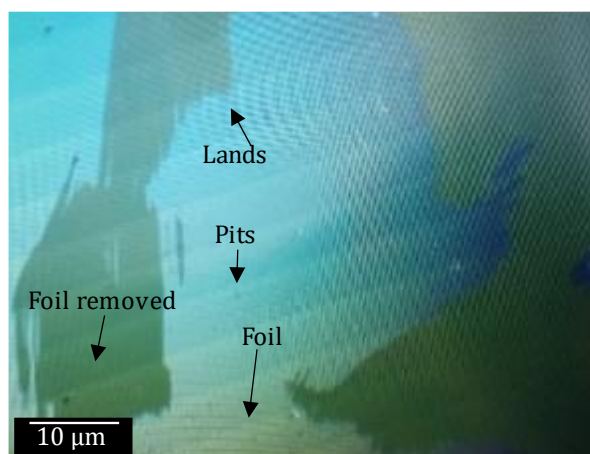


Figure 3.2. Bright-field microscopy image showing an area of the CD where the foil has not been fully removed by the cleaning process. The pits and lands of the CD are clearly visible in this image.

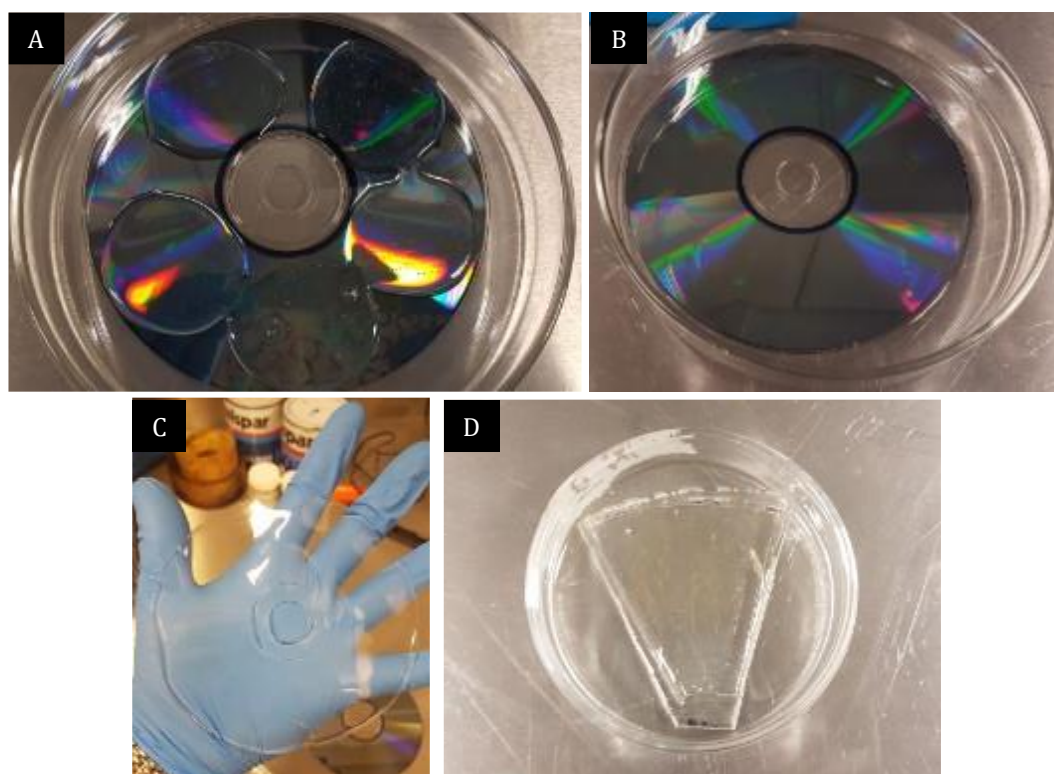


Figure 3.3. Fabrication of PDMS mould. CD placed into clean glass dish (A), and covered in PDMS (B). After curing and cooling, the mould was carefully peeled from the CD (C), and a section was cut and used as a master mould for NIL (D).

A PMMA solution, with a concentration of 5 wt. % in chloroform, was spin coated onto a cleaned glass cover slip, using the following dynamic spin coating parameters: 6000 RPM, 60 seconds, and 40 μL of PMMA solution. To make the PMMA solution, a small PTFE-coated stir bar was added to a small amber vial. 150 mg of PMMA powder was added to the vial with 3 mL of chloroform. The vial was sealed with a lid, and Para film,

and was placed into a water bath heated to 45 °C, and stirred at a rate of 1000 RPM for 20 minutes. After 20 minutes, the heat was turned off and the solution was allowed to cool to room temperature before being removed from the water bath. The solution was stored at room temperature until required [120].

Three grating, and three planar surfaces were fabricated using the following methods:

1. Imprinting the AgNPI on a glass substrate by the PDMS mould, and subsequent thermal annealing (AgNPI)
2. Imprinting the AgNPI on a PMMA-coated glass substrate (AgNPI/PMMA)
3. Imprinting a PMMA-coated glass substrate with the PDMS mould and subsequent thermal evaporation (TE) of Ag onto the imprinted, cured, PMMA (TE Ag/PMMA).

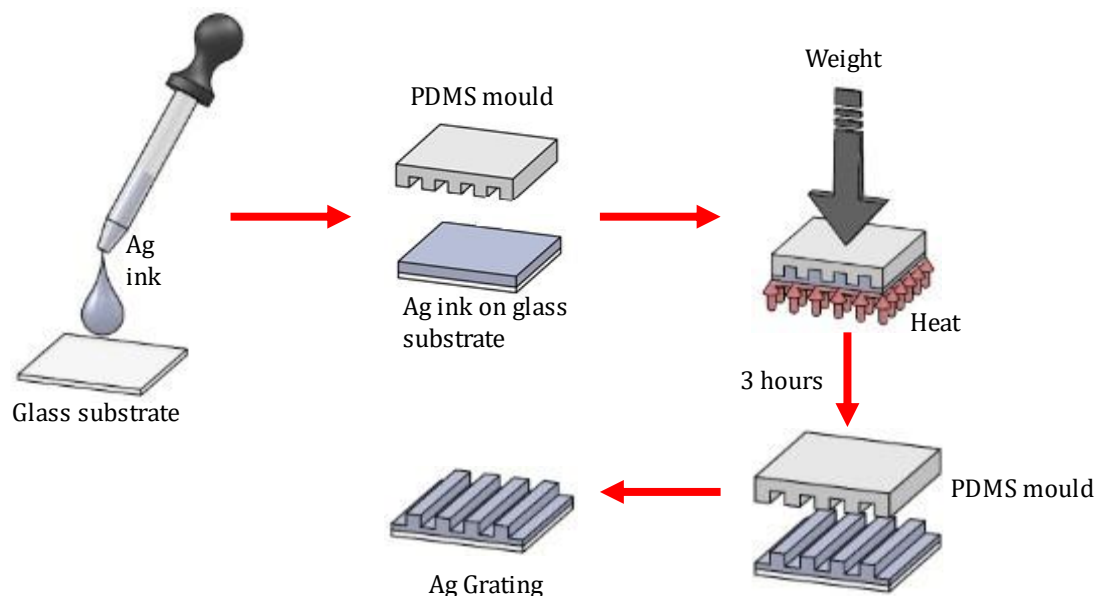


Figure 3.4. Schematic of NIL process for fabrication of AgNPI gratings, using method (1). AgNPI is placed on a glass substrate, with the PDMS mould placed on top of the ink. Weights are placed on top of the mould to ensure good transfer of the grating pattern. The sample was then annealed in an ambient condition oven for 3 h. The oven was then turned off and allowed to come to room temperature. The sample was then removed from the oven, and the PDMS mould carefully peeled from the AgNPI to reveal a silver nanoparticle grating.

To create surfaces using method 1, as shown in Figure 3.4, 60 mL of AgNPI was placed onto a cleaned glass coverslip. The PDMS mould (with grating or planar surface), cut from the original master template, was placed on top of the ink, imprint side down. This was then placed between aluminium plates. Extra Al plates, totalling a weight of 1.35

kg, are placed on top to facilitate mould pattern transfer. The sample was then subsequently annealed at 180 °C for 3 hours in a pre-heated ambient condition oven.

The annealing conditions were chosen after extensive testing of various temperatures and time, and are described in Table 3.1, with images shown in Figure 3.5. Figure 3.5 shows how the grating pattern was transferred under different conditions, whether not long enough, temperature too low, or not enough weight for pattern transfer. The parameters chosen allowed enough time for solvents to evaporate, and for the ink to anneal, with minimal cracking to the metallic film.

Table 3.1. Parameters explored for ideal annealing conditions of AgNPI.

Temperature (°C)	Time (h)	Weight (kg)	Outcome
RT	120	0.05	Solvent visible. Ink not annealed. Can be wiped off the glass substrate.
150	24	0.05	Sample not fully annealed. Grating pattern not fully transferred. Mould lifting off the ink during annealing. Removed from oven too soon, cracking visible
150	3 (plus cooling)	1.0	Better transfer of grating pattern. Not fully annealed. Cracking visible at edges
180	5 (plus cooling)	1.35	Good pattern transfer. Some ink adhering to mould during removal.
180	3 (plus cooling)	1.35	Good pattern transfer. No ink adhering to mould. Minimal cracking noted at edges where ink layer is thin.

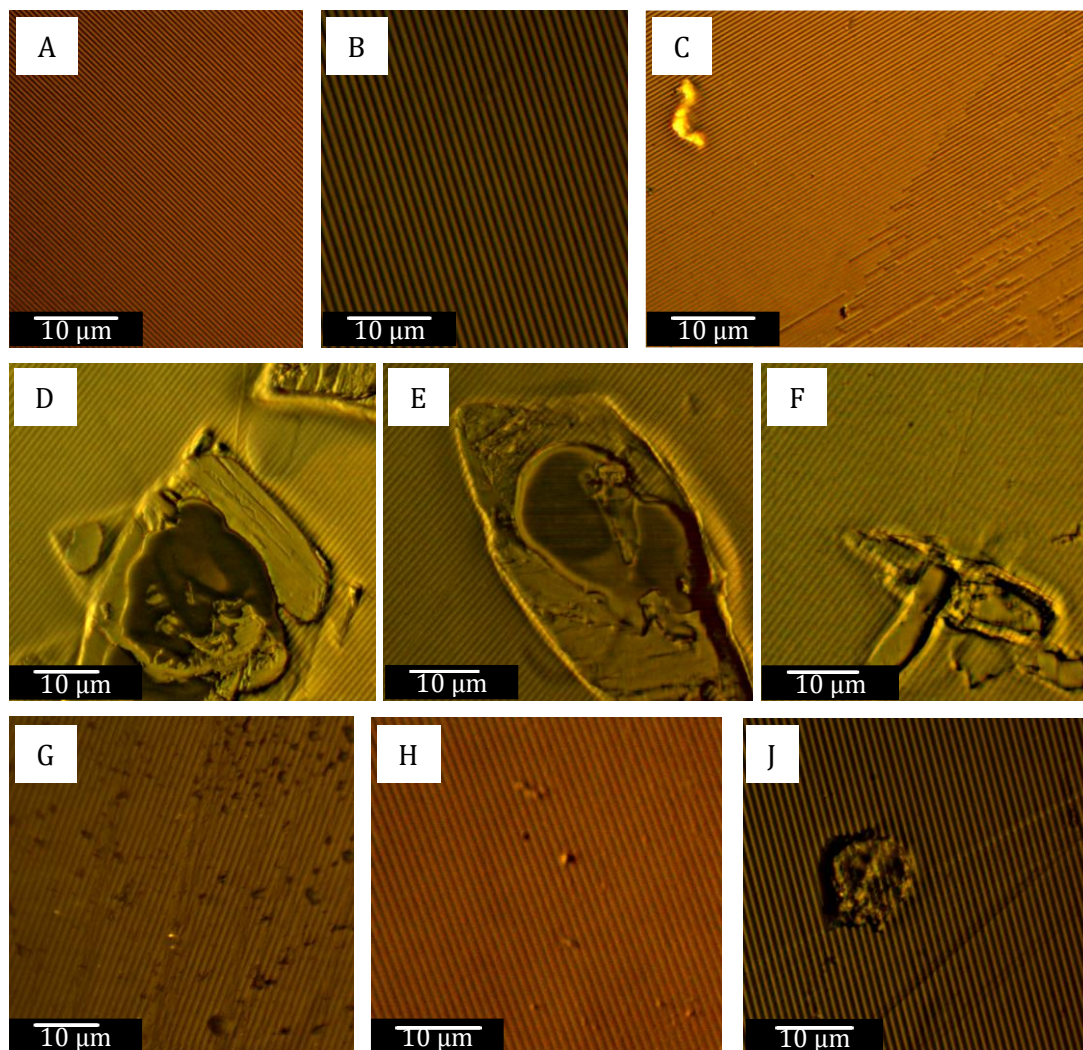


Figure 3.5. Bright-field images of grating patterns during testing phase. (A) and (B) show good pattern transfer. (C) was a result of not enough weight being placed on top of the mould. (D), (E), and (F) occurred when some of the ink adhered to the mould. (G), (H), and (J) have some artefacts on the grating, possibly from bad cleaning prior to NIL.

The samples were annealed by being allowed to cool to room temperature in the oven before being removed. This mitigated thermal shock cracking of the metallic ink, which can be seen in Figure 3.6. The PDMS mould was peeled off the Ag layer, revealing an Ag grating, shown in Figure 3.7. The procedure for the AgNPI planar thin film is shown in Figure 3.8.

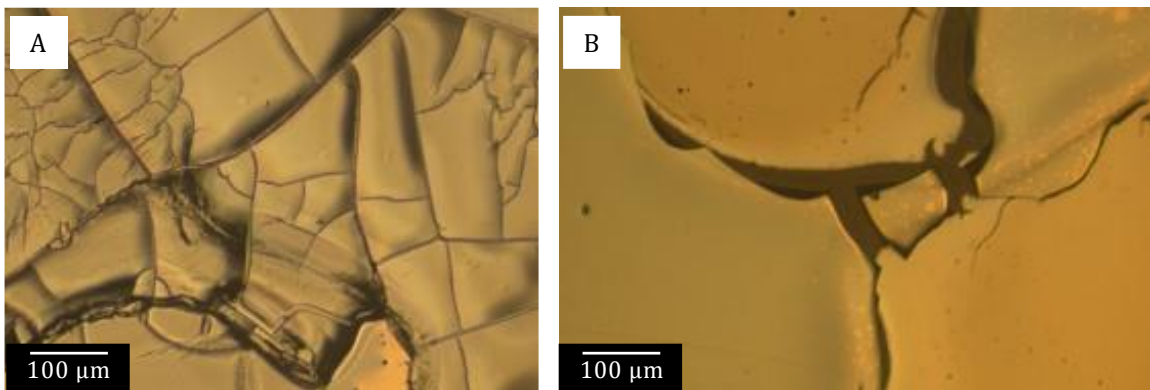


Figure 3.6. Thermal shock of AgNPI thin film. Taking the samples out of the oven before they have cooled causes thermal shock, which appears as cracking on the sample. These images show thermal shock which has occurred on planar AgNPI samples.

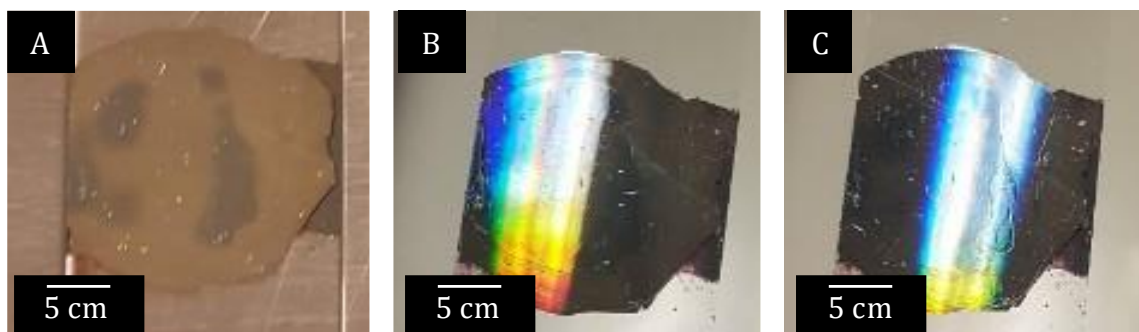


Figure 3.7. Silver ink grating on a glass substrate (A). The grating pattern (B and C) can be seen without the use of a microscope. By angling the sample to an overhead light, the diffraction pattern of the grating can be seen, indicating that the grating pattern has been transferred successfully.

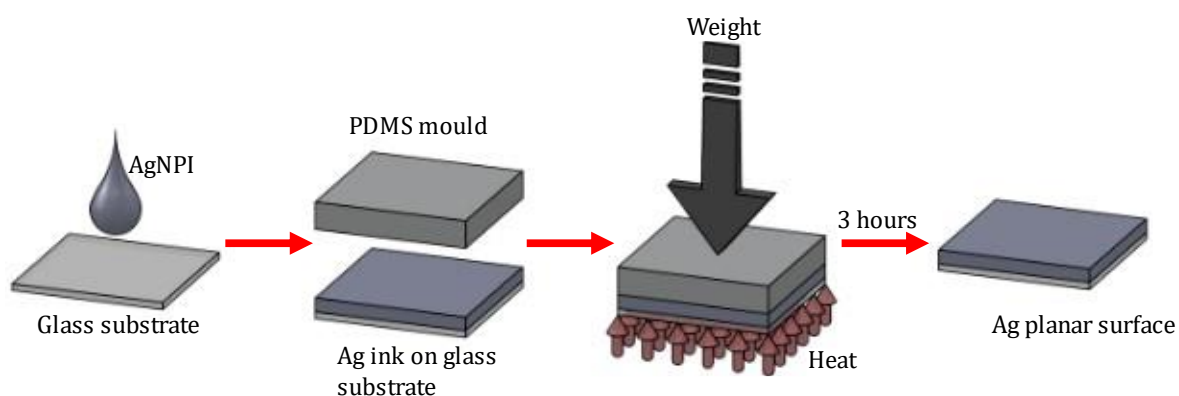


Figure 3.8. Schematic of the NIL process for fabrication of an AgNPI planar surface using method (1). AgNPI is placed on a glass substrate, with the PDMS mould placed on top of the ink. Weights are placed on top of the mould to ensure good transfer of the grating pattern. The sample was then annealed in an ambient condition oven for 3 h. The oven was then turned off and allowed to come to room temperature. The sample was then removed from the oven, and the PDMS mould carefully peeled from the AgNPI to reveal a silver nanoparticle planar surface.

To create samples using method (2), a 1.3 μm thick layer of PMMA was spin coated onto a clean glass coverslip. A 60 μL drop of room temperature AgNPI was placed on the PMMA-coated coverslip, and the PDMS mould (grating/planar) was placed on top, as shown in Figures 3.9 and 3.10, respectively. The rest of the procedure is the same as method (1).

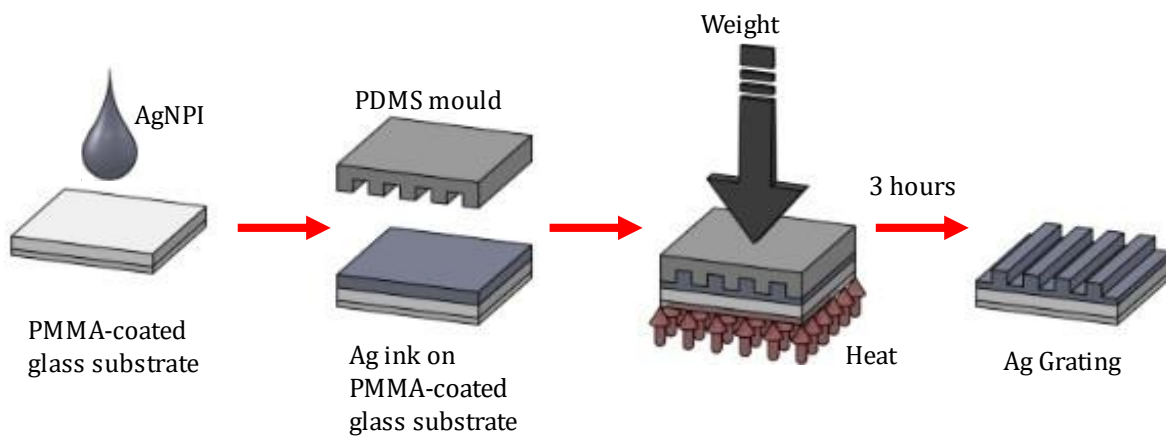


Figure 3.9. Schematic of the NIL process for fabrication of an AgNPI grating, using method (2). AgNPI is placed on a PMMA-coated glass substrate, with the PDMS mould placed on top of the ink. Weights are placed on top of the mould to ensure good transfer of the grating pattern. The sample was then annealed in an ambient condition oven for 3 h. The oven was then turned off and allowed to come to room temperature. The sample was then removed from the oven, and the PDMS mould carefully peeled from the AgNPI to reveal a silver nanoparticle grating.

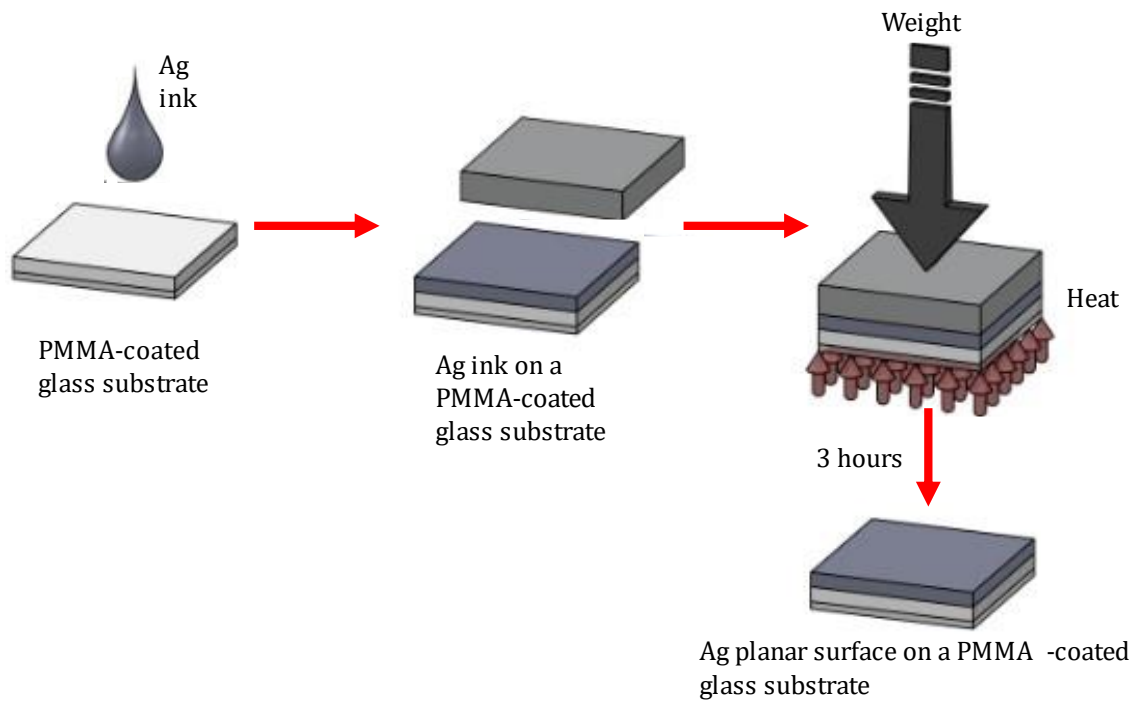


Figure 3.10. Schematic of the NIL process for fabrication of an AgNPI planar surface, using method (2). AgNPI is placed on a PMMA-coated glass substrate, with the PDMS mould placed on top of the ink. Weights are placed on top of the mould to ensure good transfer of the grating pattern. The sample was then annealed in an ambient condition oven for 3 h. The oven was then turned off and allowed to come to room temperature. The sample was then removed from the oven, and the PDMS mould carefully peeled from the AgNPI to reveal a silver nanoparticle planar surface.

Finally, fabricating samples, using method (3), PMMA was spin coated onto clean glass coverslips. PDMS moulds (grating/planar) was placed directly onto the PMMA. The subsequent steps are similar to method (1), except that the sample was placed in a pre-heated ambient condition oven at 170 °C for 2.5 hours [121]. These samples were allowed to cool to room temperature in the oven before being removed, and the PDMS mould was peeled off the PMMA film. A 100 nm thick Ag films was deposited by thermal evaporation under vacuum (3×10^{-6} Torr), at a rate of 1 \AA/s for roughly 20 minutes, as depicted in Figures 3.11, and 3.12.

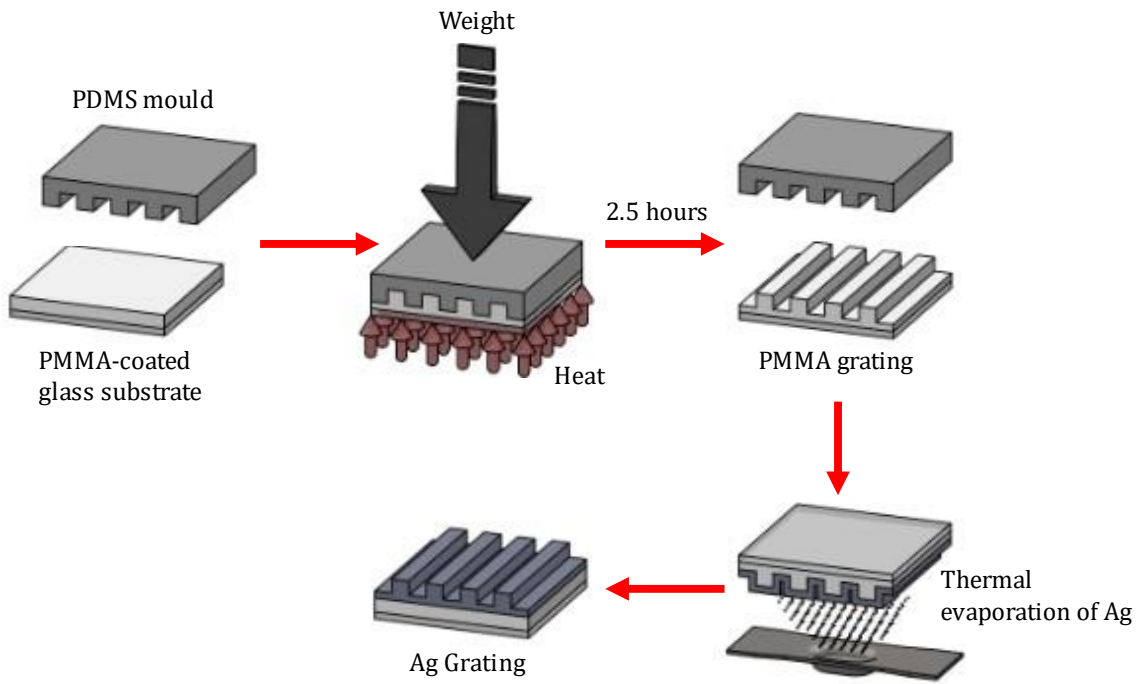


Figure 3.11. Schematic of the conventional NIL process for fabrication of an Ag grating using method (3). A PMMA-coated glass substrate is embedded with a PDMS grating mould and cured an ambient condition oven at 170 °C for 2.5 h. The sample was allowed to cool to RT and then the mould was careful removed from the PMMA film. A 100 nm thick Ag film was deposited by thermal evaporation under vacuum, leaving an Ag grating.

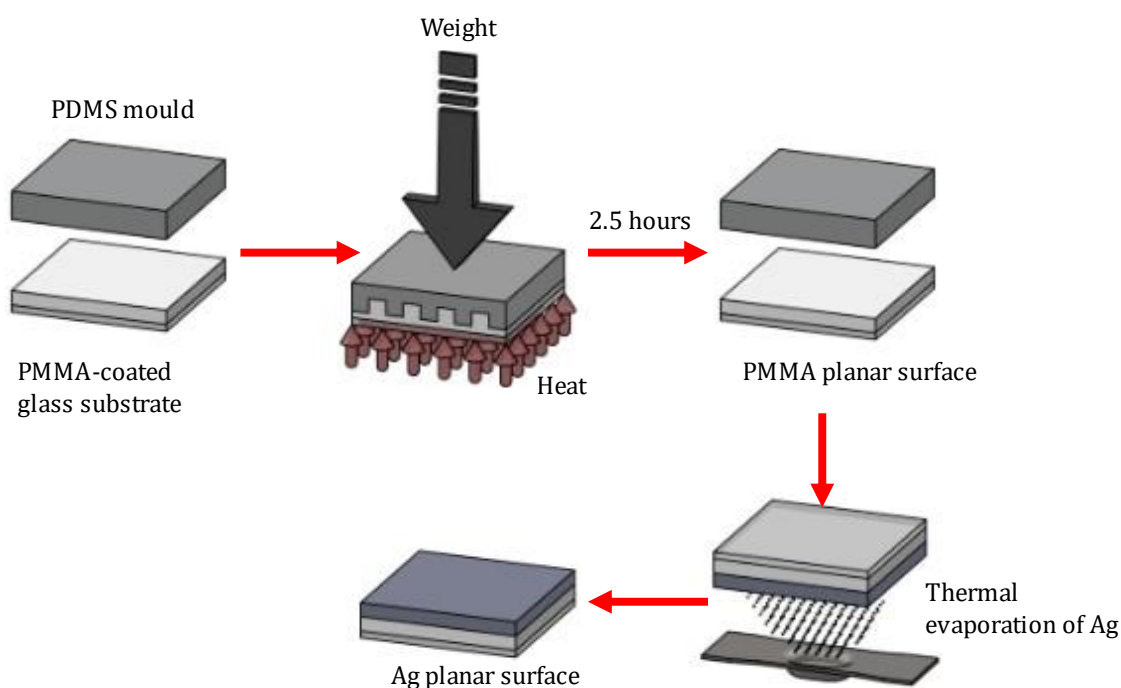


Figure 3.12. Schematic of the conventional NIL process for fabrication of an Ag planar surface using method (3). A PMMA-coated glass substrate is embedded with a PDMS planar mould and cured an ambient condition oven at 170 °C for 2.5 h. The sample was allowed to cool to RT and then the mould was careful removed from the PMMA film. A 100 nm thick Ag film was deposited by thermal evaporation under vacuum, leaving a Ag planar surface.

For the photoluminescence studies carried out, PVK:Flrpic was spin coated onto all the fabricated surfaces. PVK:Flrpic was prepared using the following protocol: 0.036 g of poly(9-vinylcarbazole) (PVK) and 1 mL of chlorobenzene were added to a small amber vial. A PTFE-coated stir bar was added to the vial. The vial was sealed with a lid and Para film, and placed in a water bath heated to 40 °C and stirred at 1000 RPM for 10 minutes. 0.004 g of bis[2-(4,6-difluorophenyl)pyridinato-C²N](picolinato)iridium(III) (Flrpic) and 1 mL of chlorobenzene were added to a small amber vial. A small PTFE-coated stir bar was also added to the vial. The vial was then sealed with a lid and Para film, and placed in a water bath heated to 40 °C, and stirred at 1000 RPM for ten minutes. These stock solutions were allowed to cool to room temperature in the water bath, and then wrapped in aluminium foil, without removing the Para film sealing the lid. The stock solutions were then stored at room temperature until used. To make a useable solution of PVK:Flrpic, equal amounts of the stock solutions were added to an amber vial, with a PTFE-coated stir bar. The vial was sealed with a lid and Para film. It was then placed in a water bath heated to 40 °C and stirred at 1000 RPM for 10 minutes.

The following dynamic spin coating protocol was used: 100 μ L PVK:FIrpic solution was dropped onto the substrate at 2000 RPM and spun for 25 seconds, producing a film thickness of 62 nm \pm 8.1 nm. The samples were then allowed to dry at room temperature, overnight, in the dark.

3.2. Characterisation

Characterisation of the fabricated samples was subdivided into three different categories: optical, structural, and electrical.

Throughout the fabrication process, the CD, moulds, and samples were inspected using bright-field optical microscopy (Leitz Optical Microscope) to assess the surfaces for artefacts or damage caused during the cleaning and fabrication process, and to ensure good quality pattern transfer.

Optical characterisation involved UV/Visible spectroscopy (PE Lambda 650 S), angle resolved spectroscopy (lab-built setup), and photoluminescence studies on a spectrofluorometer (Edinburgh Instruments FS5) and photoluminescence maps using dark field microscopy (Olympus BX53), shown in Figures 3.13 and 3.14. Structural characterisation involved using bright-field microscopy (BFM), scanning electron microscopy (SEM) (Zeiss Ultra *plus*), and atomic force microscopy (AFM) (AFM Asylum MFP-3D), shown in Figure 3.15. Electrical properties were measured using a four-point probe (Osilla) shown in Figure 3.16.

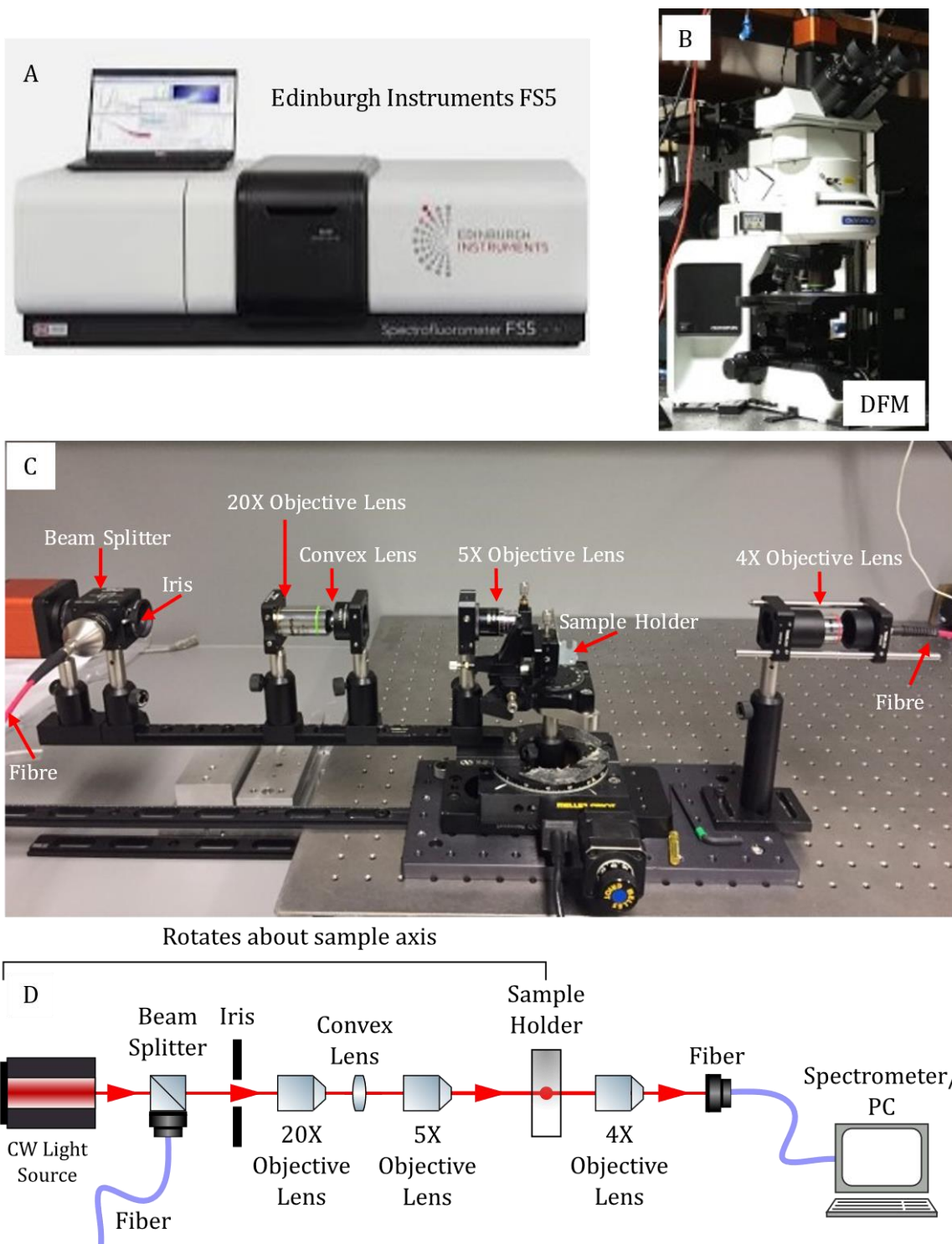


Figure 3.13. Optical characterisation of fabricated surfaces was carried out using (A) Spectrofluorometry, (B) Darkfield microscopy, (C) angle resolved spectroscopy, and (D) which shows the optical path for angle resolved spectroscopy.

UV/Visible characterisation was carried out on the Perkin Elmer Lambda 650S. The reflectance and transmittance of each surface, over a broad wavelength range, from 400 nm to 800 nm at normal incidence was determined. The integrating sphere detector collects both specular and diffuse reflection (R), and diffuse transmission (T).

From these spectra the absorption (A) of each surface can be calculated, using the following equation:

$$A = 1 - (R + T) \quad \text{Equation 3.1}$$

Angle-resolved reflectance spectra were collected by a lab-built setup shown in Figure 3.13. The angles were measured from 10° to 70° with a collimated incident light beam. For these measurements, the incident angle was kept equal to the detection angle.

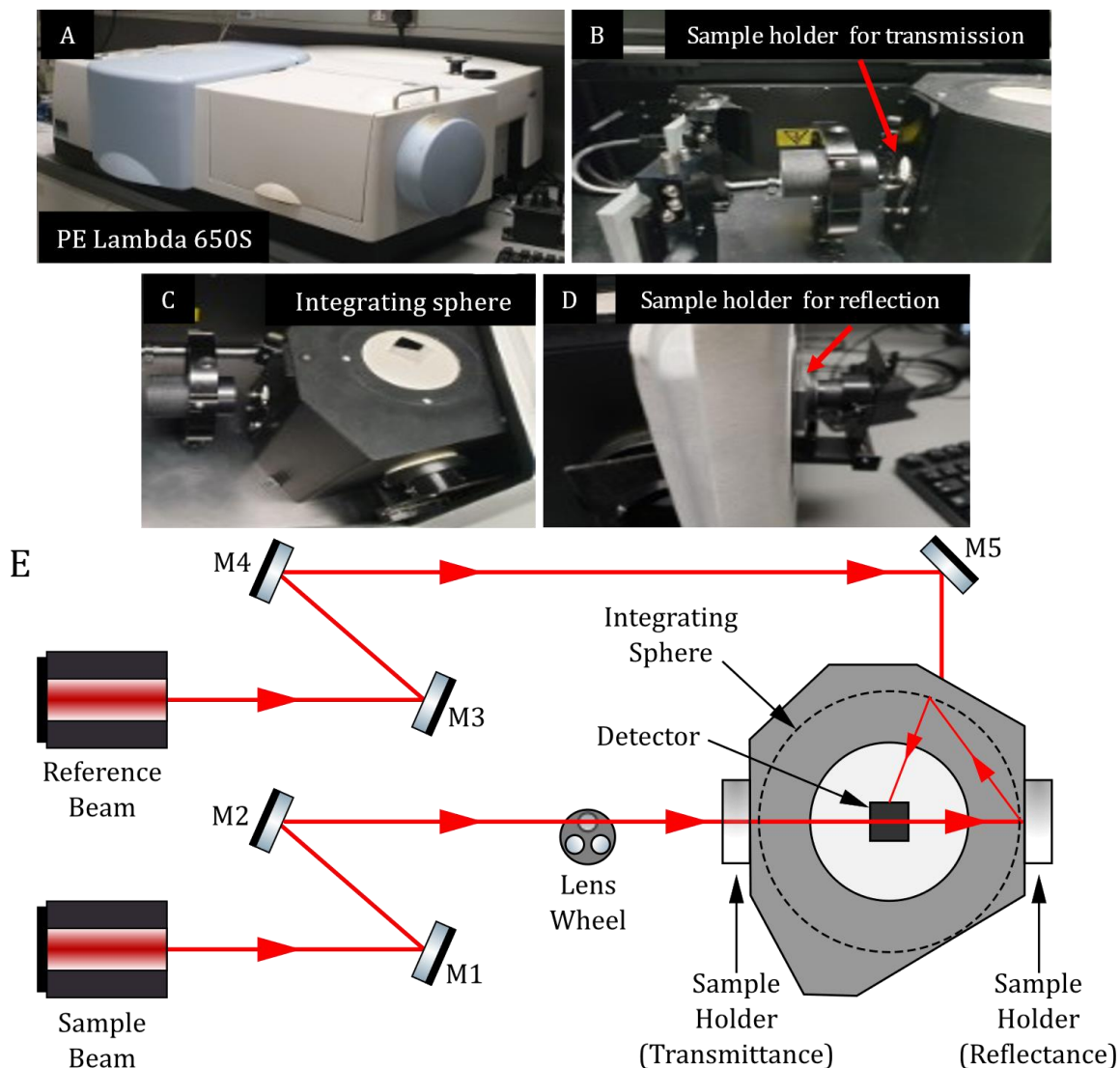


Figure 3.14. UV/Visible set up showing (A) the PE Lambda 650S, (B) placement of samples for transmittance spectroscopy, (C) the integrating sphere, (D) position of samples for reflectance spectroscopy, and (E) a schematic of the light path for UV/Visible spectroscopy.

Photoluminescence studies were carried out to determine if the nanoparticle and/or thermally evaporated Ag structures caused enhancement or quenching of a photo-emissive layer (PVK:Flrpic). Photoluminescence mapping was carried out using dark-

field microscopy, using an excitation wavelength of 405 nm, a 450 nm long pass filter, a 100X objective, and 0.5 second integration time. To obtain photoluminescence spectra (Edinburgh Instrument FS5), an excitation wavelength of 365 nm, a step size of 0.5 nm, and an integration time of 0.5 seconds were used. During emission map scan set up, emission correction background subtraction was selected. The resulting measurement is a true spectrum, undistorted by instrumental effects.

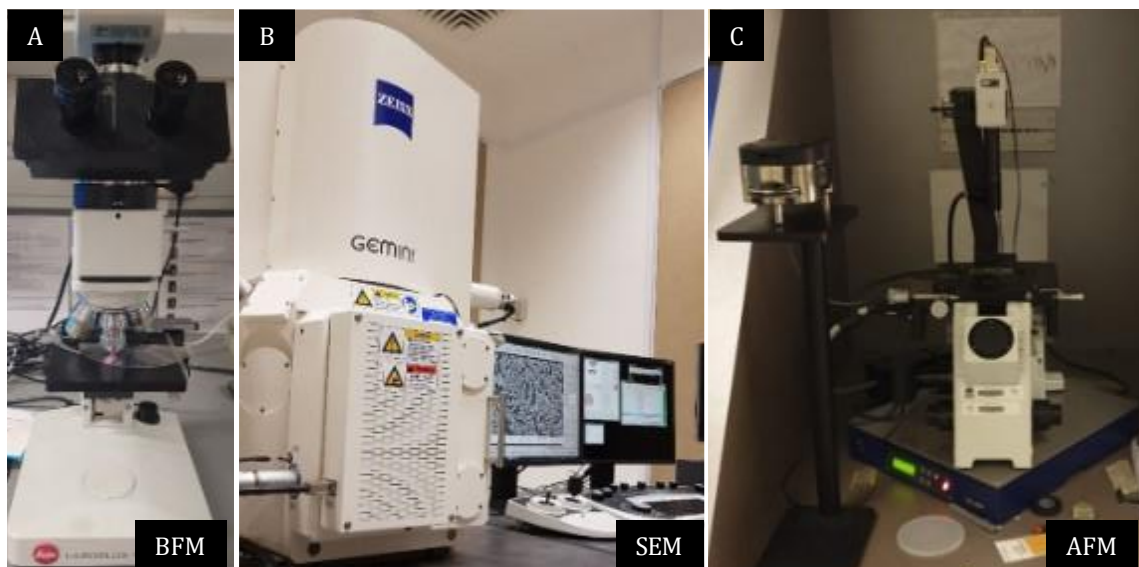


Figure 3.15. Structural characterisation of fabricated surfaces was carried out using (A) bright-field microscopy, (B) scanning electron microscopy, and (C) atomic force microscopy.

Structural characterisation was carried out using bright-field microscopy, scanning electron microscopy, and atomic force microscopy. To analyse the microstructure of the grating, SEM, and AFM were used. AFM was also used to determine the depth of the grating by importing AFM images into Gwyddion 2.53 image analysis software. This allows the plotting of line profiles of the grating, and was used to reconstruct 3D images of all surfaces, including the CD, and the PDMS mould.

Electrical characterisation was carried out by measuring the conductivity by using a four-point probe (Osilla), shown in Figure 3.16.

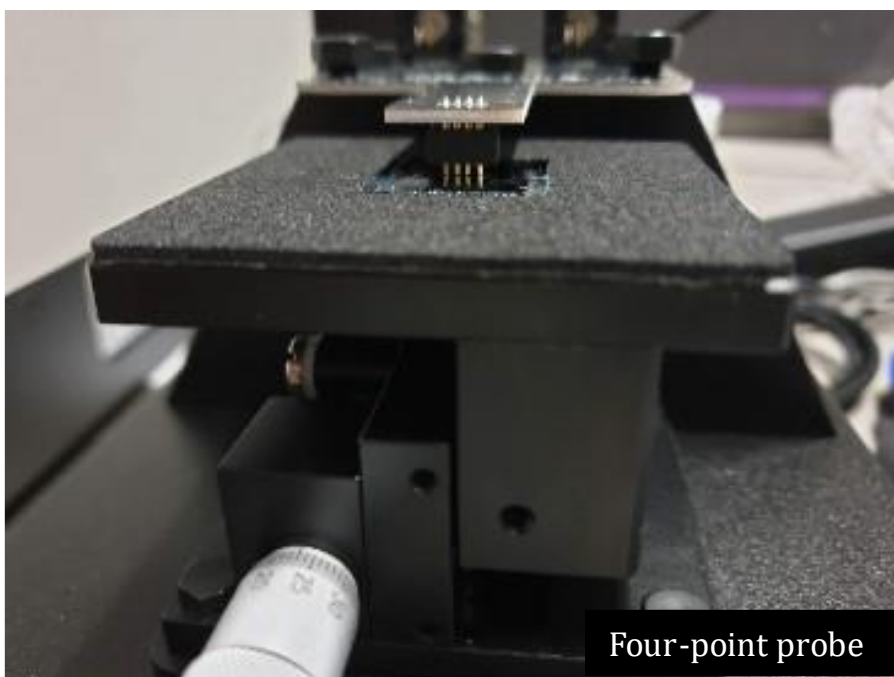


Figure 3.16. Electrical characterisation of fabricated surfaces was carried out using a four-point probe.

3.3. Results and Discussion

3.3.1. Structural Characterisation

The gratings were fabricated according to methods (1), (2), and (3), using a CD with a grating pattern with a nominal period of $1.6\ \mu\text{m}$, as described in § 3.2.

Bright-field microscopy was used to confirm good transfer of the grating pattern had been achieved for each of the three fabrication methods, and that no evidence of artefacts were present; sample images are seen in Figures 3.5 and 3.6.

These surfaces were further investigated using SEM, e.g., Figure 3.17, which revealed the nanoparticle ink samples have a rougher surface than those fabricated using thermal evaporation, as was expected. According to the manufacturer, the nanoparticles in the ink have a diameter of $\sim 10\ \text{nm}$; however, particle size analysis shows a range of nanoparticle diameters from $11\ \text{nm}$ to $> 200\ \text{nm}$. This suggests nanoparticle agglomeration occurs during the annealing process. This effect is even more evident for the samples prepared with a PMMA layer. It is possible that during the annealing step, the PMMA and AgNPI amalgamate, leading to a change in both the PMMA and AgNPI properties, as well as the nanoparticle size. Using a focused ion beam (FIB) to etch a cross-section into the samples, Figure 3.18, shows that the NPs

penetrate into the PMMA layers. Larger clusters of NPs are seen at the surface, with small NP clusters penetrating into the PMMA layer. Using FIB to etch a cross-section into the thermally evaporated sample was attempted. However, the Ag layer was only 1 Å thick and it delaminated. The larger particle sizes seen in AgNPI/PMMA results in a rougher surface for both the grating and the planar surfaces, when compared to TE/PMMA, which can be clearly seen in Figure 3.17 A – C.

The pitting observed in the planar surfaces seen in Figure 3.17 D – F may have arisen during the fabrication of the PDMS mould. The PDMS moulds were examined using bright-field microscopy after they were fabricated, but pitting/bubbles were not observed. It may be possible to eliminate these features using a vacuum oven during the fabrication of the PDMS mould, with periodic degassing to burst the bubbles [122,123].

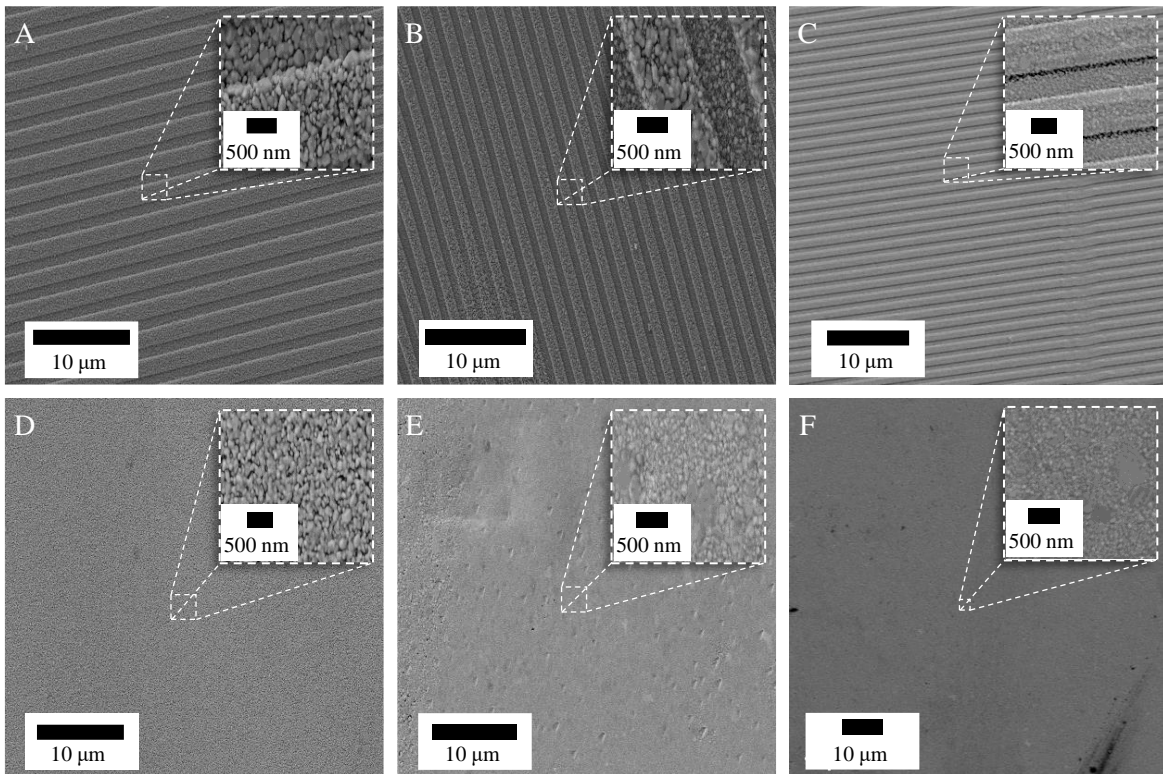


Figure 3.17. Scanning Electron Microscopy images of (A) AgNPI grating; (B) AgNPI/PMMA grating; (C) TE Ag/PMMA grating; (D) AgNPI planar surface; (E) AgNPI/PMMA planar surface; and (F) TE Ag/PMMA planar surface. All surfaces were fabricated on a glass substrate.

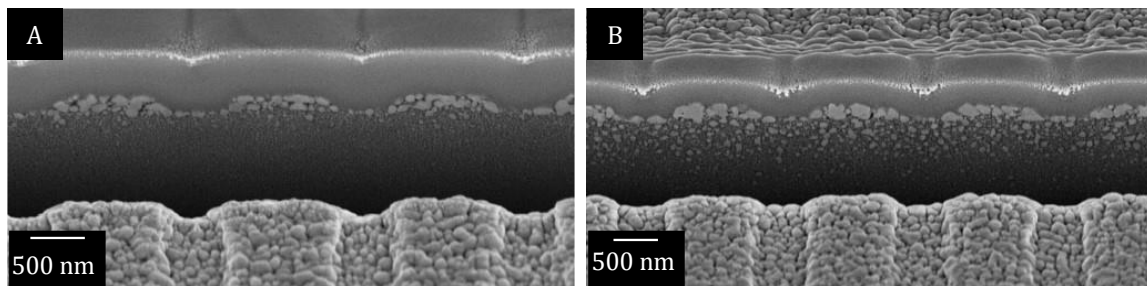


Figure 3.18. Focused Ion Beam (FIB) was used to etch a cross-section of (A) AgNPI grating and (B) AgNPI/PMMA grating, showing how using PMMA creates larger clusters of NP at the surface of the grating, and also shows how the AgNPI permeates the PMMA throughout the structures.

Topographic AFM was carried out on the CD, PDMS mould, and all fabricated samples. The data acquired allowed 3D representations, Figure 3.19, and line profiles, Figure 3.20, to be generated. The pitting that was evident in the SEM images can also be seen in the AFM measurements on all of the planar surfaces. From the line profiles, the period of the grating, the height of the ridges, and the spaces between the ridges was determined by measuring FWHM, and can be seen in Table 3.2. The AFM data confirms

that the surfaces of the AgNPI samples are rougher than those prepared by thermal evaporation of Ag.

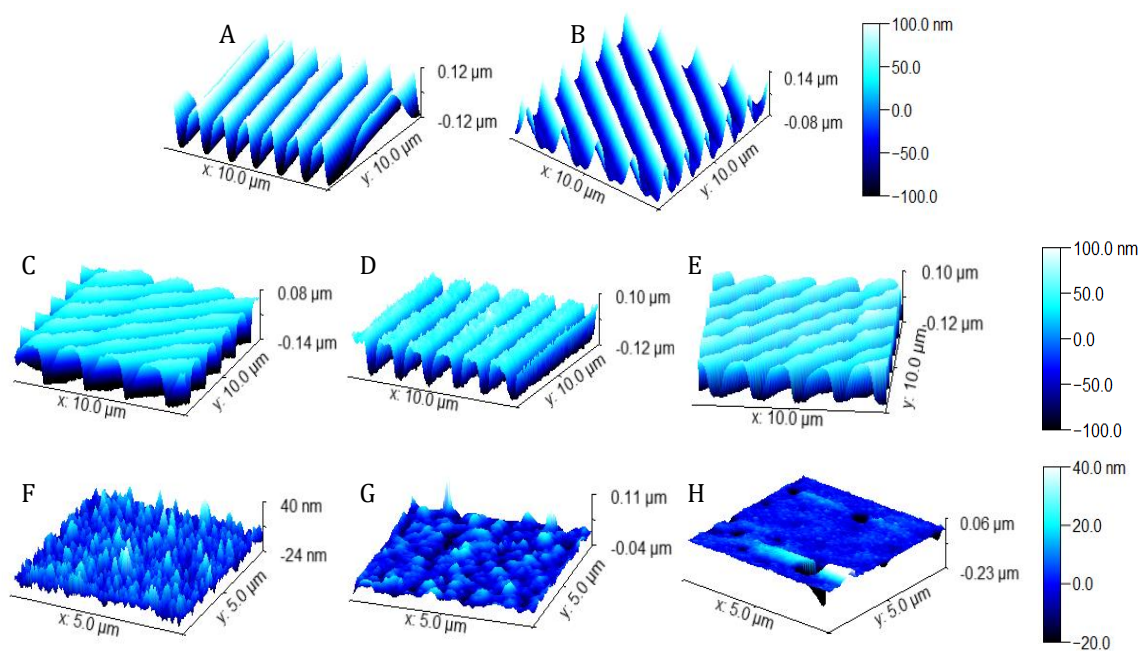


Figure 3.19. AFM 3D Representations of: (A) CD; (B) PDMS mould; (C) AgNPI grating; (D) AgNPI/PMMA grating; (E) TE Ag/PMMA grating; (F) AgNPI planar surface; (G) AgNPI/PMMA planar surface; and (H) TE Ag/PMMA planar surface. All surfaces were fabricated on a glass substrate.

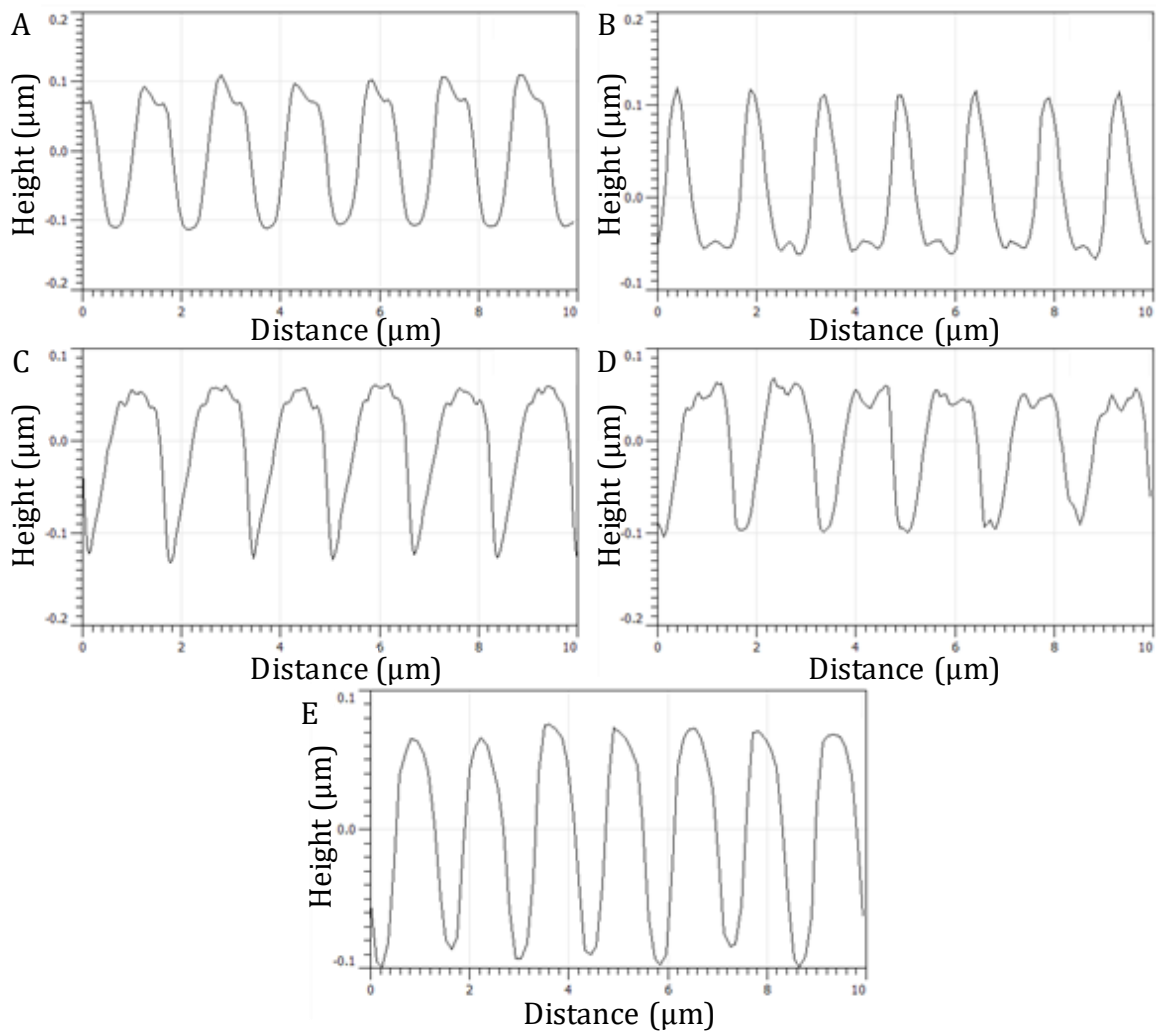


Figure 3.20. AFM Line Profiles of: (A) CD; (B) PDMS mould; (C) AgNPI grating; (D) AgNPI/PMMA grating; and (E) TE Ag/PMMA grating. These line profiles show that a good mould was fabricated from the CD, and successfully transferred. The depth of the grating, as well as the spacing between in each ridge was measured. The PDMS mould appears different to the other profiles because it is the inversion of the CD, and subsequent fabricated surfaced.

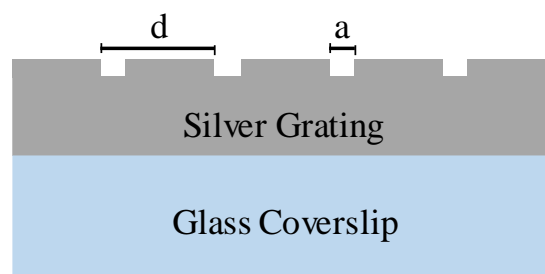


Figure 3.21. Schematic of Silver Grating on a glass substrate, depicting the period, 'd', and the space between the grating ridges, 'a'. These measurements were obtained for each grating, and are shown below in Table 3.1.

Table 3.2 Average Measurements for Grating Obtained from Line Profiles. Average period, d , height, and space between ridges, a , measured using AFM line profiles from Figure 18. To measure the space between grating ridges, the FWHM was used.

	Period, d (μm)	Height (nm)	Space between ridges (nm)
CD Grating (A)	1.52 ± 0.03	210 ± 4	690 ± 20
PDMS mould (B)	1.48 ± 0.03	177 ± 7	901 ± 30
AgNPI Grating (C)	1.49 ± 0.08	188 ± 8	600 ± 30
AgNPI/PMMA Grating (D)	1.69 ± 0.06	155 ± 7	650 ± 20
TE Ag/PMMA Grating (E)	1.45 ± 0.04	150 ± 4	620 ± 20

3.3.2. Optical Characterisation

UV/Visible spectroscopy was carried out on all fabricated surfaces over a wavelength range of 400 to 800 nm, using an integrating sphere detector. Reflectance and transmittance spectra were obtained, and the absorbance spectra was calculated using Equation 3.1, and are shown in Figure 3.20. The reflectance (R) spectrum of a silver planar surface was calculated using Equation 3.2, and compared to experimentally obtained spectra.

$$R = \frac{((n-1)^2+k^2)}{((n+1)^2+k^2)} \quad \text{Equation 3.2}$$

where n and k are the real and imaginary (extinction coefficient) parts of the complex refractive index of silver, respectively [124]. The Ag layer is optically thick, with almost zero transmittance across the spectral range. Looking at the planar surfaces in Figure 3.22 B and 3.22 D show that the reflectance for all samples is lower than for an ideal Ag planar surface, with the reflectance of the TE Ag/PMMA surfaces closest to the ideal case. This surface has significantly higher reflectance than the surfaces fabricated with the NPI. However, while the NPI surfaces show lower reflectance, it has the sample overall trend as a function of wavelength. The reflectance is lowest for the AgNPI/PMMA, and, in contrast with other surfaces, it shows decreasing intensity at longer wavelengths. The lower measured reflectance for the planar surfaces may be attributed to surface roughness, and the presence of the Ag NPs, resulting in higher absorption, as seen in Figure 3.22 D [83].

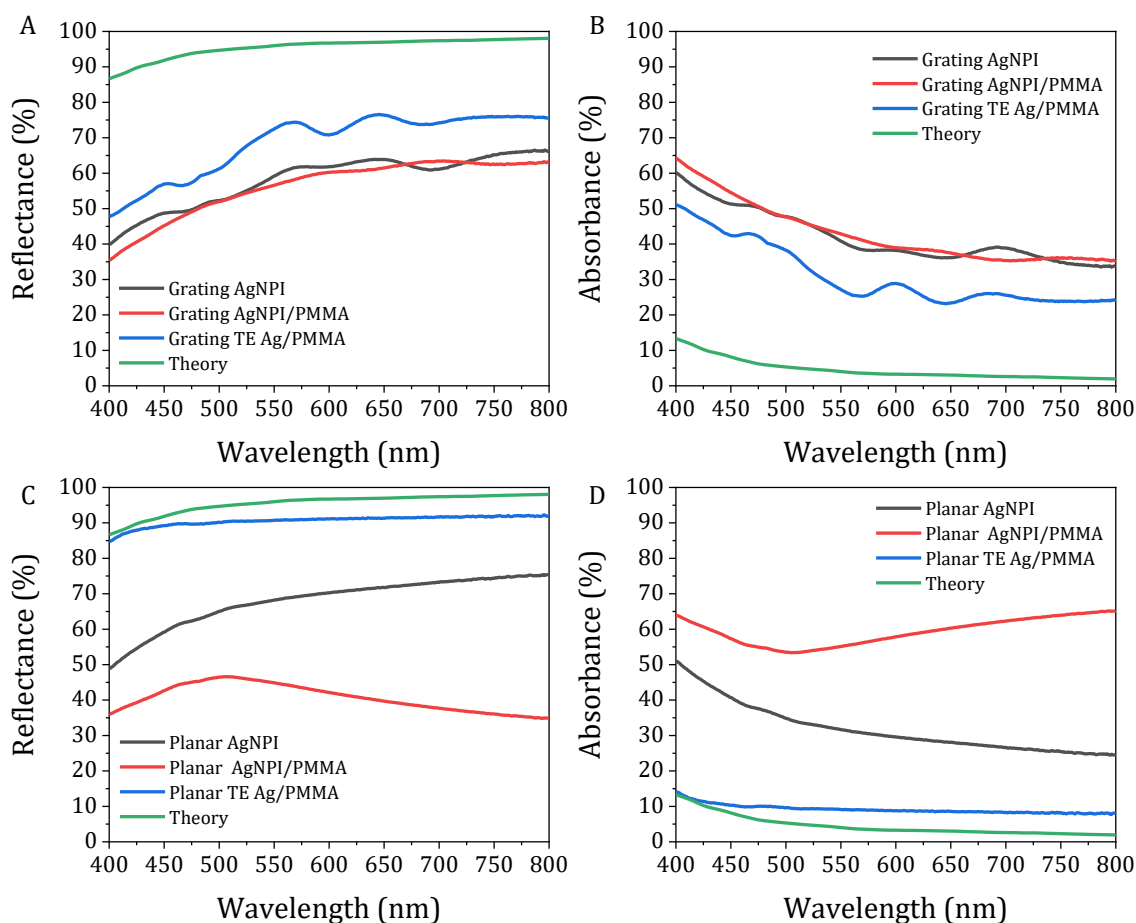


Figure 3.22. UV/Visible Reflectance and Absorbance spectra. (A) Reflectance for grating surfaces; (B) Absorbance for grating surfaces; (C) Reflectance for planar surfaces; (D) Absorbance for planar surfaces; AgNPI fabricated using method (i); AgNPI/PMMA fabricated using method (ii); and TE Ag/PMMA fabricated using method (iii), with theoretical spectra calculated using Equation 3.2.

The grating surfaces have similar spectral dependence, Figure 3.22 A, with highest reflectance observed for the thermally evaporated sample. However, in contrast to the planar surfaces, there is less variation in the overall magnitude of the reflectance and absorbance between the Ag gratings prepared by the different methods. Additionally, peaks and troughs in the spectra of the AgNPI and TE Ag/PMMA grating occurs at similar wavelength, indicating that the gratings are interacting with the incident light in a similar way. The peaks are less well-resolved for the AgNPI/PMMA grating, and occur at different wavelengths, when compared to the other two fabricated gratings. The notable difference between theory and experimental spectra is due to the absorption by the nanoparticles.

The angle dependence of the reflectance spectra, Figure 3.23 C, of the TE Ag/PMMA grating show clear dips in intensity at larger angles, and well-defined peaks that can be seen at small angles. These spectral features are likely due to diffraction by the gratings that reduces specular reflection and/or coupling to propagating surface plasmon modes [125–127]. However, the spectra for the AgNPI grating surfaces, seen in Figure 3.23 A, shows the dips in intensity to be red-shifted and weaker, with little spectral structure evident in the case of the AgNPI/PMMA grating, as seen in Figure 3.23 B. In particular, Figure 3.23 E shows the AgNPI/PMMA planar surface, which shows no significant dependence of the reflectance spectrum. It is notably different to the other two planar surfaces. The shape of the spectrum of the corresponding planar AgNPI/PMMA sample is typical of localised surface plasmon resonance scattering from Ag nanoparticles. This is consistent with the large nanoparticles observed on the surface in Figures 3.17 B and 3.18 B. From the angle resolved data, it is apparent that TE Ag/PMMA (both grating and planar surface) have better optical quality, i.e., high reflectance and well-resolved grating response, when compared to AgNPI and AgNPI/PMMA samples; however, the reflectance of the AgNPI grating shows significantly better optical quality than the AgNPI/PMMA grating.

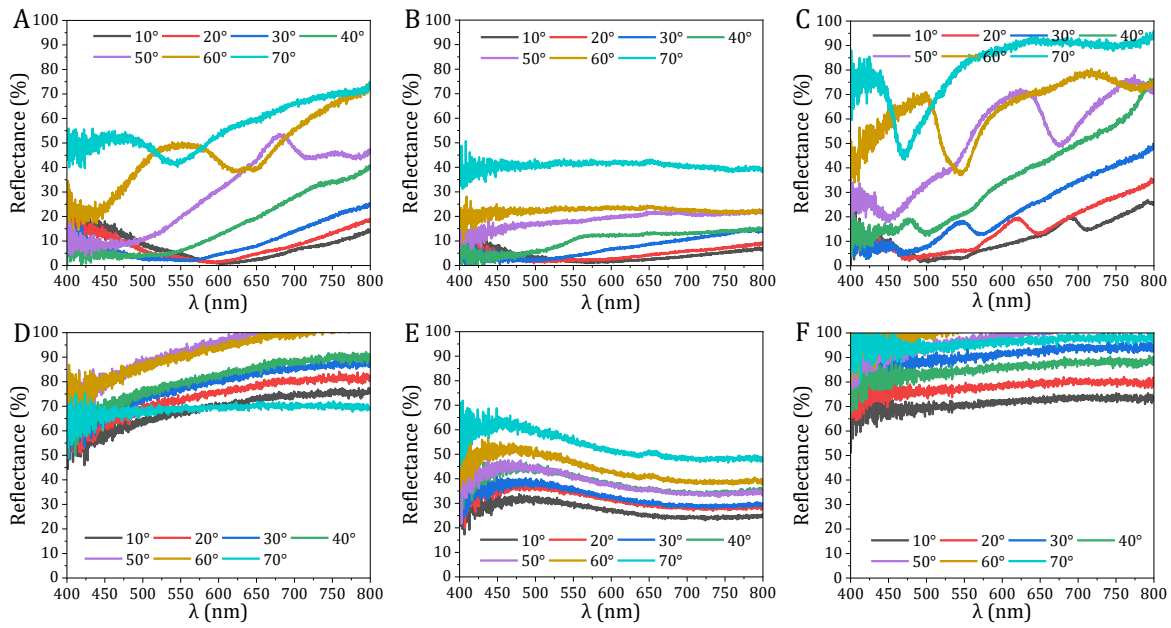


Figure 3.23. Angle Resolved Reflectance Spectroscopy, where specular reflection was measured. Here, the incident angle is kept equal to the detection angle. (A) AgNPI grating; (B) AgNPI/PMMA Grating; (C) TE Ag/PMMA grating; (D) AgNPI planar surface; (E) AgNPI/PMMA planar surface; and (F) TE Ag/PMMA planar surface.

For light-emitting and sensing applications, it is important to assess how the grating modifies the emission of a proximal light-emitting layer. PVK:Flrpic was spin coated onto each sample, with a thickness of 62 nm. Photoluminescence (PL) maps, shown in Figure 3.24, show non-uniform emission over the whole area for AgNPI and AgNPI/PMMA planar surfaces, typical of the effect of surface roughness. More discrete regions of increased emission were observed for the TE Ag/PMMA planar surface, consistent with the pitting observed in the bright-field and SEM images. In the case of the grating surfaces, the PL intensity is highest for the TE Ag/PMMA grating.

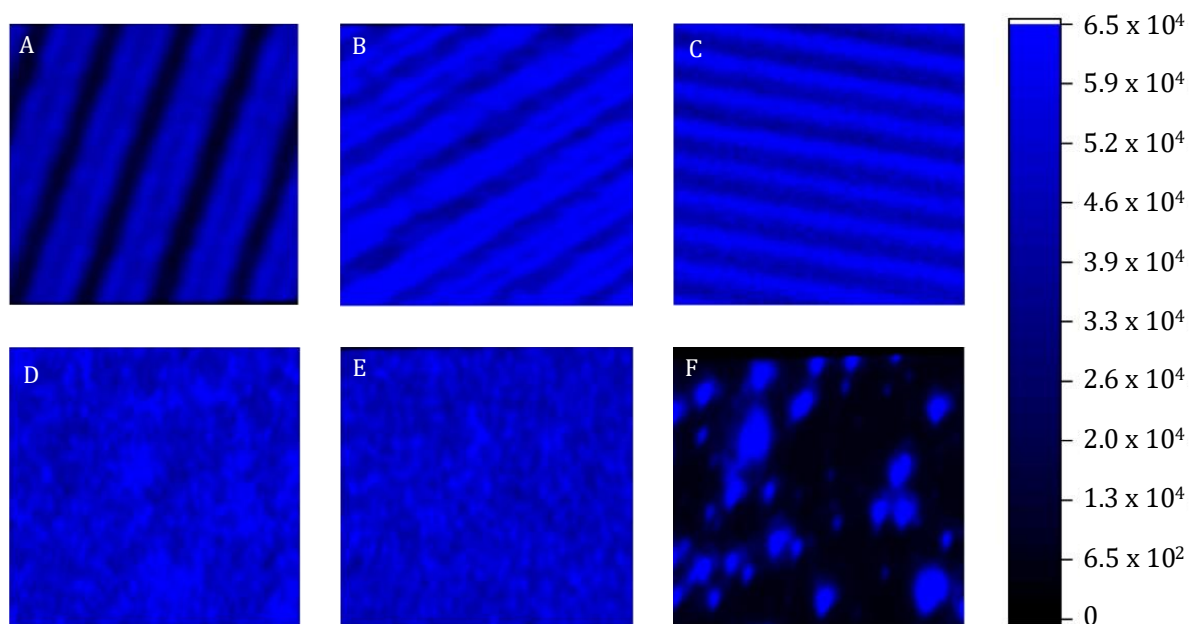


Figure 3.24. Photoluminescence Maps of (A) AgNPI grating; (B) AgNPI/PMMA grating; (C) TE Ag/PMMA grating; (D) AgNPI planar surface; (E) AgNPI/PMMA planar surface; and (F) TE Ag/PMMA planar surface. PVK:Flrpic was spin coated onto each surface

To further compare the effect of the gratings on emission, PL spectra of PVK:Flrpic on the different surfaces are shown in Figure 3.23. A reference spectrum of the photo-emissive layer on a cleaned glass cover slip was also taken for comparison. The emission of the photo-emissive layers is enhanced by a factor of 1.8 on the TE Ag/PMMA grating, and enhanced by a factor of 1.3 on the TE Ag/PMMA planar surface. However, in contrast, the emission is always partially quenched for the AgNPI surfaces, with the AgNPI surfaces quenching more than the AgNPI/PMMA surfaces. In all cases, there is no significant modification of the spectral shape of the emitter. The quenching is consistent with the higher absorbance of the AgNPI surfaces observed in Figure 3.22. In particular, the AgNPI surfaces have Ag nanoparticles with diameters of ~ 10 nm,

which absorb EM energy, but do not scatter efficiently, contributing to these surfaces having the highest quenching.

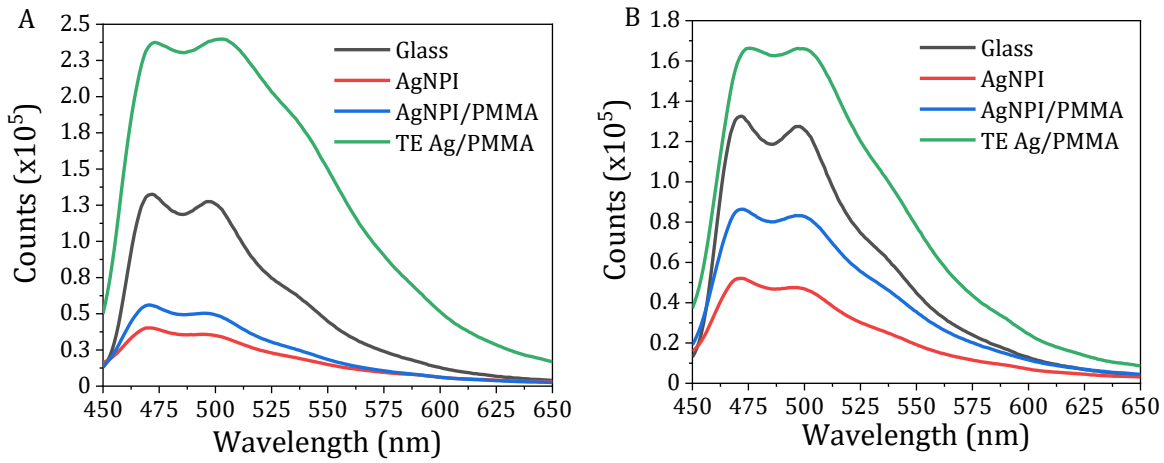


Figure 3.25. Photoluminescence Spectra. (A) Grating surfaces; (B) Planar surfaces, both with a glass cover slip coated with PVK:Flrpic as a reference. Emission correction background subtraction do not modify the shape of the spectra. All NPI surfaces are quench the photo-emissive layer, with the TE surfaces enhancing it.

3.3.3. Electrical Characterisation

Ag grating metasurfaces can play a dual role in optoelectronic devices, allowing for the manipulation of EM radiation as well as being an electrical contact. Known conductivity of the thermally evaporated AG and the AgNPI were compared to those obtained from four-point probe measurements, with the data presented in Tables 3.2 and 3.3. For all methods of fabrication, the conductivity of the grating surface is similar to the planar surface, showing that the formation of the grating structure has not adversely affected the electrical properties. However, it can be noted that the conductivity for all samples using PMMA, which can act as an insulator [128,129], is an order of magnitude lower than for the AgNPI and TEAg surfaces.

Table 3.3. Conductivity Measurements for surfaces fabricated using AgNPI and NIL.

	AgNPI [130]	Grating AgNPI	Planar AgNPI	Grating AgNPI/PMMA	Planar AgNPI/PMMA
Average	3.7×10^7	1.548×10^7	1.347×10^7	2.12×10^6	2.32×10^6
(S/m)		$\pm 0.008 \times 10^7$	$\pm 0.007 \times 10^7$	$\pm 0.01 \times 10^6$	$\pm 0.1 \times 10^6$

Table 3.4. Conductivity measurements for surfaces fabricated using a conventional method.

	Silver [131]	Grating TE Ag/PMMA	Planar TE Ag/PMMA
Average (S/m)	6.3×10^7	$3.74 \times 10^6 \pm 0.02 \times 10^6$	$4.18 \times 10^6 \pm 0.09 \times 10^6$

3.4. Conclusion

A simplified method for the fabrication of Ag thin film grating using silver nanoparticle ink in conjunction with nanoimprint lithography, without the need for specialised equipment, has been investigated. The structural, optical, and electrical properties of the AgNPI have been compared with those fabricated using a more conventional method of NIL in PMMA followed by thermal evaporation of an Ag film. Bright-field microscopy was used to confirm good grating transfer using different fabrication methods. Further analysis of the surfaces made with the AgNPI had a rougher surface, as seen in SEM and AFM 3D representations and line profiles, and those fabricated with AgNPI/PMMA showed a larger variance in nanoparticle size. Surfaces fabricated using AgNPI also showed lower reflectance, and higher absorption, in particular, for the AgNPI/PMMA sample. The presence of the Ag nanoparticles also resulted in PL quenching of a proximal emitting layer. Grating AgNPI surfaces showed an increased conductivity compared with ideal planar Ag but the use of PMMA resulted in an order of magnitude decrease in the conductivity for both AgNPI/PMMA and TE Ag/PMMA surfaces. The grating structures did not adversely affect the conductivity compared with planar surfaces for any of the fabrication methods investigated. It can be concluded that using AgNPI shows promise for the fabrication of Ag structured thin films, and may be useful for upscaling, for example in roll-to-roll processes. The use of PMMA could be eliminated from the fabrication method as it adds an extra step to the process, and does not enhance any characteristics of the Ag grating thin films [132].

Chapter 4 Assessing Nanobiomaterial (NBM) Interactions and Trafficking in Three-Dimensional Hepatic Spheroids over Time Using Confocal Microscopy

Currently, the gold standard for assessing toxicity of nanobiomaterials (NBMs) is by using a 2D *in vitro* model, and whilst these are standardised, they have often been shown to be inaccurate predictors of human toxicity and the fate of NBMs within the body. This is due to the highly simplistic nature of 2D *in vitro* models, and the absence of the physiological processes required to transport the NBMs through the cells [40,42,43]. Recently there has been a move towards 3D *in vitro* models, which can mimic human organs, and more accurately predict toxicity. These 3D models, however, are not yet standardised and much work must be done to validate them. Studies using flow cytometry have characterised the uptake and penetration of NBMs, polystyrene NPs as well as metallic and magnetic NPs as drug delivery systems in colorectal cancer spheroids, murine fibroblast and mouse melanoma spheroids [105,106]. Using confocal microscopy and fluorescent labelling (secondary antibodies) [133] indirect imaging techniques have been used to evaluate the hepatotoxicity of metallic nanoparticles [50–52]. Two-photon photoluminescence microscopy has also been used to analyse the uptake of gold NPs in colorectal monolayers and spheroids showing that results seen in 2D *in vitro* models were not indicative of behaviour noted in 3D models, and that small, spherical nanoparticles efficiently penetrate to the core of spheroids [134].

Other qualitative techniques have been used, including bright-field microscopy (which is low-cost, and non-destructive) or scanning electron microscopy (SEM), environmental SEM, or transmission electron microscopies, which are all time consuming, expensive, and require sample preparation that is destructive to the spheroid [135,136]. However, confocal microscopy is highly sensitive, non-destructive and allows for 3D reconstructions [137,138]. Using confocal microscopy also allowed for fluorescence lifetime imaging microscopy (FLIM) to be carried out.

Flow cytometry and confocal microscopies are typical analysis techniques used for fluorescence detection. However, recent advances in imaging techniques for assessing the effective delivery of novel drugs and NMBs has led to visualisation of the uptake and quantitatively analysing biological information. Fluorescence lifetime imaging microscopy (FLIM) is one such technique. FLIM measures the lifetime of a fluorophore, i.e., the average rate of decay of a fluorophore, from the excited state to the ground state, where it will release a photon. FLIM has been successfully used to study drug delivery, including intracellular doxorubicin release [118,139,140], while other studies have used FLIM to visualise nanoparticle uptake and subcellular trafficking [46,141,142].

In previous work by Tutty *et al.*, an indirect imaging protocol was used to locate LipImage, where cells were fluorescently tagged using a primary, and then appropriate secondary antibody, i.e., anti-PEG primary antibody, and Alexa Fluor-488 goat anti-mouse secondary antibody [143]. Alexa Fluor-488 was then excited using a 488 nm laser, with peak emission at 525 nm [144]. This protocol is similar and comparable to that used for poly(ethyl-butyl cyanoacrylate) nanoparticle (NP) (PACA). However, LipImage™815 is a near-IR dye, which has an optical window that has low signal to noise, low autofluorescence and causes minimal damage to surrounding tissues, and can be used for deep tissue imaging [145]. In this work, direct imaging method using confocal microscopy was used to localise NMBs within the core of a 3D hepatic cell culture model. Using excitation and emission wavelengths of $\lambda_{ex}/\lambda_{em}$ 740/830 nm [146] for LipImage™815, a direct imaging method can be achieved, which reduces the complexity of the sample preparation protocol, and takes advantage of the benefits of using a near-IR dye, with a view for use of the method in assessing the toxicology of NMBs, an application which is beyond the scope of this work.

4.1. Materials and Methods

Liver spheroids, cultured from 1000 Hepatocellular carcinoma (HepG2) cells, were kindly provided by Dr Melissa Anne Tutty at Nanomedicine Group, and Laboratory for Biological Characterization of Advanced Materials (LBCAM), TTMI, Trinity College Dublin, St. James's Hospital, Dublin 8. All protocols for cell culture, NBM characterisation, formation, and characterisation of spheroids, and exposure of spheroids to NMBs, is described in detail in the following sections.

4.1.1. Chemicals

All chemicals were purchased from Sigma Aldrich, Ireland, unless otherwise specified in the test.

4.1.2. NBM Preparation

Two dye-loaded NBMs, both with applications in drug delivery and deep tissue imaging, were used in this study:

1. LipImage™815, a liposome which encapsulates the near-infrared lipophilic fluorescence dye IR780, and
2. A poly(ethyl-butyl cyanoacrylate) nanoparticle (PACA), loaded with the far-red dye, NR668.

From this point on, LipImage™815 will be referred to as LipImage, and NR668-PACA will be referred to as PACA.

LipImage was kindly provided by CEA-LETI (Grenoble, France) at a particle concentration of 95 mg/ml (9.5%) in 154 mM NaCl and a dye concentration (HPLC) of 239.5 μ M (252 μ M/100 mg particle). The diameter of LipImage was 80 nm, and the dispersion media used was 154 mM NaCl and ascorbic acid (1.75 g/l). LipImage was sterile and endotoxin free, with an endotoxin quantity of < 1 IU/ml, within acceptable endotoxin levels.

PACA nanoparticles were provided by SINTEF (Trondheim, Norway). They were synthesized under aseptic conditions, by mini-emulsion polymerization, at a concentration of 105 mg/ml HCl in sterile, distilled water. Equipment used to synthesize the nanoparticles was autoclaved, and all solutions were sterile, and filtered before synthesis. An oil phase was prepared, which consisted of poly(ethyl-butyl cyanoacrylate) (PEBCA) (Quantum Medical Cosmetics) which contained 2 wt.% Miglyol 812 (Cremer) and 10% vanillin. NR668 (modified Nile Red), via custom synthesis from SINTEF [147], was added to the oil phase for dye loading. An aqueous phase was added to the oil phase, that consisted of 0.1 M HCl containing two PEG stabilisers (Brij®L23 and Kolliphor®HS15, both Sigma Aldrich, 5% wt. of each). The oil and water phases were mixed and immediately sonicated for 3 min on ice (six 30 s intervals, 60% amplitude, Branson Ultrasonics digital sonifier). The solution was rotated at 15 RPM for 12 h, and at room temperature (RT). The pH was adjusted to 5.0 for 5 h, at RT to

allow for further polymerisation. Unreacted PEG was removed before being characterized, by dialyzing the dispersions (Spectra/Por dialysis membrane MUCO 100.000 Da) against 1 mM HCl.

4.1.3. NBM Characterisation

Nanoparticle tracking analysis (NTA) was used to assess NBM hydrodynamic diameter, using NS500 Nanosight (Software Version 3.2) (Malvern-Panalytical, UK), according to protocols in the Laboratory for Biological Characterization of Advanced Materials (LBCAM) [148,149], which are now well established validated protocols for NBMs under the European Nanomedicine Characterisation Laboratory (EUNCL) [150].

NBMs were prepared as standard and diluted to 1:5000 and 1:100,000 using D-PBS buffer (MgCl₂ and CaCl₂). The particles were visualised using a 405 nm laser, with 60 s recordings captured using a EM-CCD camera, with the focus manually controlled. The detection level, manually selected, and set to 3. The recordings were analysed using Nanosight (v3.2) to determine the number of particles per frame, and the particle size. AuNP (gold) citrate nanoparticles, of known size, were used as a reference. Dynamic Light Scattering (DLS) was also carried out using Zetasizer Nano ZS system (Malvern, UK), running Zetasizer software (v7.13), and using the EUNCL approved PCC-001 SOP 'Measuring Batch Mode DLS' [150]. A DTS0012 disposable cuvette was loaded with the sample suspended in D-PBS buffer, using a pipette to ensure adequate mixing. As per the EUNCL SOP, the cuvette was subjected to 300 s equilibrium time. Twelve 10 s runs per measurement were recorded for the sample, which was subjected to 10 measurements, with a zero second delay between measurements. Automatic attenuation selection, general-purpose analysis mode, optimum positioning, and backscatter angle (173° NIBS default) were chosen.

4.1.4. Cell Culture

For all experiments described here, the immortalised human liver hepatocellular carcinoma (HepG2) cell line, supplied by SINTEF, was used. HepG2 cells were maintained in low glucose Dulbecco's Modified Eagles Medium (DMEM), supplemented with 10 % foetal bovine serum (FBS), and 1% Penicillin Streptomycin (all supplied by Gibco, Invitrogen Ltd., VWR), and maintained at 37 °C and 5 % CO₂, in a T75 flask. In accordance with ATCC guidelines, all cell generations were restricted to between 10 and 20 passages to avoid the formation of vacuoles. Once 80 % confluence was reached,

cells were detached from the T75 flask by trypsinizing them using Tryp1E™ (Gibco, Invitrogen, Oregon, USA), centrifuging them, and resuspending the cell pellet in 1 ml of culture medium.

4.1.5. Cultivation of HepG2 Cells and Preparation of HepG2 Spheroids

HepG2 cell monolayers and spheroids were cultured as per the protocol detailed by Tutty *et al.* [143]. After the cells had been resuspended, as described in § 4.1.4, they were counted, using a Countess automated cell counter (Thermo Fisher, Ireland). To form spheroids, the cells were seeded in CellStar® 96 well ultra-low attachment (ULA) cell repellent plates (Grenier, BioOne, UK) at a density of 1000 cells per well in 100 µl of culture medium. Figure 4.1 shows a schematic of HepG2 spheroid formation in CellStar® 96 well ULA cell repellent plates. After three days of incubation at 37 °C, and 5 % CO₂, the medium was changed, with great care taken not to disturb the spheroids. After 1 week, the spheroids have a diameter of approximately 300 µm, and were taken for further analysis or exposed to NBMs.

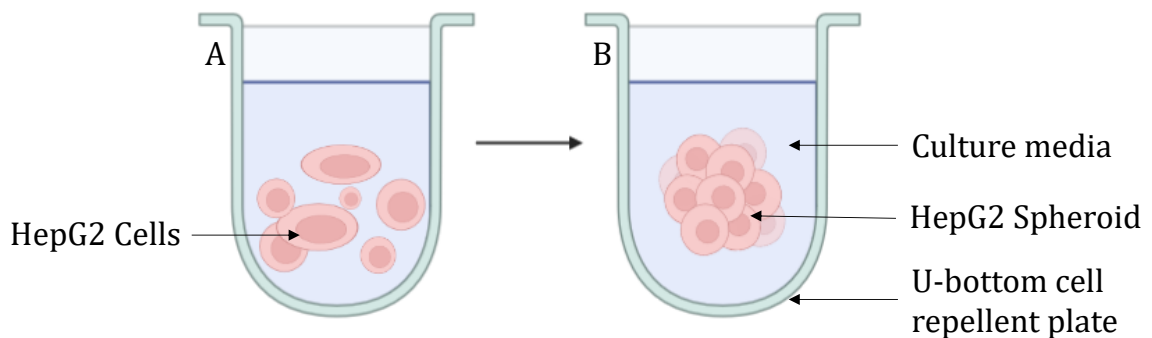


Figure 4.1. Schematic of HepG2 spheroid formation in CellStar® cell repellent plates. (A) Single cells are seeded into non-adherent round bottom wells. (B) After 6 h cells cluster together to form cell spheroids.

4.1.6. Morphological Assessment of HepG2 Spheroids

Morphological assessment of the spheroids was carried out using bright-field microscopy. This allowed for the assessment of spheroid growth, morphology, and allowed spheroid sizes to be calculated across a month-long culture period. Using an epifluorescent microscope (Nikon TE300), equipped with a 10X objective, and QCapture imaging software, (QImage, v7.0.0), images of spheroids were captured, with all image processing and analysis carried out using ImageJ (v1.53t) [151].

Assessing the internal structure and the health of hepatic spheroids was carried out using histological analysis. Spheroids were prepared by washing with phosphate-buffered saline (PBS) and fixed for 1 h in 4 % paraformaldehyde (PFA), before being embedded in plastic moulds using 2 % electroendosmosis (EEO) agarose in d-PBS. Increasing the concentration of ethanol (EtOH) (20 %, 40 %, 60 % EtOH in H₂O) dehydrated the agarose block, which were subsequently embedded in paraffin using a tissue processor by Dr Gavin McManus (Trinity Biomedical Science Institute, Trinity College Dublin, Ireland). The paraffin blocks were sectioned using a microtome, and then stained with Haematoxylin and Eosin (H&E) staining to identify shape and structure of cells in the spheroid, shown in Figure 4.2. To stain with H&E, the spheroid section slides were required to be dewaxed, and then rehydrated using the following protocol:

- Xylene for 5 min
- Xylene for 4 min
- 99% industrial methylated spirits (IMS) for 3 min
- 90% IMS for 2 min
- 70% IMS for 1 min
- Wash under cold water for 1 min

The slides were then submerged in Haematoxylin for 5 min before being removed and again rinsed under cold water for 1 min. To remove excess stain and define the nuclei, slides were subsequently dipped in acid alcohol (1%) for 2 s and rinsed under tap water for 30 s before staining with Eosin for 5 min. Eosin is a highly water soluble stain, therefore care is needed when briefly rinsing in tap water.

Sections were then dehydrated and cleared using the following protocol:

- 70% IMS for 1 min
- 90% IMS for 1 min
- 99% IMS for 2 min
- Xylene for 3 min
- Xylene for 3 min

Slides were then mounted using DPX mounting media, and covered with a cover slip added at a 45° angle. Stained tissue sections were then imaged by Epifluorescent

microscopy (Nikon TE300, equipped with a 10X objective and QCapture Software QImaging). Image analysis was performed by ImageJ software. The H&E stained spheroid is presented in Figure 4.2, and shows no necrotic core visible.



Figure 4.2. *Internal spheroid structure and morphology. Spheroids were cultured for 7 days before being fixed in PFA and suspended in agarose, dehydrated in increasing concentrations of ethanol, paraffin embedded, sectioned and stained with H&E. This image is representative of the spheroids used, and show a mid-section of the spheroid. Image was taken by Dr Melissa Anne Tutty of the nanomedicine group, Trinity College Dublin.*

4.1.7. Exposure to NBMs

Stock NBM suspensions were vortexed and appropriate dilutions were made in cell culture medium. For NBM exposures, cell culture medium was removed from the wells and the well was washed with pre-warmed PBS, and then exposed to the NBMs .

For LipImage, spheroids were exposed to 200 $\mu\text{g}/\text{ml}$, and for PACA, spheroids were exposed to 30 $\mu\text{g}/\text{ml}$, and were exposed for 24 h, 48 h, and 72 h. The rationale behind these concentrations and exposure times was to allow adequate time for NMBs to penetrate to the core of the spheroid.

4.1.8. Immunofluorescent Staining

Prior to imaging, both 2D monolayers, and 3D cultures were stained using appropriate dyes. Table 4.1 shows the stains, and concentration used for each NBM. Before staining the 2D monolayers and 3D spheroids, culture medium was removed, and the cell layer was washed with pre-warmed PBS. Samples were then:

- Fixed in 3.7 % PFA for 10 min at RT,
- Permeabilised with 0.1 % Triton X-100 in PBS for 10 min, and
- Blocked in 1 % BSA in PBS for 1 h.

The nuclei and actin were stained using Hoechst (1:1000) and rhodamine phalloidin (1:50) (both Invitrogen, Fisher Scientific, Ireland), respectively, for 1 h, at RT, and in a dark room. PACA was loaded with NR668 (Nile Red), which is a fluorescent molecule that emits in the red region. To avoid overlapping of the emission spectra, rhodamine phalloidin, which similarly emits in the red region of the visible spectra, was omitted from the staining protocol for PACA monolayers and spheroids. After staining was completed, the samples were washed in pre-warmed PBS and mounted on Ibidi μ -Slide angiogenesis slides (Ibidi GmbH, Germany), using Slow Fade™ Gold Antifade Mounting media (Thermo Fisher, Ireland).

Table 4.1. Immunofluorescent Stains used for confocal microscopy.

NBM	Hoechst (1:1000)	Rhodamine Phalloidin (1:50)
LipImage	✓	✓
PACA	✓	x

4.1.9. Confocal Microscopy

Bright-field microscopy was used to focus on the widest section of the spheroid, as illustrated in Figure 4.3. The widest point of the spheroid is assumed to be the centre, or close to the centre of the spheroid. In this focal plane all confocal fluorescence microscopy was carried out. Confocal microscopy was performed using the MicroTime200 (PicoQuant GmbH, Germany). The MicroTime200 uses an Olympus IX71 inverted microscope. All images were acquired using picosecond pulsed diode laser excitation sources (PDL 800-B, PicoQuant GmbH, Germany), with a repetition rate of 40 MHz. Samples were excited with excitation wavelengths of 405 nm, 470 nm, and 730 nm, at optical powers of 0.4 μ W, 5 μ W, and 0.8 μ W respectively. The emission was collected using an Olympus UPlanFL N 100X/1.30 oil immersion objective. The pinhole size was set to 75 μ m. Different optical filters were used to spectrally separate the emission of the different fluorophores, and NBMs, including 450 nm and 750 nm long

pass filters, and $550 \text{ nm} \pm 20 \text{ nm}$ and $600 \text{ nm} \pm 20 \text{ nm}$ band-pass filters. The 450 nm long pass filter was used to measure the fluorescence from Hoechst, the $550 \text{ nm} \pm 20 \text{ nm}$ was used to measure the fluorescence from rhodamine phalloidin. PACA and LipImage were measured using the $600 \text{ nm} \pm 20 \text{ nm}$ band-pass filter and 750 nm long pass filter, respectively. $300 \text{ px} \times 300 \text{ px}$ ($80 \times 80 \text{ }\mu\text{m}^2$), images were acquired using single-photon avalanche diode (SPAD) detectors, with a dwell time of 0.6 ms per pixel, and a resolution of $0.267 \text{ }\mu\text{m}$. Intensity images were saved via SymPhoTime, PicoQuant's data acquisition and analysis software, as data files.

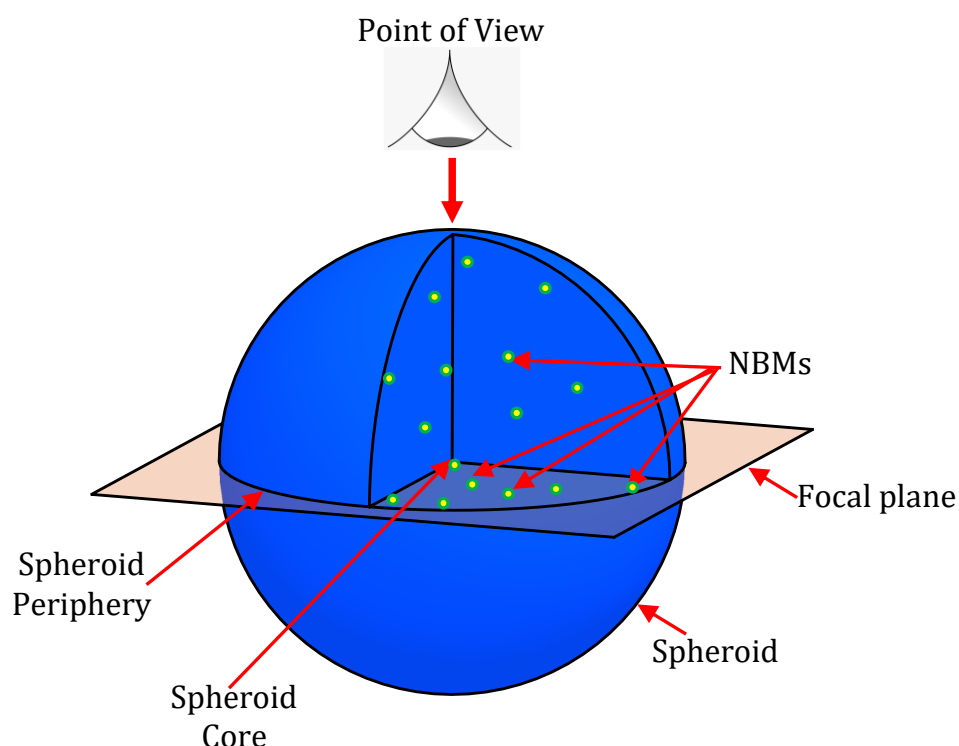


Figure 4.3. Schematic of spheroid (blue), and imaging plane (orange) where the images are acquired, allowing localisation of NBMs from periphery to core to be assessed. Bright-field microscopy is used to focus on the widest section of the spheroid, which will be approximately the centre of the spheroid.

Image analysis was carried out on the recorded intensity data. Figure 4.4 shows a flow chart of the treatment of the images. Images were saved as ASCII text files, and were converted to .tiff images. From these, 16-bit raw intensity images, and 8-bit greyscale images were created. The 8-bit images are contrast enhanced, allowing the images to be manually stitched together. The spatial coordinates of the stitched images were measured from the manually stitched images. These coordinates were used, with a bespoke Python code, to automatically stitch the 16-bit raw intensity images together.

During image acquisition, the NBMs are prone to photobleaching. As some images are exposed several times as shown in Figure 4.5, an automated image stitching tool was not deemed practical for stitching images together for this work.

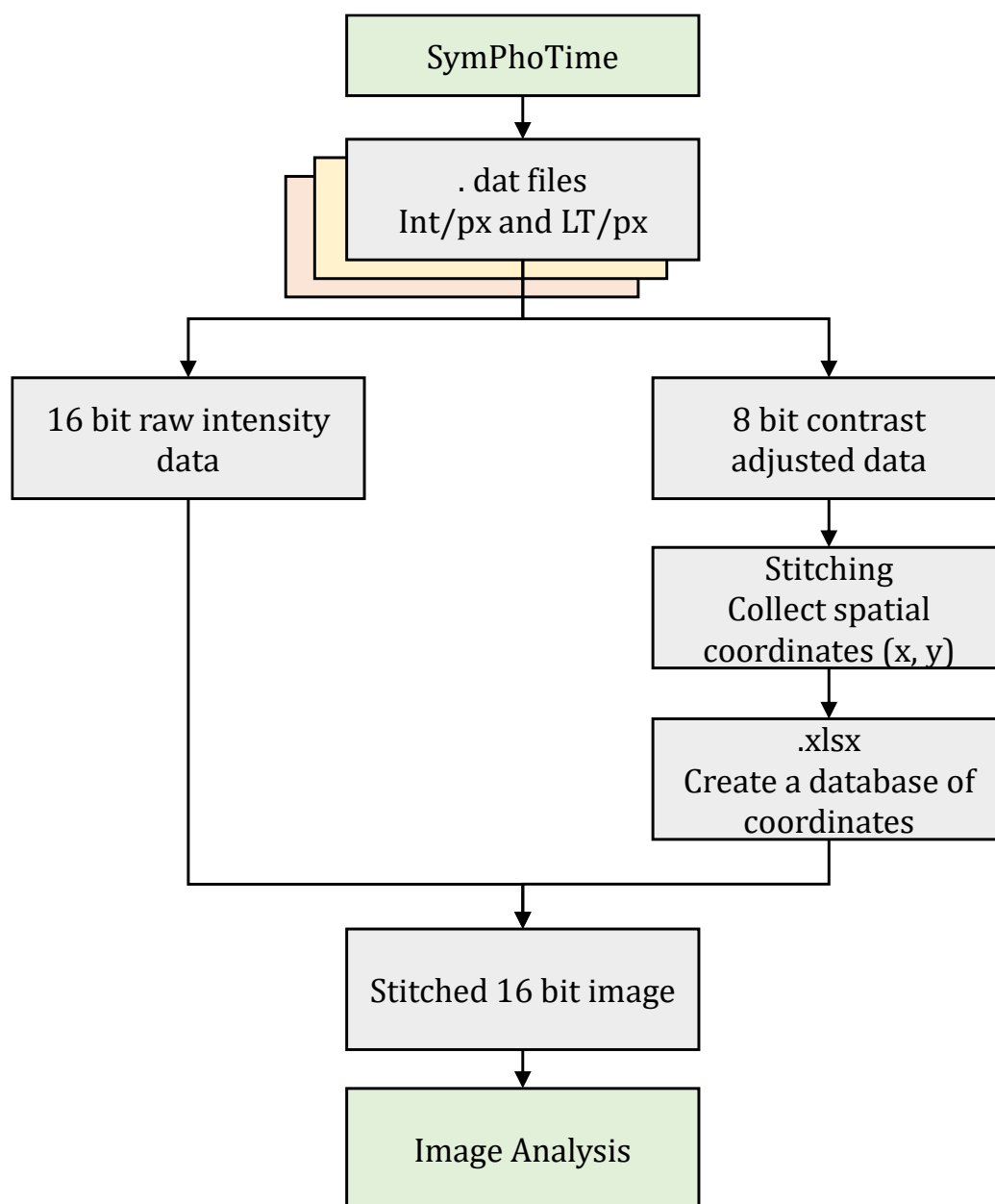


Figure 4.4. Flow Chart describing the treatment of images. Images were acquired using SymPhoTime. Images were saved as ASCII text files. These text files were converted to .tiff images and were saved as 16-bit raw intensity images, and 8-bit greyscale images, which were contrast enhanced to enable stitching. Images were manually stitched together, and the spatial coordinates (x, y) were collected. A database of the coordinates was created, and using a bespoke python code, the 16-bit raw intensity images were stitched together, and subsequently used for image analysis.

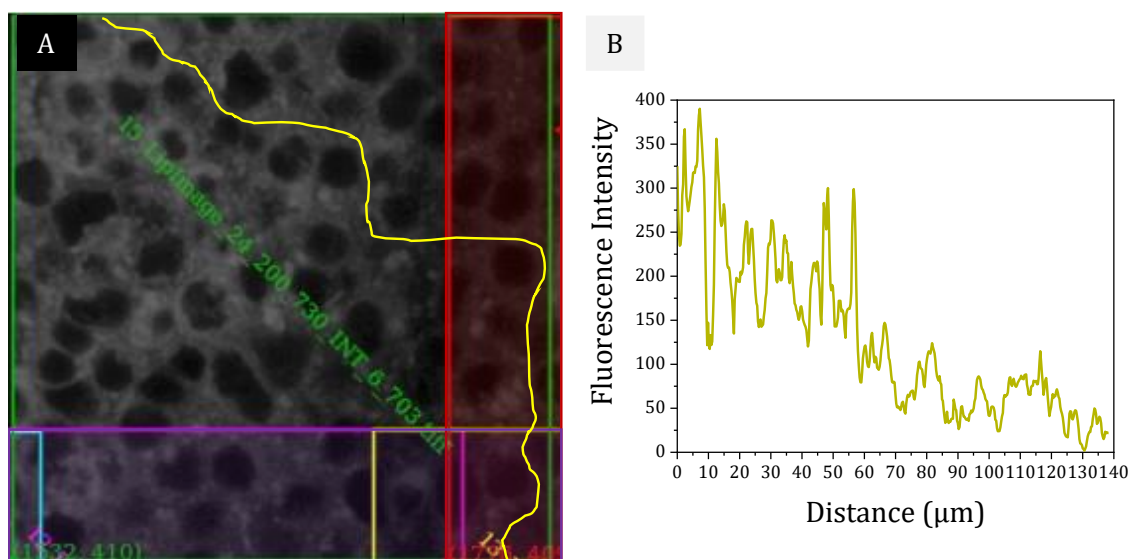


Figure 4.5. Photobleaching effect on LipImage. (A) In ImageJ, the free hand tool is used to draw a line across the image, where the NBM LipImage is located. This trace, shown in yellow, goes from an area that has been imaged once, to an area imaged twice (located in the red and purple boxes), and finally into an area that has been imaged three times (located where there is an overlap of red and purple boxes). (B) The line trace was plotted, and shows the decrease in fluorescence intensity, i.e., the effect of photobleaching on LipImage.

4.1.10. Fluorescence Lifetime Imaging Microscopy

Fluorescence Lifetime Imaging Microscopy (FLIM) was carried out at the same time as confocal imaging, as described in § 4.1.9. The confocal set up, as described, was coupled with a time-resolved single photon counting (TCSPC) unit (PicoHarp 300 Picosecond Histogram Accumulating Real-time Processor, PicoQuant GmbH, Germany), and the pulsed laser diode, allowed time-resolved measurements to be performed. This set up was controlled by, and analysis carried out using the SymPhoTime software from PicoQuant. Normalised decay curves were plotted, and fitted with a one- or two-exponential nonlinear function, using the following equations:

$$y = y_0 + A_1 e^{-x/\tau_1} \quad \text{Equation 4.1}$$

$$y = y_0 + A_1 e^{-x/\tau_1} + A_2 e^{-x/\tau_2} \quad \text{Equation 4.2}$$

where A_1 and A_2 are the amplitudes and τ_1 and τ_2 are the slow and fast decay times, respectively. Using amplitude and decay times, Equation 4.3 was used to calculate the amplitude weighted average lifetime of the NBMs for a one-exponential fit, and Equation 4.4 was used to calculate the lifetimes for a two-exponential fit:

$$\tau_{average} = \frac{A_1\tau_1^2}{A_1\tau_1} \quad \text{Equation 4.3}$$

$$\tau_{average} = \frac{A_1\tau_1^2 + A_2\tau_2^2}{A_1\tau_1 + A_2\tau_2} \quad \text{Equation 4.4}$$

The choice of fitting was determined by the residual trace, and the chi-squared values [152]. Initially, the normalised decay was fitted with a one-exponential nonlinear decay fit. If the fit was acceptable, there should have been no trend seen in the residual trace. If a trend was seen, as shown in the red box of Figure 4.6, for example, then the number of exponentials was increased, until no residual trend was seen. A good fit would show a residual trace with no trend as seen in the green box in Figure 4.6.

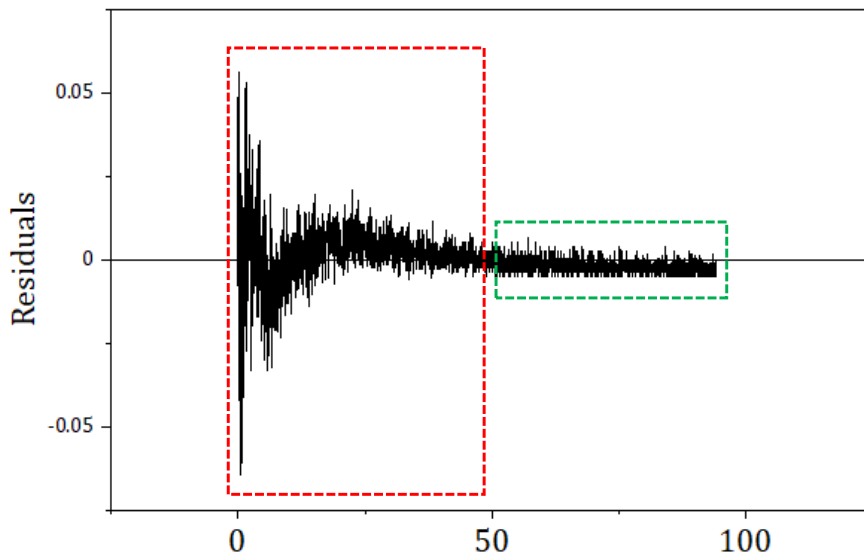


Figure 4.6. Residual trace from exponential decay nonlinear curve fit. For an acceptable fit, no trend should be seen in the residual trace, as is shown in the green box. A fit is deemed unacceptable if residual trends are seen, shown in the red box. When this occurs, the exponential is increased until the residual trends disappear.

4.2. Results and Discussion

4.2.1. Characterization of NBMs

To determine if the chosen NBMs remain stable during shipment, characterization was undertaken of both NBMs prior to any further experimentation, with results compared to characterization data from the supplier.

4.2.1.1. Hydrodynamic Diameter

Studies have shown that both size and shape greatly influence the uptake profiles of NBMs in solid tissues/tumours, as well as NBM-induced toxicity [153–156]. The potential of a NBM formulation to be internalised into cells, and spheroids, is directly dependent on its size. Therefore, LipImage, and PACA were carefully characterized within the LBCAM using conventional nano-characterization techniques and validated protocols. The data obtained was then compared to the data supplied by the supplier.

In line with the EUNCL developed protocols for NBM size and concentration characterisation, analysis was carried out using Nanoparticle Tracking Analysis (NTA) and Dynamic Light Scattering (DLS). The results of this analysis, for both LipImage and PACA can be seen in Tables 4.2 and 4.3, respectively. The data obtained from the characterisation undertaken in-house is in close agreement with values provided by the supplier.

Table 4.2 Summary and comparison of characterization data by NTA and DLS for LipImage.

LipImage	Supplier Values	Measured Values
Mean hydrodynamic size (DLS)	52.2 nm	50.72 nm
Mean hydrodynamic size (NTA)	Not provided	72.7 nm
Polydispersity Index (PDI) (DLS)	<0.102	0.11

Using NTA, a mean of 50.72 nm was reported, with DLS reporting a mean of 73 nm. PDI obtained from DLS is 0.11, making LipImage monodispersed.

Table 4.3. Summary and comparison of characterization data by NTA and DLS for PACA.

PACA	Supplier Value	Measured Values
Mean hydrodynamic size (DLS)	178 nm	164.7 nm
Mean hydrodynamic size (NTA)	Not provided	140 nm
Polydispersity Index (PDI) (DLS)	0.28	0.18
Zeta Potential	-3.6 mV	Not provided

PACA was also analysed using NTA and DLS. Here, NTA reported a mean size of 140 nm, with DLS reporting a mean of 165 nm. The PDI, obtained from DLS, is 0.18, also making PACA monodispersed. The supplier also noted that DLS analysis measured an average zeta potential of -3.6 mV at pH 7, making PACA neutral.

4.2.1.2. HepG2 spheroid culture and characterisation

Tutty *et al.* have previously assessed hepatic spheroids growth over a 31-day culture period [143]. The diameter of HepG2 spheroids gradually increased over the culture period, with spheroids maintaining a spherical and uniform shape throughout. After approximately 6 h in culture, HepG2 cells began to loosely compact to form loose spheroids. These structures further compacted to form fully intact spheroids after 3 days. A seeding concentration of 1,000 cells per 100 μ L culture medium caused the formation of uniform, circular spheroids that were of consistent morphology, and had diameters ranging from 290 μ m \pm 10 μ m after 3 days, to 650 μ m \pm 17 μ m after 31 days.



200 μm

Figure 4.7. Representative Bright-field microscopy image of HepG2 spheroid. Spheroids were formed from a cell seeding concentration of 1,000 cells per 100 μL culture medium and cultured in CellStar® cell repellent plates for 7 days. At this point in time the spheroids show defined edges, and good shape. This image was taken by Dr Melissa Anne Tutty of the nanomedicine group, Trinity College Dublin.

In this work HepG2 spheroids were cultured using CellStar® cell-repellent plates, chosen as they are easily acquired, standardised, and spheroids can be easily reproduced using them [157,158]. The HepG2 spheroids were formed by the aggregation from a single cell in each well. After 7 days the formed spheroids were characterised using bright-field microscopy, as shown in Figure 4.7, which showed well-formed spheroids, with clear, defined edges, and a circular shape.

4.2.3. Liposome Stability

Evaluation of the stability of the liposome in LipImage was carried out. It was already shown that shipment of the product had no adverse effect, shown in Table 4.2, however, treatment times, and repeated imaging may cause instability in the liposome layer. Using 2D monolayers of HepG2 cell treated with 200 $\mu\text{g}/\text{ml}$ of LipImage, weekly confocal images were acquired. Three cells, on a single microscope slide, were selected. Using a custom built slide position selector that was mounted to the microscope stage, shown in Figure 4.8, and housed the microscopy slide, the cells positions on the slide were noted to allow them be repeatedly imaged, over a three-month period. The **C**orrected **T**otal **C**ell **F**luorescence (CTCF) was calculated for each image, using the following equation:

$$CTCF = \sum I_C - A_C \bar{I}_B$$

Equation 4.5

where

I_C is the integrated fluorescence intensity of the cell,

A_C is the area of the selected cell, and

\bar{I}_B is the mean fluorescence intensity of background readings.

The CTCF monthly measurements show a decrease in intensity over the three-month period, shown in Figure 4.9B for each cell, shown in Figure 4.9A. At the same time, two random cells were also selected each week, and their CTCF was also calculated. This showed no pattern in the CTCF, suggesting the decrease in intensity observed in the repeatedly imaged cells is due to photobleaching, rather than a degradation of the liposome. Photobleaching can also occur in cells within the locale of the cell being imaged. Scattering of light from an illuminated area can affect cells within a 90 μm radius of the area being imaged, causing photobleaching and phototoxic effects [159], which is why, when selecting cells for repeated imaging, not only were ones with distinctive shapes chosen, but distance from each other was taken into consideration. It can, therefore, be determined, that once the cell is fixed, the NBM is relatively stable. This allows for samples to be revisited at a later time, if further imaging is required, once samples are stored in a suitable manner.

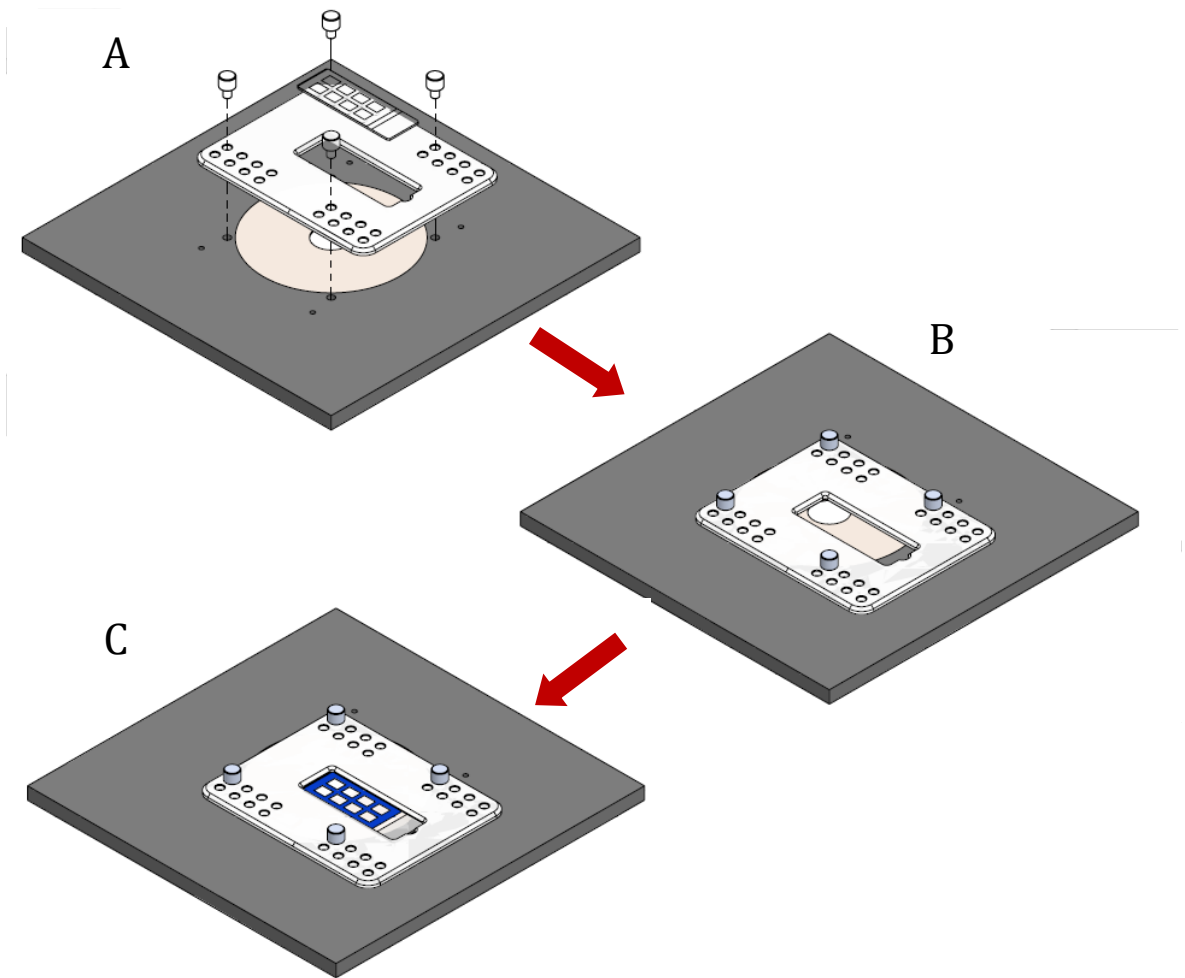


Figure 4.8. Custom built slide position locator. The microscopy slide is divided into eight areas, with 2D monolayers located in each area. Selecting an area, which corresponds to the pins on the slide position locator, the position locator was mounted to the microscopy stage. The slide was then inserted into the holder, with the selected area positioned above the objective. This allowed the location of cells that were selected for repeated imaging to be noted, making it possible to locate them at a later date.

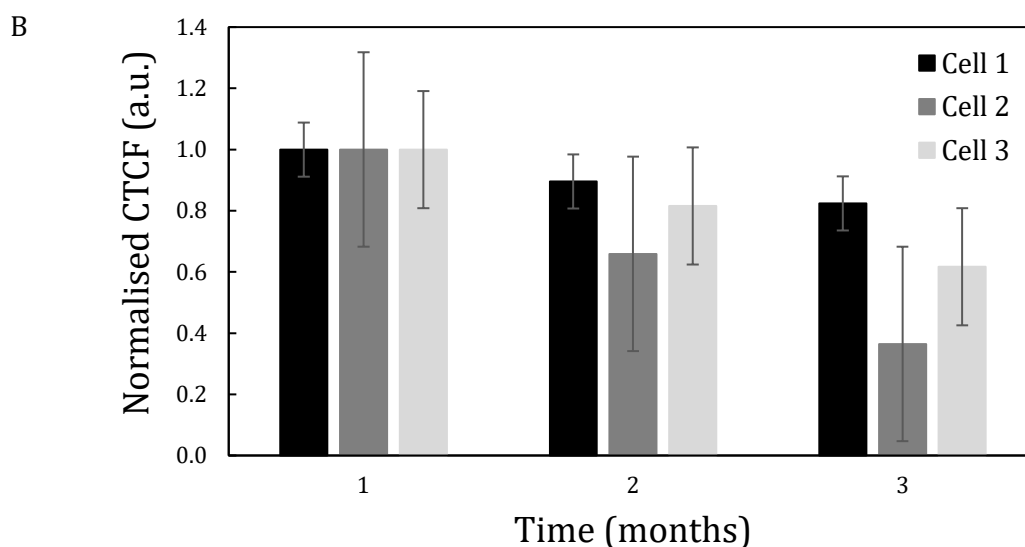
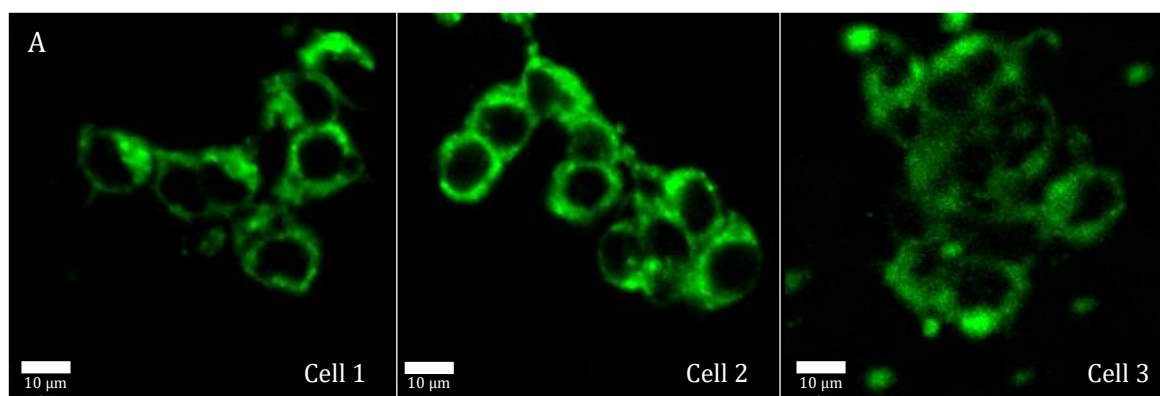


Figure 4.9. Fluorescence intensity measurements of 2D monolayers of HepG2 cells. (A) These cells were selected, and imaged weekly over three months. (B) The CTCF was calculated for each cell, with the average, normalised, month CTCF plotted. The plot shows a decrease of fluorescence intensity for each cell, over time.

4.2.4. Direct Imaging Method Validation

In previous work undertaken by Tutty *et al.* [143] and indirect imaging method was used to detect NBMs in 3D hepatic spheroids. The indirect imaging method required the NBM to be fluorescently labelled. Fluorescent labelling involves attaching another fluorescent molecule to the NBM to aid with detection of the NBM. The NBM was fluorescently labelled using a primary antibody, and then appropriate secondary antibody, i.e., anti-PEG primary antibody (ab170969), and Alexa Fluor-488 goat anti-mouse secondary antibody. The excitation/emission spectra for Alexa Fluor-488 and LipImage are shown in Figure 4.10, where it is observed that Alexa Fluor-488 is excited and emits in the visible range of the EM spectrum, and LipImage is excited and emits in the near infra red (near-IR) region of the EM spectrum. Alexa Fluor-488 was then

excited using a 488 nm laser, with peak emission at 525 nm, seen in Figure 4.11 [144]. This protocol is similar and comparable to that used for poly(ethyl-butyl cyanoacrylate) nanoparticle (NP) (PACA). However, LipImage™815 is a near-IR dye, which has an optical window that has low signal to noise, low autofluorescence and causes minimal damage to surrounding tissues, and can be used for deep tissue imaging [145]. In this work, direct imaging method using confocal microscopy was used to localise NBMs within the core of a 3D hepatic cell culture model, shown in Figure 4.11. Using excitation and emission wavelengths of $\lambda_{ex}/\lambda_{em}$ 740/830 nm [146] for LipImage™815, a direct imaging method can be achieved, which reduces the complexity of the sample preparation protocol, and takes advantage of the benefits of using a near-IR dye, with a view for use of the method in assessing the toxicology of NMBs, an application which is beyond the scope of this work.

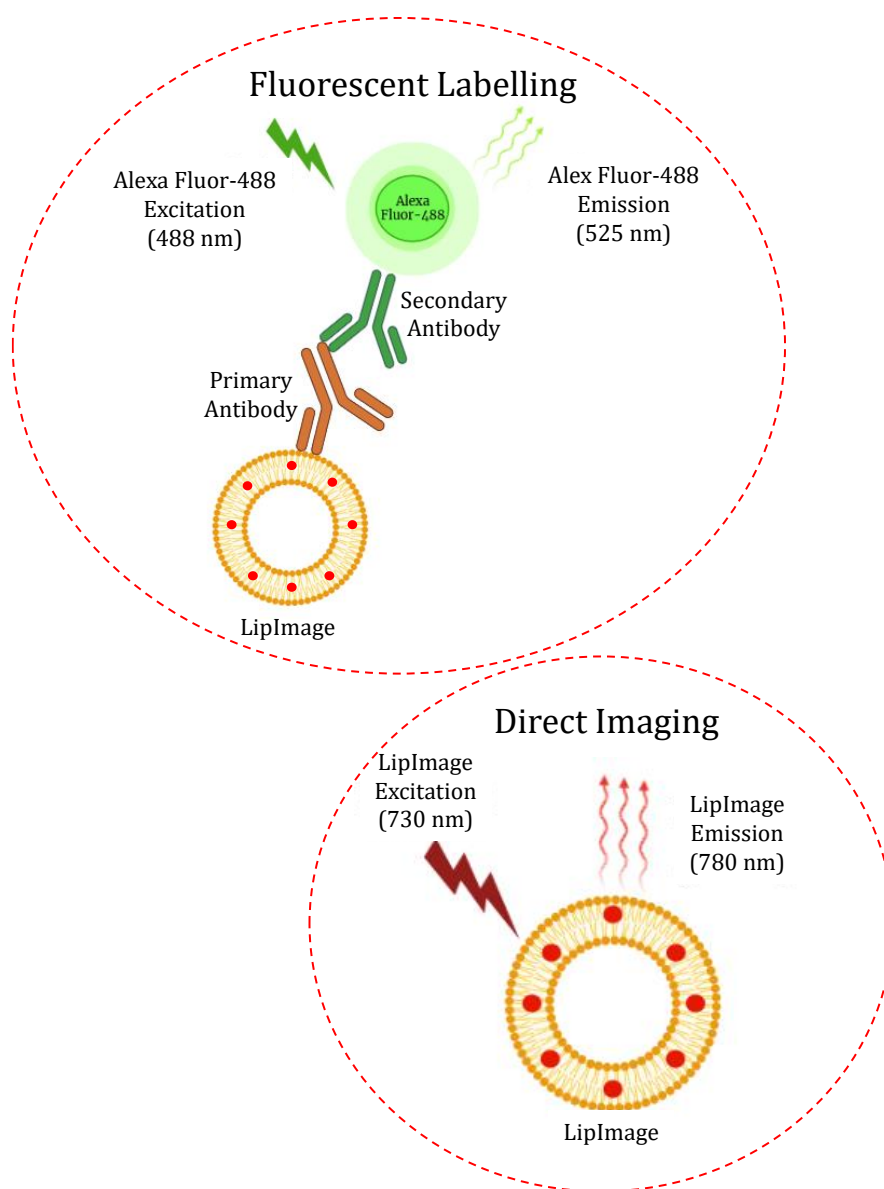


Figure 4.10. Fluorescent Labelling vs Direct Imaging.

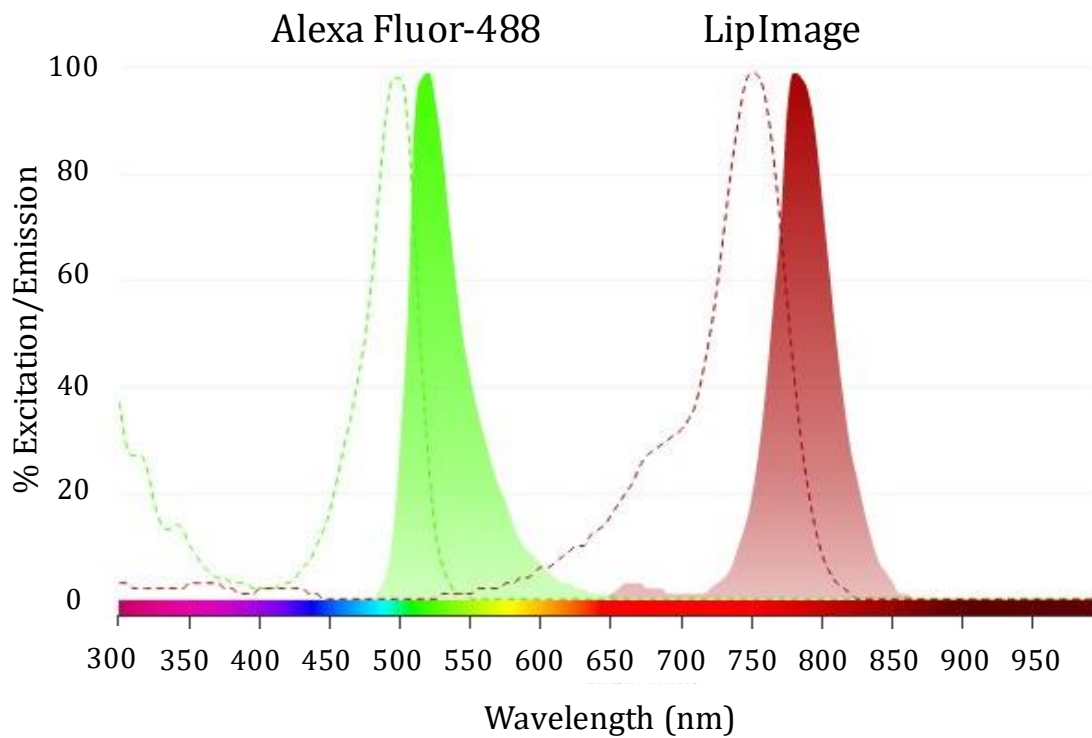


Figure 4.11. Excitation and emission spectra for Alexa Fluor-488, excited in the visible range of the spectrum and LipImage, excited in the Near-IR range of the spectrum.

Figure 4.12 illustrates a control image of a monolayer of HepG2 cells stained with Hoechst (nuclei), Rhodamine phalloidin (actin), and Alexa Fluor-488 goat anti-mouse Ab (NBMs) and imaged using the direct imaging method, describe in § 4.1.9.

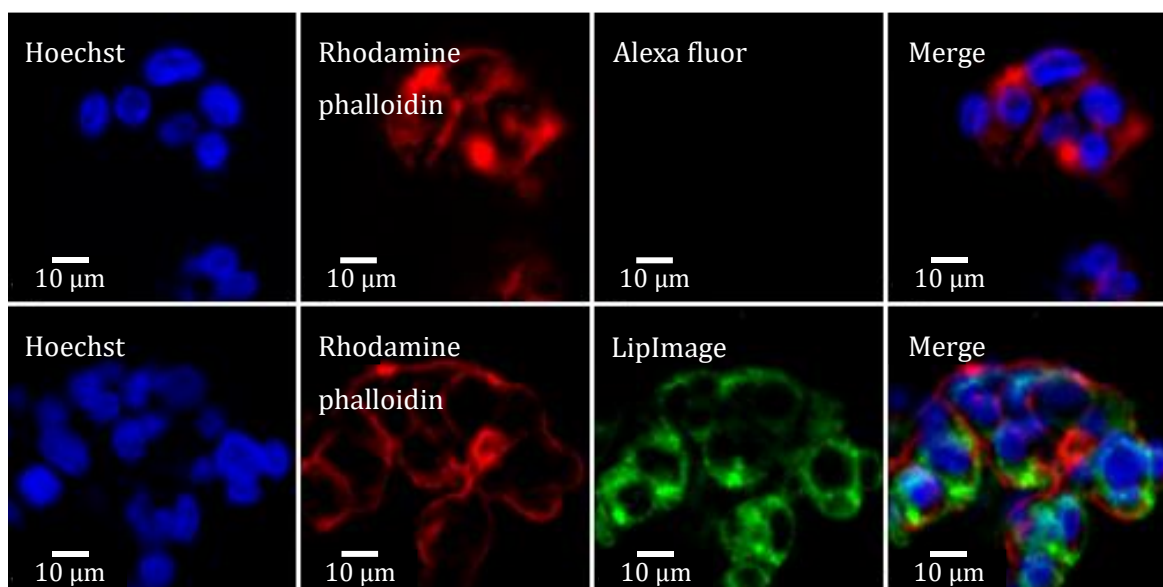


Figure 4.12. Validation of direct imaging. Control 2D monolayers were stained with (A) Hoechst (nucleus – blue, 1:1000), (B) Rhodamine phalloidin (actin – red, 1:40), and (C) Alexa Fluor-488 goat anti-mouse (particle – green, 1:500). In this panel, the Alexa Fluor-488 is excited with a 730 nm laser, and a 750 nm long pass emission filter is used. These are the condition used to image LipImage. No fluorescence from Alexa Fluor-488 is detected under these conditions. (D) shows a merged image.

4.2.5. Confocal Images

Confocal intensity images were obtained as described in § 4.1.9. These images were imported into ImageJ, where they were de-speckled and the background was removed, before being stitched together, using a bespoke Python programme (see Appendix A). A pseudo colour is applied to each image in ImageJ, and the images are then merged. From these images, the location of the NBM can be visualised, as observed in Figures 4.13 and 4.14. However, only qualitative information can be obtained from these images, as the images have been adjusted for visualisation. Quantitative analysis is carried out on the raw intensity images, shown in Figure 4.15.

During image acquisition, the area imaged was limited to $80 \times 80 \mu\text{m}^2$, therefore, there needed to be some overlapping between images, to ensure that the entire focal plane of the spheroid was captured. This introduced artefacts in the form of photobleaching, into the images, which appear as dark lines at the border of the smaller images that make up the larger image. These artefacts are most obvious in the raw intensity image for LipImage, shown in Figure 4.15. The confocal images show that the spheroids are

not wholly circular or appear to have distinct portions within the spheroid core where stained cells cannot be visualised. Mechanical damage can occur to the spheroids when they are being mounted before being imaged, which can present as misshaped spheroids, or give the appearance of empty space. Misalignment of images can also occur during image acquisition, which is evident in some images and is noted in Figure 4.13 (Rhodamine phalloidin at 48 h). This does not affect the analysis of the NBM.

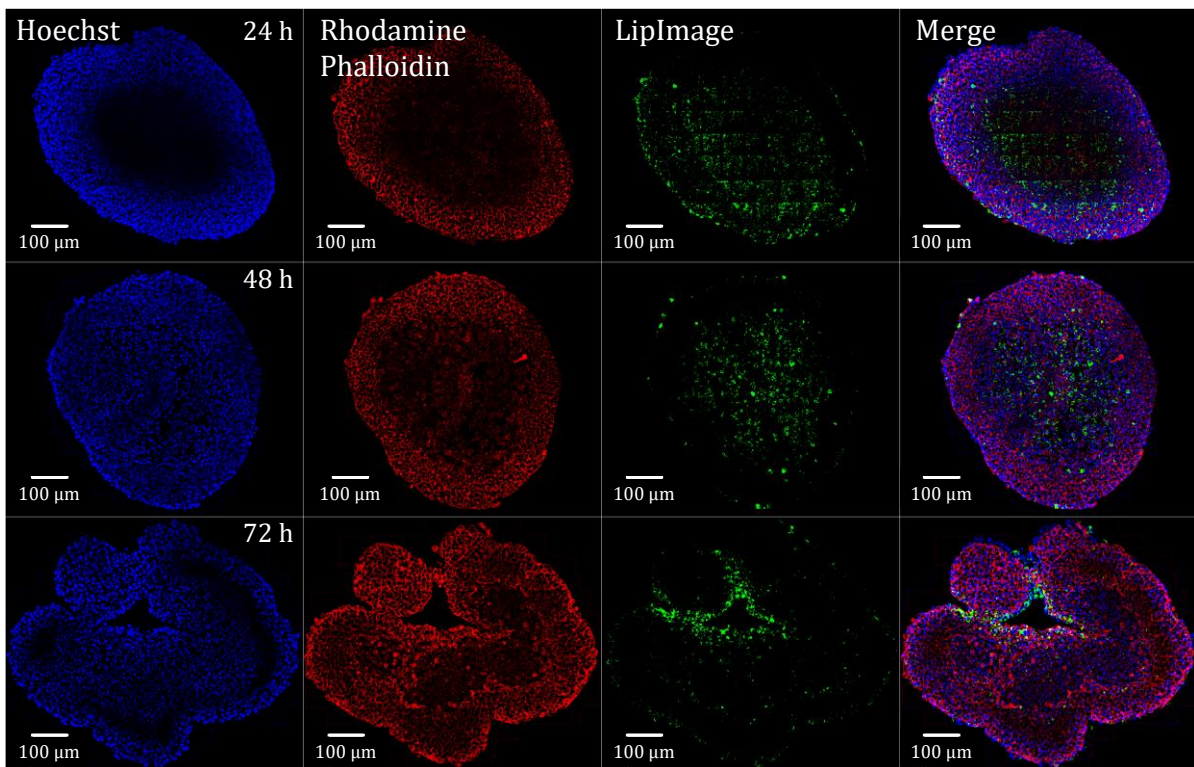


Figure 4.13. Colour confocal images stained with Hoechst (nuclei – blue, 1:1000), Rhodamine phalloidin (actin – red, 1:40), and treated with 200 µg/ml LipImage (green), and merged to show the localisation of LipImage through the spheroid, at 24 h, 48 h, and 72 h.

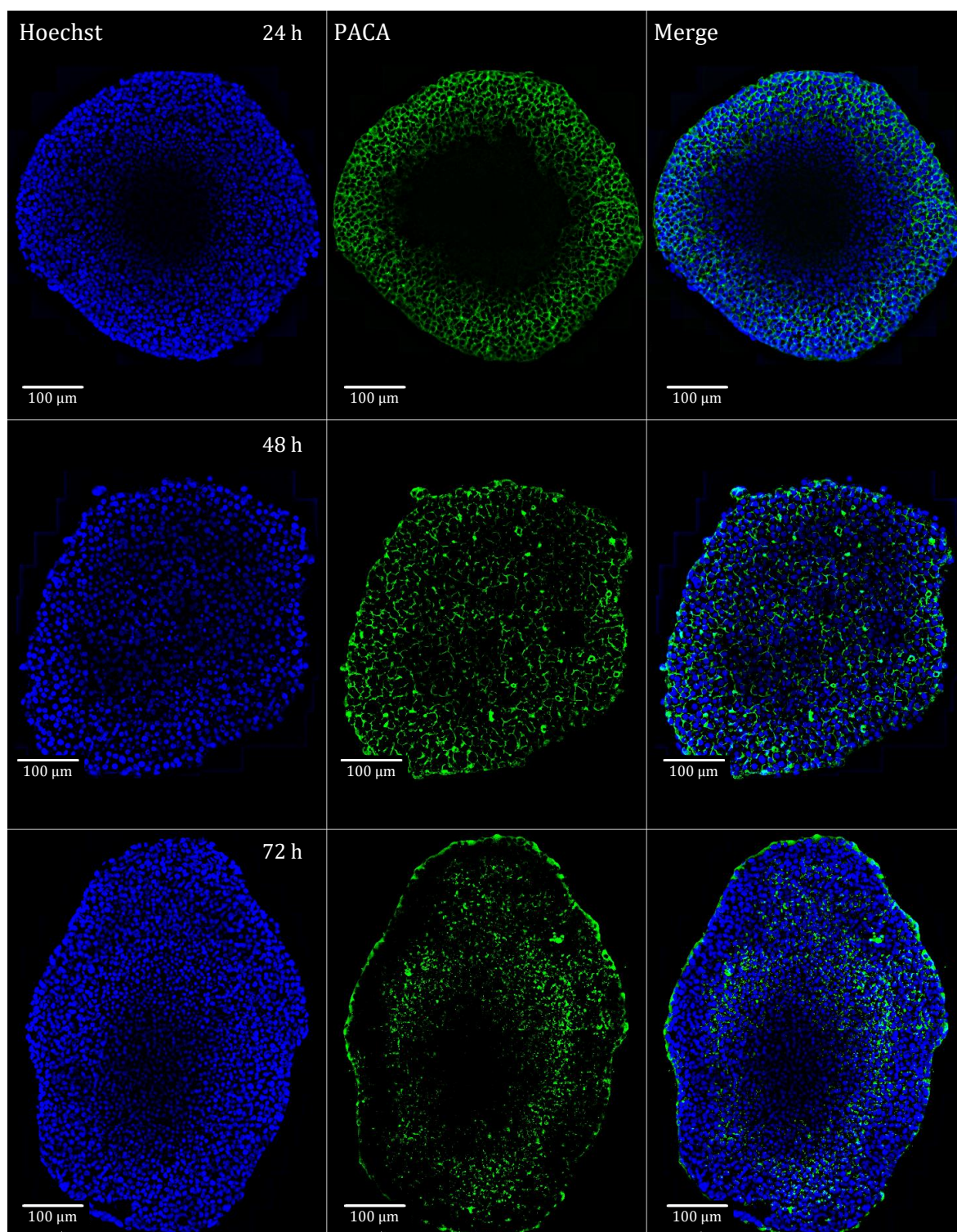


Figure 4.14. Colour confocal images stained with Hoechst (nuclei – blue, 1:1000), and treated with 30 µg/ml of PACA (green) and merged to show the localisation of PACA through the spheroids, at 24 h, 48 h, and 72 h.

4.2.6. Distribution of NBMs in HepG2 Spheroids

To investigate the effect of treatment time on 3D spheroids, fluorescent intensity of the spheroids treated with NBMs was measured. The colour confocal images from Figures

4.13 and 4.14 demonstrate that both NBMs appear to fully penetrate the core, but at different rates. This was previously seen by Tutty *et al.* using 3D reconstructions of the spheroids [143]. Here, the confocal intensity images were acquired, and as described in § 4.1.9, were stitched together, in order to carry out analysis on the focal plane imaged. The raw intensity images for both NBMs are reported in Figure 4.3. As previously mentioned, overlapping during image acquisition was necessary, and can be clearly seen in the intensity images presented. Photobleaching of the area that is imaged, up to three times, shown in Figure 4.5, can be very clearly seen in the stitched intensity images, showing up as a dark border between images. This did not appear to affect PACA as much as it affected LipImage.

LipImage is observed in the spheroid core after 24 h, whereas PACA could only be observed in the spheroid core after 48 h exposure, observed in Figure 4.15. By measuring the integrated fluorescence intensity of the whole image, it can be seen that neither NBM is suitable for long incubation times, of up to 72 h or beyond. It is hypothesised that a degradation in the liposome results in the dye coming into contact with water, consequently quenching the IR780. Degradation of the polymer shell may also be the cause of the decrease in intensity seen for PACA. This phenomenon can also be observed in Figure 4.16, where the integrated fluorescence intensity of spheroids was measured following treatment with NBMs to evaluate the overall fluorescence intensity of the NBMs in each spheroid. This was achieved by marking the circumference of the spheroid, and measuring the integrated fluorescence intensity. Both NBMs show a significant decrease in intensity suggesting a degradation in the NBMs over longer incubation times, when the sample is unfixed. This decrease in intensity different to the decrease in intensity seen previously in 2D monolayers from § 4.2.2. In that case, the 2D monolayers were treated with LipImage for 24 h and subsequently fixed. The decrease in intensity seen was due to repeated fluorescence imaging, i.e., photobleaching.

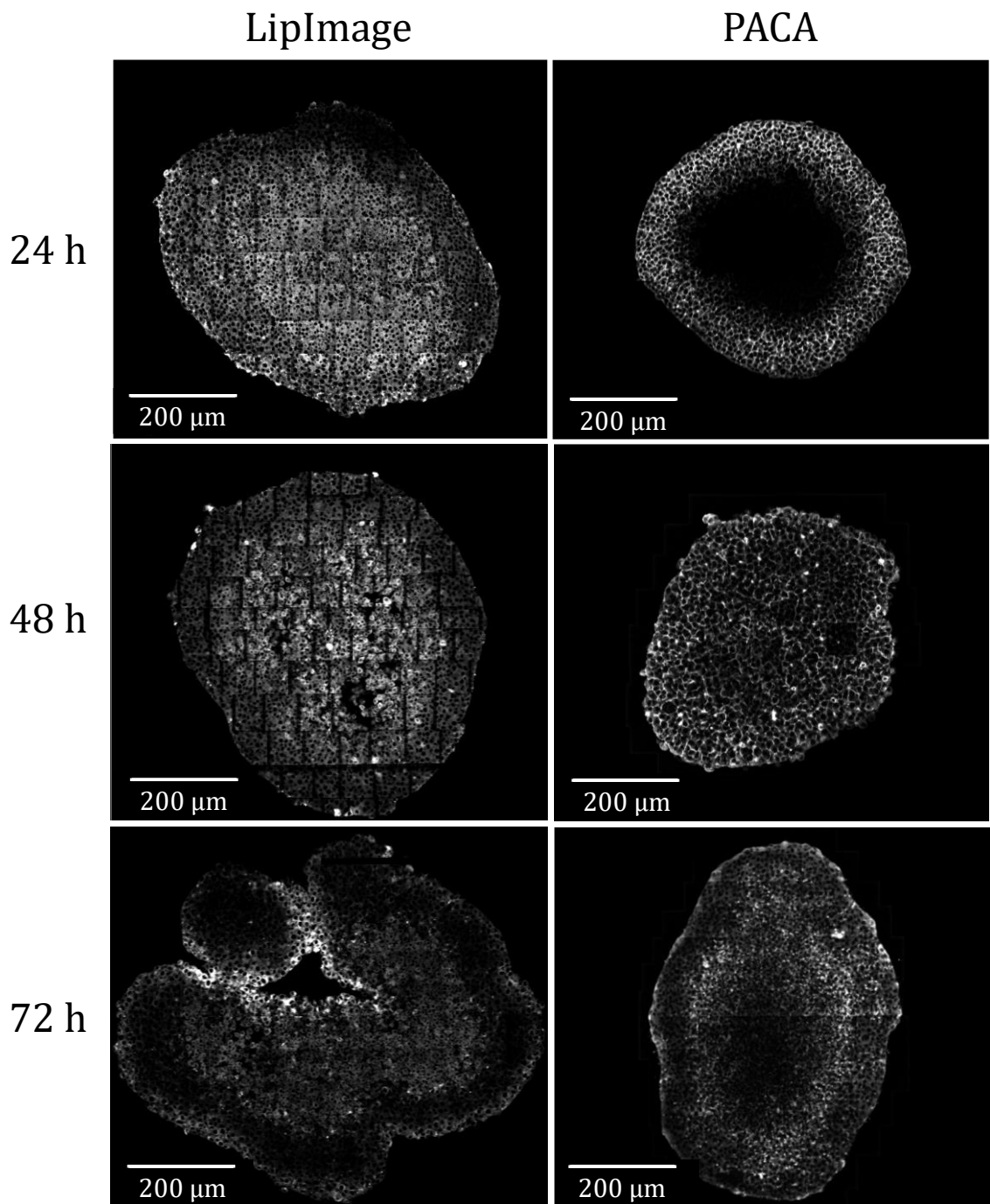


Figure 4.15. Stitched, normalised intensity images of LipImage and PACA treated spheroids. HepG2 spheroids treated with 200 µg/ml of LipImage, and 30 µg/ml of PACA for: 24 h, 48 h, and 72 h. Images acquired were 80 × 80 µm² that were normalised and stitched together for whole focal plane spheroid image analysis. These were then used for all quantitative analysis carried out throughout this body of work. Here images are enhanced.

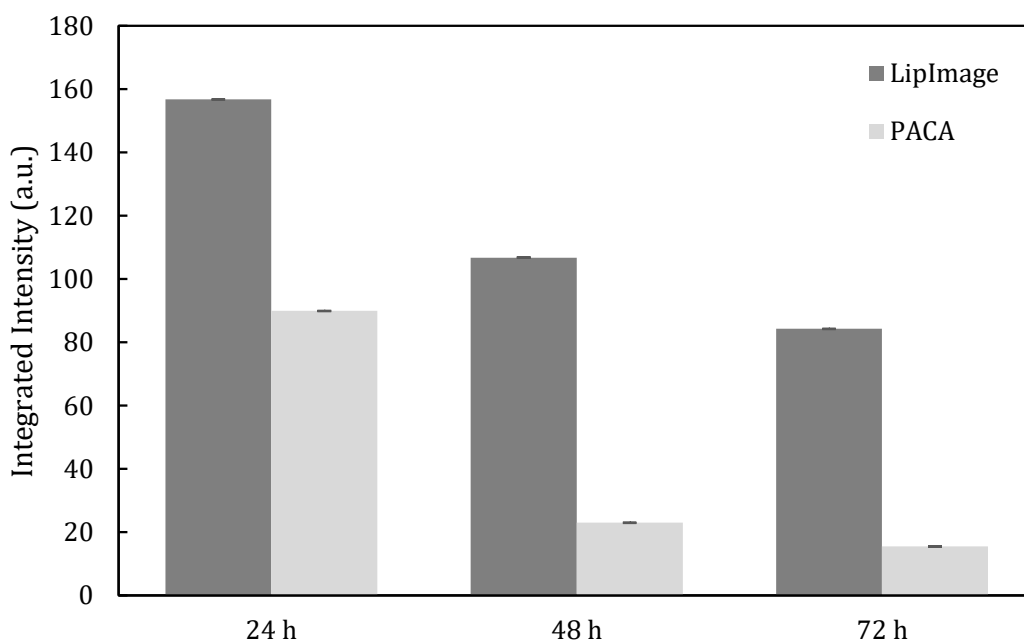


Figure 4.16. Fluorescence intensity of whole spheroid. The integrated fluorescence intensity of the spheroid was measured. This shows a decrease in the fluorescence intensity for both NBMs over treatment time.

Line plots were explored, and are presented in Figure 4.15, to examine the distribution of the NBMs from the periphery, through the core, and to determine if the distance from the periphery of the spheroid had an influence on the distribution pattern of the NBM. Using the raw intensity images from Figure 4.15, a 1-pixel thick ($0.267\ \mu\text{m}$) line was drawn from the periphery-core-periphery, at 45° , 90° , 135° , and 180° , with all lines intersecting at the core. The fluorescence intensity is measured along these lines, and plotted. The line plots show that more LipImage appears to penetrate to the core when compared to PACA for all time points. This is particularly evident at 24 h, where no PACA appears to penetrate to the core, but is instead concentrated at the periphery, likely due to its large size. In Figure 4.17 (1A) it can be observed that LipImage showed a homogenous distribution from periphery to the core, in all directions, after 24 h. At 48 h and 72 h, LipImage appears to have a slightly less homogenous distribution, with a peak in the intensity appearing at the core. PACA, on the other hand, shows no NBM at the core at 24 h, shown in Figure 4.17 (2A) but has high intensity at the periphery. After 48 h, PACA can be observed at the core, with still slightly higher intensity observed at the periphery. However, by 72 h PACA has penetrated the core and a more homogenous distribution of the NBMs can be seen. All plots show a decrease in intensity at 72 h, confirming observations made in Figure 4.16.

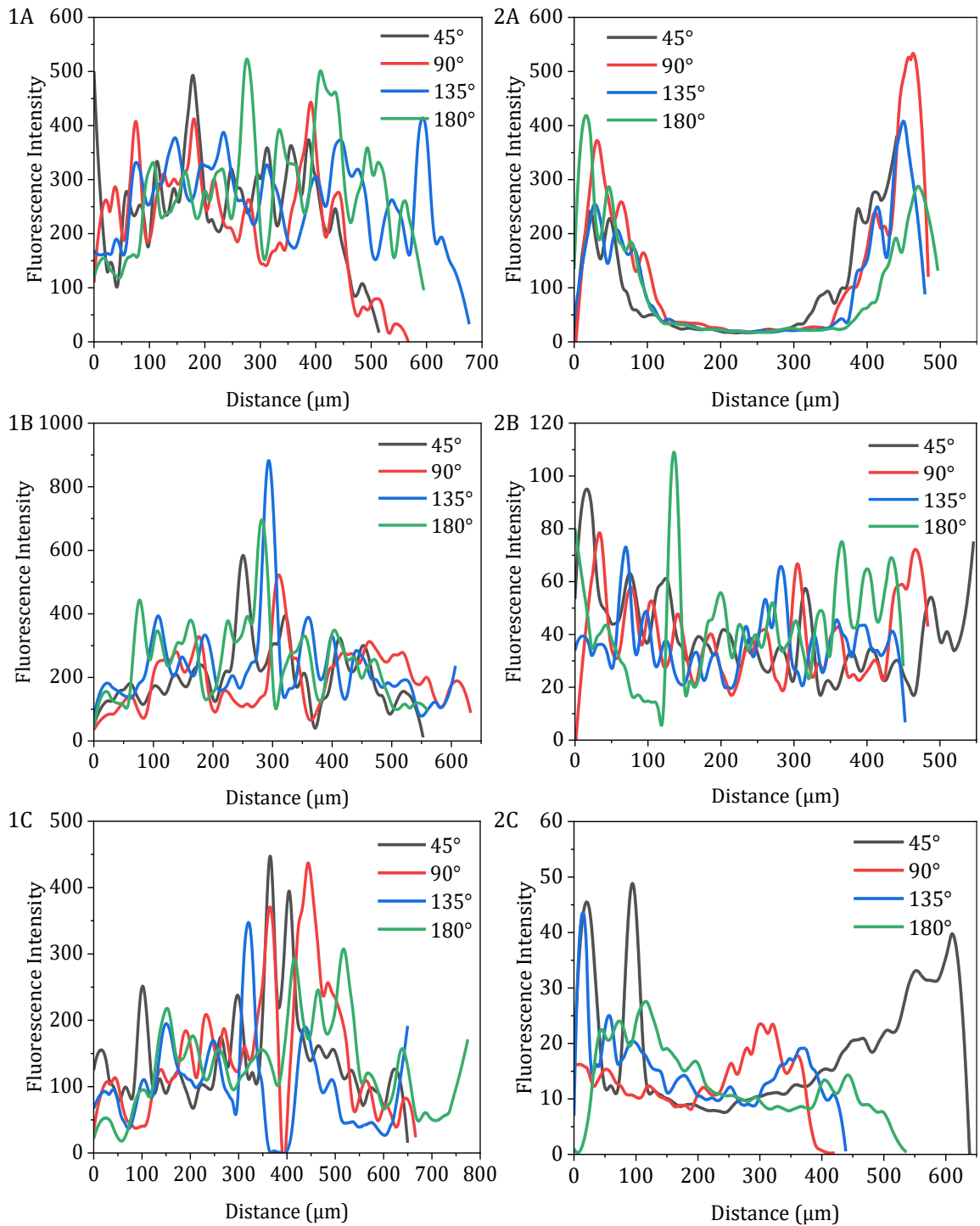


Figure 4.17. A line plot from periphery through the core of the spheroid, showing the actual intensity and distribution of NBMs through a spheroid. (1) LipImage and (2) PACA. In both cases, (A) refers to 24 h, (B) to 48 h, and (C) to 72 h treatment times. A 1-pixel thick ($0.267 \mu\text{m}$) line was drawn from periphery-core-periphery at 45° , 90° , 135° , and 180° , with all lines intersecting at the core. As the spheroids were not perfectly circular, the length of each line varied, but the overall profile of each plot, in each spheroid, was similar.

Translocation and penetration of the NBMs into the core of the spheroid was assessed by plotting colour maps of the normalised integrated fluorescence intensity. Using a bespoke MATLAB script, CCD binning was used to produce a 100 px × 100 px (26.7 × 26.7 μm²) area, about twice the size of an average cell, where the integrated fluorescence intensity was measured and outputted as a text file. It was previously seen that fluorescence intensity at the periphery and at the core differs for both NBMs, at different time points, see Figure 4.17. The translocation of both NBMs and how they penetrate the core of the spheroid, and the changes that are seen over time is shown in Figure 4.18. At 24 h, LipImage has fully penetrated to the core of the spheroid, when compared to PACA, which is fully concentrated at the periphery of the spheroid. While this was seen in Figure 4.17 (1A), the colour maps present a better idea of how the NBM is distributed. Figure 4.17 (1A) shows that there is a homogeneous distribution of the NBM recorded from the periphery through to the core. The colour maps in Figure 4.18 show that the distribution is not as homogenous as initially assumed, with a higher intensity of the NBM noted towards the core of the spheroid noted for LipImage at 24 h. After 48 h, LipImage shows a more homogenous distribution, with few high intensity regions seen at the core. Conversely, PACA has almost fully penetrated the spheroid, becoming more homogenous by 72 h. At 72 h, degradation in LipImage can be seen, with little NBM seen at the periphery of the spheroid. However, where the NBM is concentrated is a periphery, albeit it near the core of the spheroid, as this spheroid appears to have a hole at its core. These colour maps show that LipImage penetrates further into the spheroid, and faster than PACA, due in part to its small size. However, PACA appears to be a more biopersistent NBM with consistent translocation seen up to 72 h, whereas LipImage is only consistently showing up to 48 h, due in part to the liposome which encapsulates the IR780 dye. This liposome degrades with increased incubation time, when the sample is unfixed and in turn releases the dye inside the liposome, exposing it to water, which quenches the dye making LipImage unsuitable for long exposure treatment.

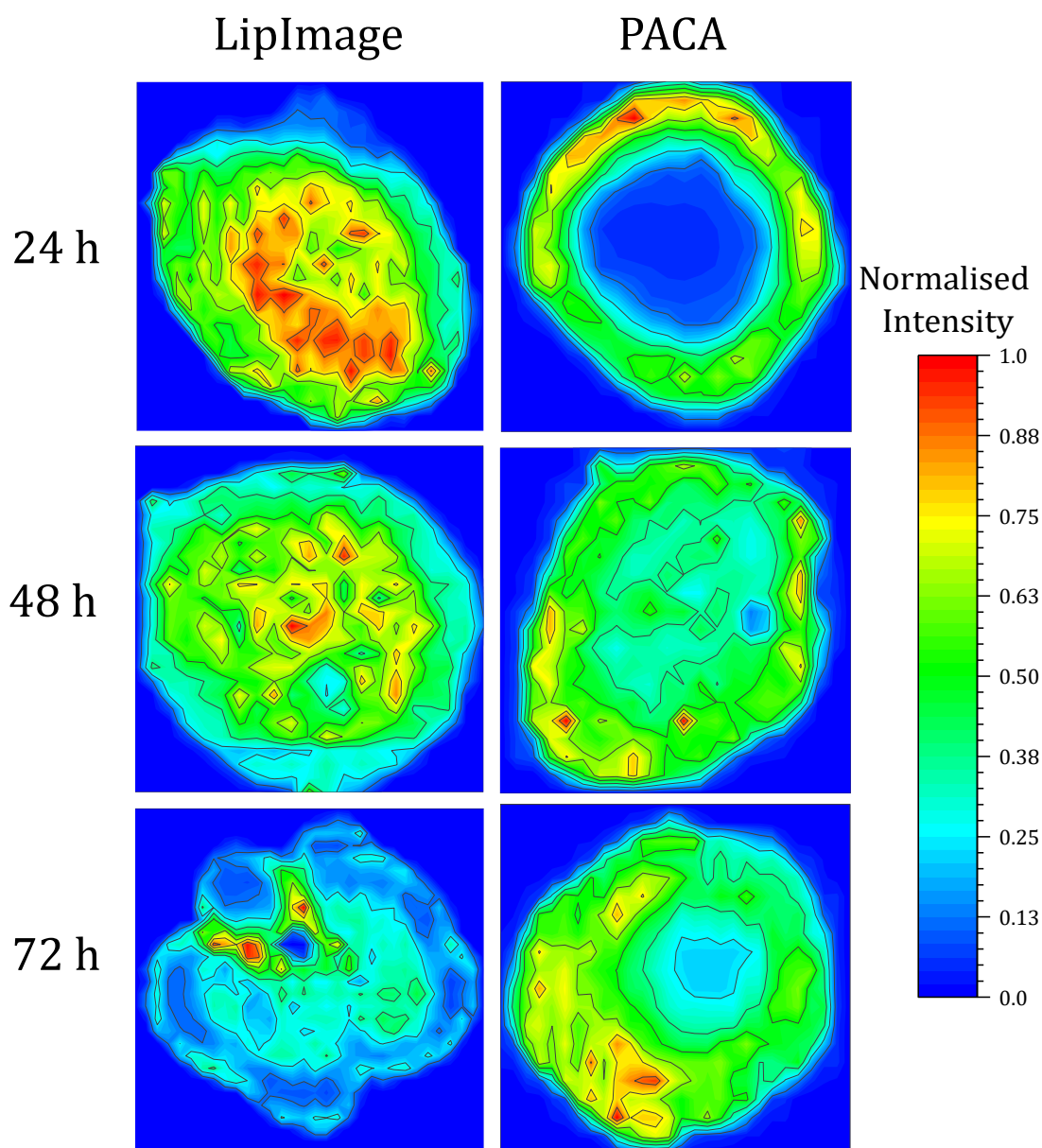


Figure 4.18. Colour maps representing normalised NBM translocation and penetration for LipImage (200 $\mu\text{g/ml}$) and PACA (30 $\mu\text{g/ml}$). Integrated intensity measurements of $26.7 \times 26.7 \mu\text{m}^2$ (100 x 100 pixel) area were made and plotted as colour maps. These maps indicate the translocation and penetration of NBMs over time, showing that with an increase in treatment time, LipImage appears homogenous at 48 h, before decreasing at 72 h, while PACA requires 48 h to penetrate to the core of the spheroid, due to its large size, and again, decreasing at 72 h.

4.2.7. Fluorescence Lifetime Imaging Microscopy

Fluorescence Lifetime Imaging Microscopy (FLIM) was carried out at the same time as confocal microscopy. Normalised decay curves were plotted, and are shown in Figure 4.19. these graphs were then fitted using Equation 4.1 and Equation 4.2. From this, the data in Table 4.4 was extracted, and using Equation 4.3 and Equation 4.4 the amplitude

weighted average lifetime was calculated for both NBMs at different treatment time points.

Table 4.4. Table of Data obtained from fitted graphs. The average lifetimes for both NBMs were calculated from normalised, fitted graphs, and using Equations 4.3 and 4.4.

NBM	Time (h)	A_1	τ_1 (ns)	A_2	τ_2 (ns)	τ_{avg} (ns)
LipImage (200 $\mu\text{g}/\text{ml}$)	24	-	-	1.1	1.1	1.1 ± 0.1
	48	-	-	1.0	1.0	0.9 ± 0.1
	72	-	-	1.1	1.1	1.1 ± 0.1
PACA (30 $\mu\text{g}/\text{ml}$)	24	0.9	2.4	0.2	6.2	3.7 ± 0.2
	48	0.3	1.2	0.7	3.5	3.2 ± 0.3
	72	0.3	1.4	0.7	3.9	3.5 ± 0.1

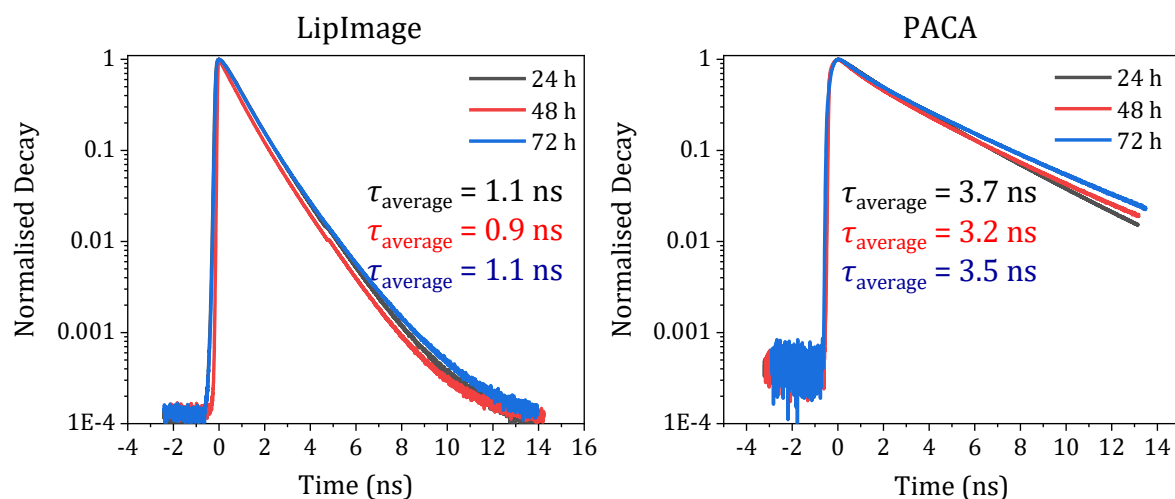


Figure 4.19. Fluorescence Lifetime Decay Curves. Spheroids were treated with 200 $\mu\text{g}/\text{ml}$ of LipImage and 30 $\mu\text{g}/\text{ml}$ of PACA for 24 h, 48 h, and 72 h. Using a non-linear, one- or two-exponential decay fitted curve for LipImage, and a two-exponential decay curve for PACA, the amplitude and time were extracted. Using equations 4.3 and 4.4, the average lifetime for both NBMs was calculated. The graphs show that LipImage has a shorter lifetime compared to PACA.

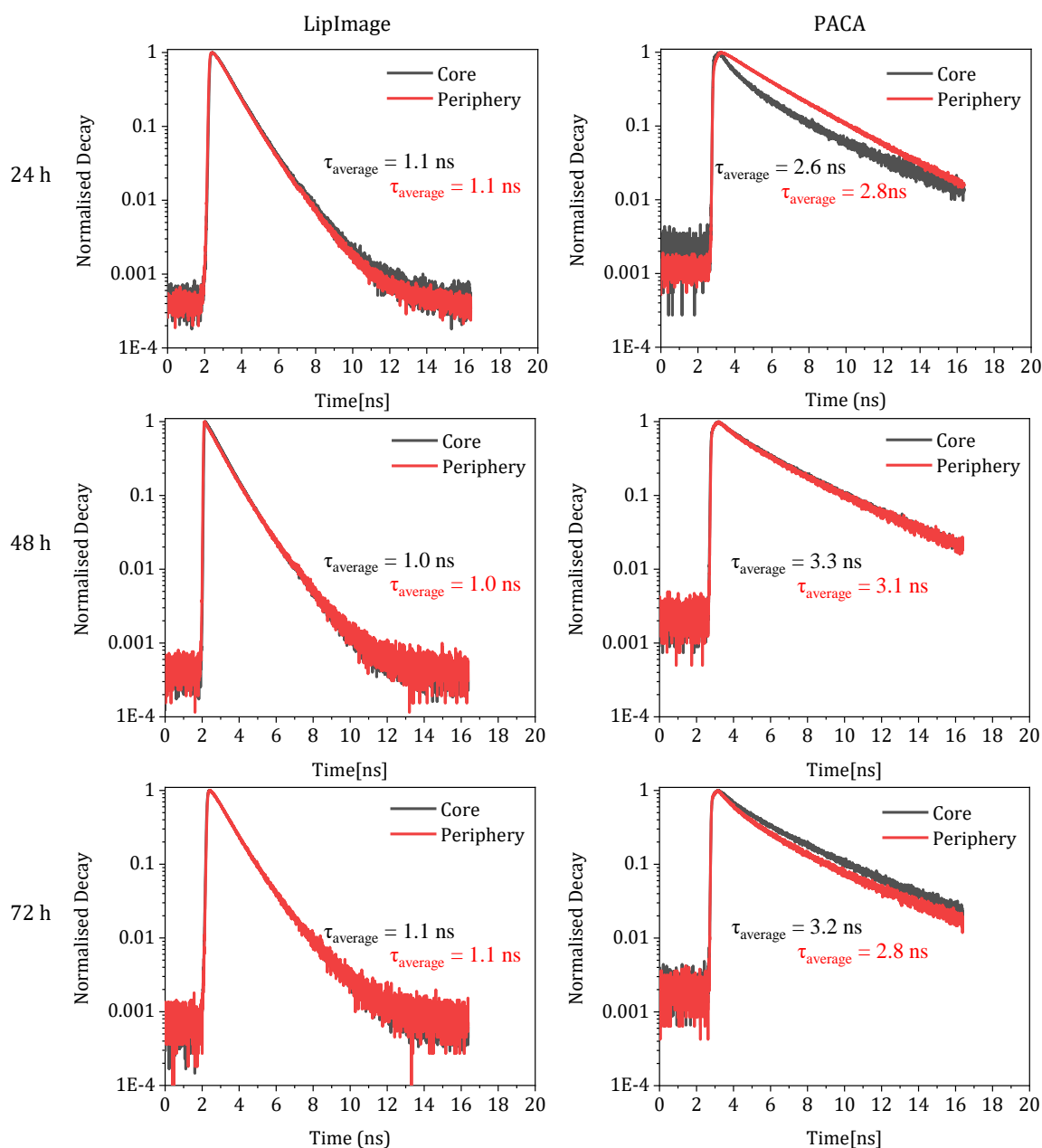


Figure 4.20. Fluorescence lifetime decay curves of LipImage (200 $\mu\text{g/ml}$) and PACA (30 $\mu\text{g/ml}$) at 24 h, 48 h, and 72 h treatment time points. In each instance an image was selected from the periphery of the spheroid, and from close to the core of the spheroid to determine if location within the spheroid affected the lifetime of the NBM. From the decay curves, there does not appear to be any significant difference in where the NBM is located, except in the case of PACA, 24 h, where from previous investigations, little to no PACA is detected.

The normalised decay curves in Figure 4.19 show the lifetimes for LipImage (1.02 ns \pm 0.07 ns) and PACA (3.46 ns \pm 0.27 ns), which are very different, as would be expected from the different emitters. The only variable between the decay curve is the incubation time, which should not affect the lifetime. However, from Figure 4.18 it has

already been seen that there is not a homogenous distribution of the NBMs over the various time points. Therefore, it may be of use to measure the lifetime at the periphery and at the core, as this will likely explain the large variation in the lifetimes for these images. With the exception of LipImage 48h, where whether at the periphery or the core the lifetime was unchanged, or PACA 24 h, where at the core the lifetime was less than at the periphery, the lifetime behaved as expected. As discussed in Chapter 2, spheroids tend to be hypoxic at their core, and the oxygen gradient through the spheroid may contribute to the changes in lifetimes, as molecular oxygen is known to be an effective quencher of fluorescence [160,161].

4.3.Conclusion

A novel direct imaging method, using confocal microscopy, was used to investigate the translocation and penetration of NBMs in a 3D *in vitro* model. This technique allowed for the direct imaging of NBMs present in the spheroid, and removed the requirement to fluorescently label the NBMs, making the preparation of the spheroids easier and less time consuming. Using the direct imaging technique, it was seen that LipImage can fully penetrate to the core of the spheroid in 24 h, while PACA requires 48 h, with little change to the distribution seen after this time point. However, at 72 h and beyond, there is a significant change in the distribution of LipImage. It was seen that while the NBM can still be observed at the core of the spheroid, there is a substantial decrease seen at the periphery of the spheroids. Long treatment times result in the degradation of the liposome encapsulating the near-IR dye, which results in a bursting of the liposome, releasing the dye into the spheroid, where it is quenched. Examining the lifetimes of the NBMs showed that at the periphery of the spheroid, the NBMs are quenched, when compared to the hypoxic core of the spheroid, as might be expected.

Most studies will assess different variables of the experimental parameters, e.g., using different time points to evaluate how time affects the translocation and penetration of an NBM, as was discussed in this chapter. But how will the NBM be affected if these parameters are changed? Will increasing the concentration of the NBM require less time for the NBM to penetrate to the core, or will the NBM agglomerate at the periphery of the spheroid? Or will decreasing the concentration, but increasing time allow for a more homogenous distribution, or will the increased time still result in a degradation of the liposome? Chapter 5 will explore these questions by using a lower, and a higher concentration for both NBMs, and use the same time points that have already been used

here. In Chapter 5, a simple diffusion model will be used to compare the diffusion for both NBMs.

Chapter 5 Assessing the Effects of Concentration on Nanobiomaterial (NBM) Interactions and Trafficking in Three-Dimensional Hepatic Spheroids

This chapter expands on the work that was carried out in Chapter 4, where a novel, direct imaging method was developed, validated, and implemented to localise NBMs within the core of a 3D hepatic cell culture. Using confocal microscopy, a highly sensitive, non-destructive imaging technique, and Fluorescence Lifetime Imaging Microscopy (FLIM), which measures the decay rate of photon emission, information on the translocation, penetration and distribution of NBMs in hepatic 3D spheroids was investigated. In Chapter 4, one concentration was selected for both NBMs. For this study, a lower and a higher concentration for each NBM was also investigated. For LipImage and PACA, 100 µg/ml and 500 µg/ml, and 10 µg/ml and 50 µg/ml were selected respectively, with the treatment times of 24 h, 48 h, and 72 h remaining the same.

Chapter 4 demonstrated that 72 h was too long a treatment time for both LipImage and PACA at 200 µg/ml and 30 µg/ml respectively, but for lower concentrations, this may be an acceptable treatment time. It was also seen that for 30 µg/ml, PACA required at least 48 h to penetrate to the core of the spheroid. This work will investigate if increasing the concentration to 50 µg/ml allows penetration to the core to occur at 24 h, and if a lower concentration of 100 µg/ml for LipImage will allow a homogenous distribution and penetration to the core.

Using the Stokes Einstein Equation, the diffusion constant was calculated for both NBMs at both room temperature (RT), 20 °C, and treatment temperature, 37 °C. The root mean square displacement was then calculated for each NBM, and a comparison was made between the calculated diffusion, and the experimental diffusion of the NBMs within the spheroids.

5.1. Materials and Methods

The materials and methods for this chapter are the same as those described in § 4.1. The spheroids were exposed to LipImage and PACA, as described in Table 5.1. The rationale behind these concentrations and exposure times was to allow adequate time for NMBs to penetrate to the core of the spheroid, and evaluate if higher concentrations had an effect on their distribution.

Table 5.1. NMBs used in this work. Spheroids were exposed to each NBM for up to 72 h, at different concentrations.

NBM	Treatment Concentration ($\mu\text{g/ml}$)	Exposure Time (h)
LipImage	100, 500	24, 48, 72
PACA	10, 50	24, 48, 72

5.2. Results and Discussion

5.2.1. Bright-field microscopy

Bright-field microscopy was carried out using an Olympus IX 71 inverted microscope, and an Olympus PLN 4X/0.1 air/dry objective. Figure 5.1 shows a selection of HepG2 spheroids. These spheroids were formed from a cell seeding concentration of 1,000 cells per 1 μL culture medium, and cultured in CellStar[®] cell repellent plates for 7 days. At this time point, spheroids showed well defined edges, and good shape. Spheroids were then selected, and treated with NMBs, as per Table 5.1, for up to 72 h. The representative images seen in Figure 5.1 were taken post treatment.

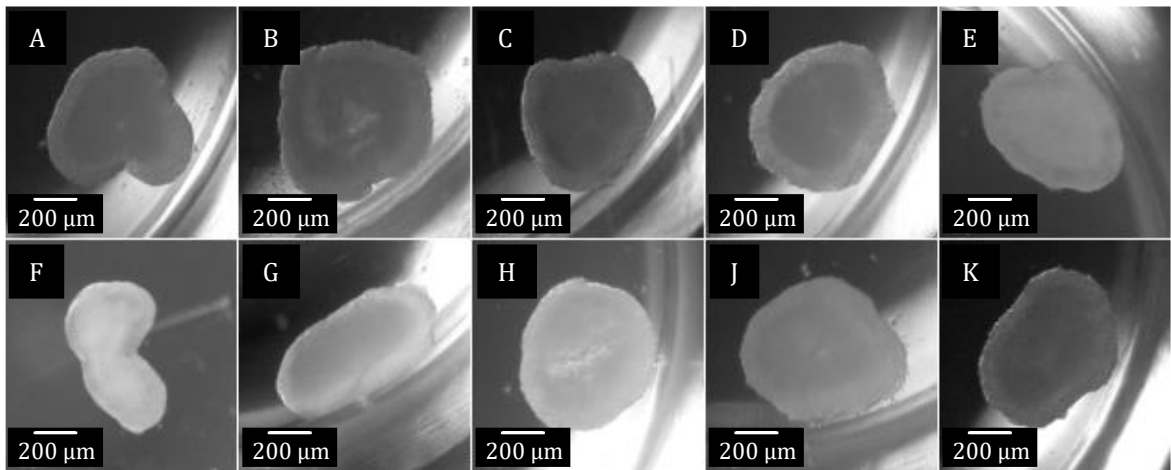


Figure 5.1. Representative bright-field images of HepG2 spheroids. Spheroids were formed from a cell seeding concentration of 1,000 cells per 100 μL culture medium and cultured in CellStar[®] cell repellent plates for 7 days. At this time point, spheroids showed well defined edges, and good shape, with the exception of (F) and (G). (F) was not selected for confocal imaging. Spheroids were then treated with NMBs for up to 72 h before these images were acquired. These images were acquired post treatment.

5.2.2. Confocal Microscopy

Confocal intensity images were obtained as described in § 4.1.9. These images were imported into ImageJ [151], where they were de-speckled and the background noise was removed. Using a bespoke Python program, these images were then normalised and stitched together. Stitched images were once again imported into ImageJ and a pseudo colour was applied to each image. These images were then merged together, and enhanced, allowing the NMBs to be visualised, as seen in Figures 5.2, and 5.3 for LipImage, and Figures 5.4, and 5.5 for PACA.

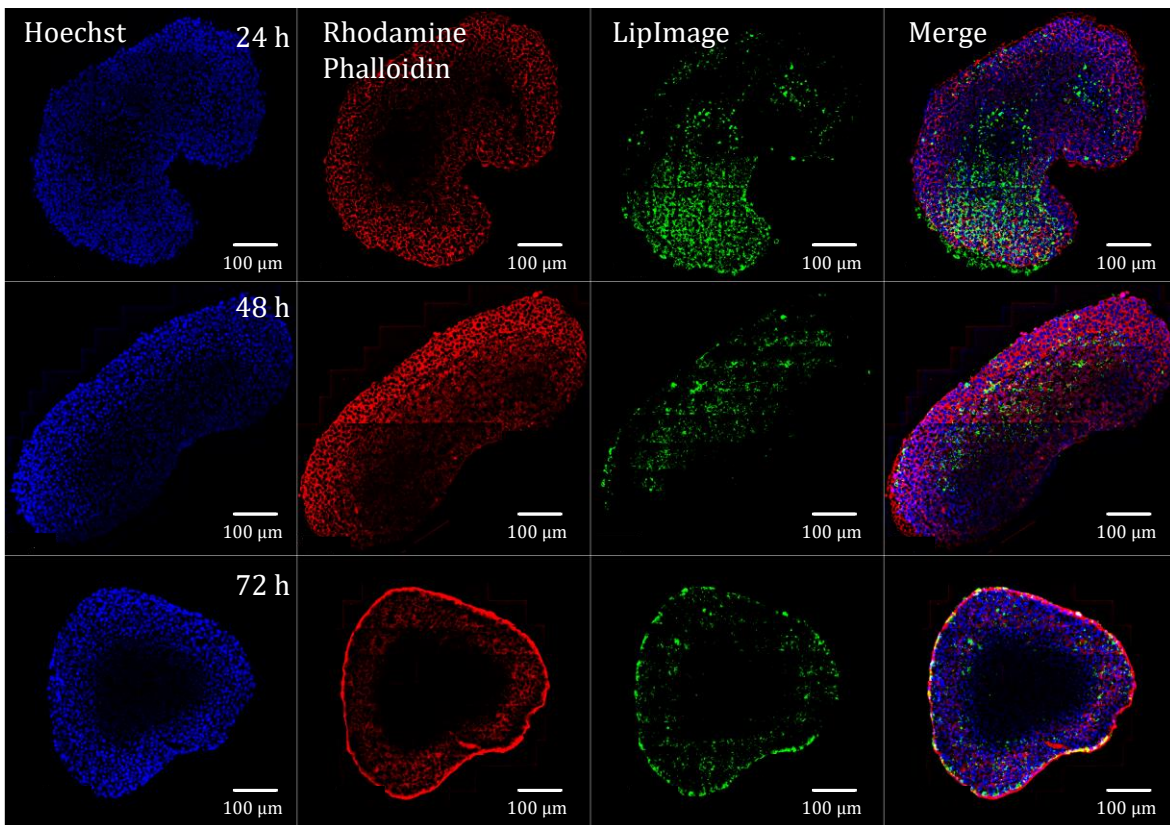


Figure 5.2. Colour confocal images of spheroids treated with 100 µg/ml of LipImage for 24 h, 48 h, and 72h. Spheroids were stained with Hoechst (nuclei – blue, 1:1000), Rhodamine phalloidin (actin – red, 1:40), treated with LipImage (green), and merged to show the localisation of LipImage through the spheroid.

Spheroids were treated with 100 µg/ml of LipImage for 24 h, 48 h, and 72 h. This concentration was the lower concentration selected for LipImage. Figure 5.2 column C clearly shows that even at lower concentrations, LipImage can easily penetrate to the core of the spheroid in 24 h, although the distribution does not appear to be as homogenous as it is at 48 h. By 72 h there is a notable absence of the NBM at the core, with what appears to be clustering observed at the periphery.

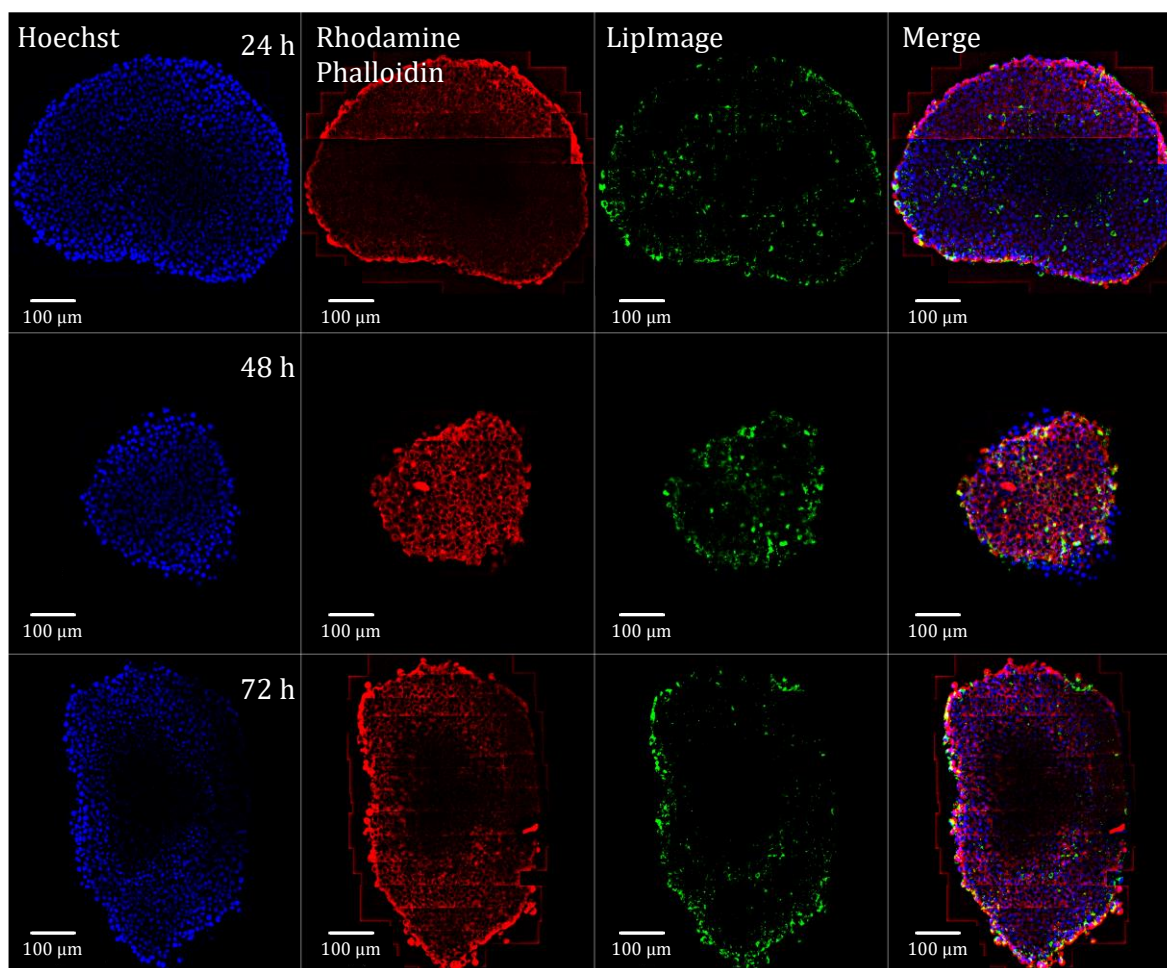


Figure 5.3. Colour confocal images of spheroids treated with 500 µg/ml of LipImage for 24 h, 48 h, and 72h. Spheroids were stained with Hoechst (nuclei – blue, 1:1000), Rhodamine phalloidin (actin – red, 1:40), treated with LipImage (green), and merged to show the localisation of LipImage through the spheroid.

This pattern in distribution is comparable to what was previously seen in Chapter 4, Figure 4.13 for treatment concentration of 200 µg/ml where core penetration was achieved by 24 h. Again, the distribution of the LipImage at 72 h shows that it is concentrated at the periphery of the spheroid. By increasing the concentration to 500 µg/ml, as shown in Figure 5.3, there are no observable differences in the distribution noted in the colour confocal images, when compared to the lower concentrations at all time points.

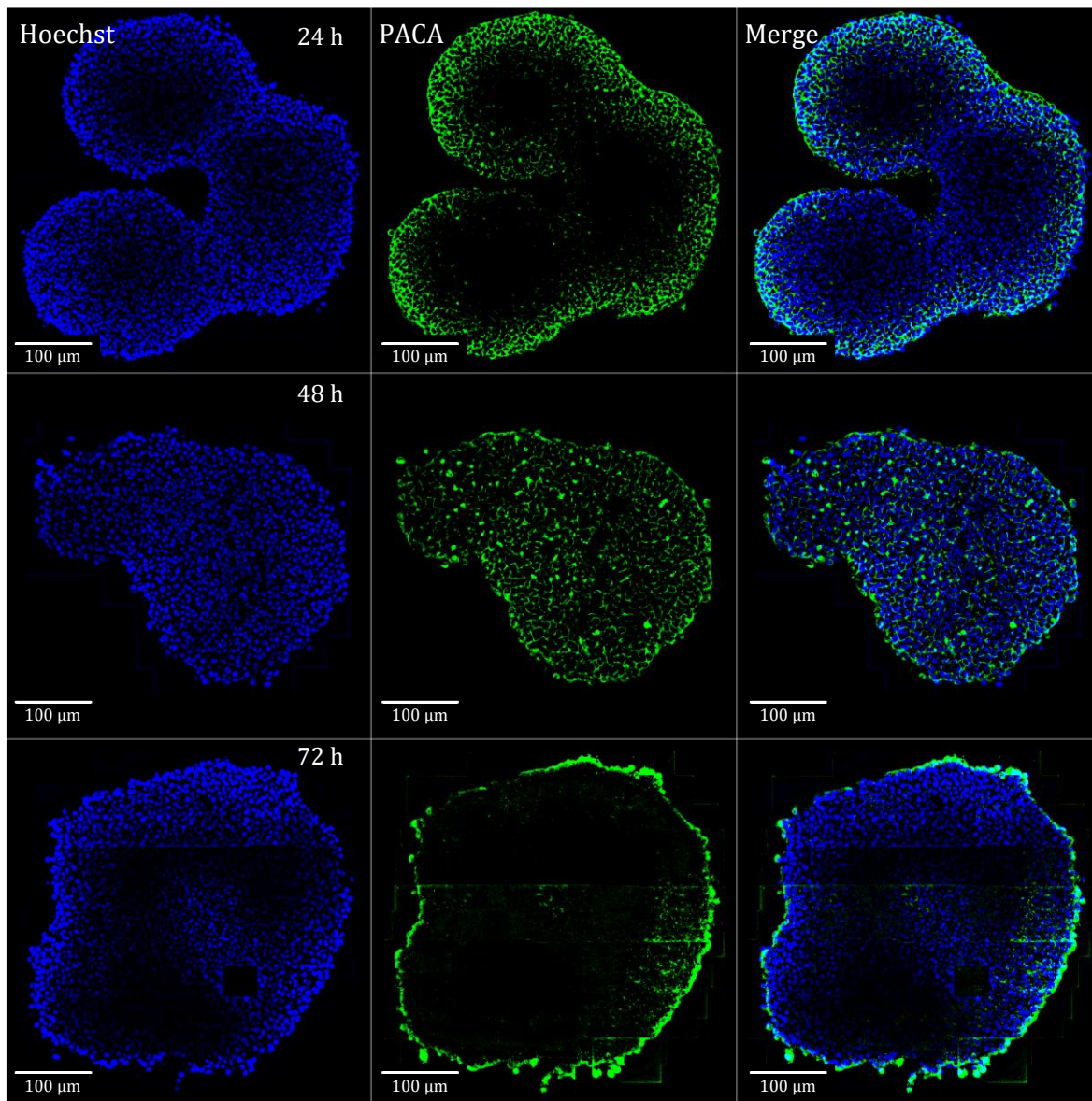


Figure 5.4. Colour confocal images of spheroids treated with 10 µg/ml of PACA for 24 h, 48 h, and 72 h. Spheroids were stained with Hoechst (nuclei – blue, 1:1000), treated with PACA (green), and merged to show the localisation of PACA through the spheroids.

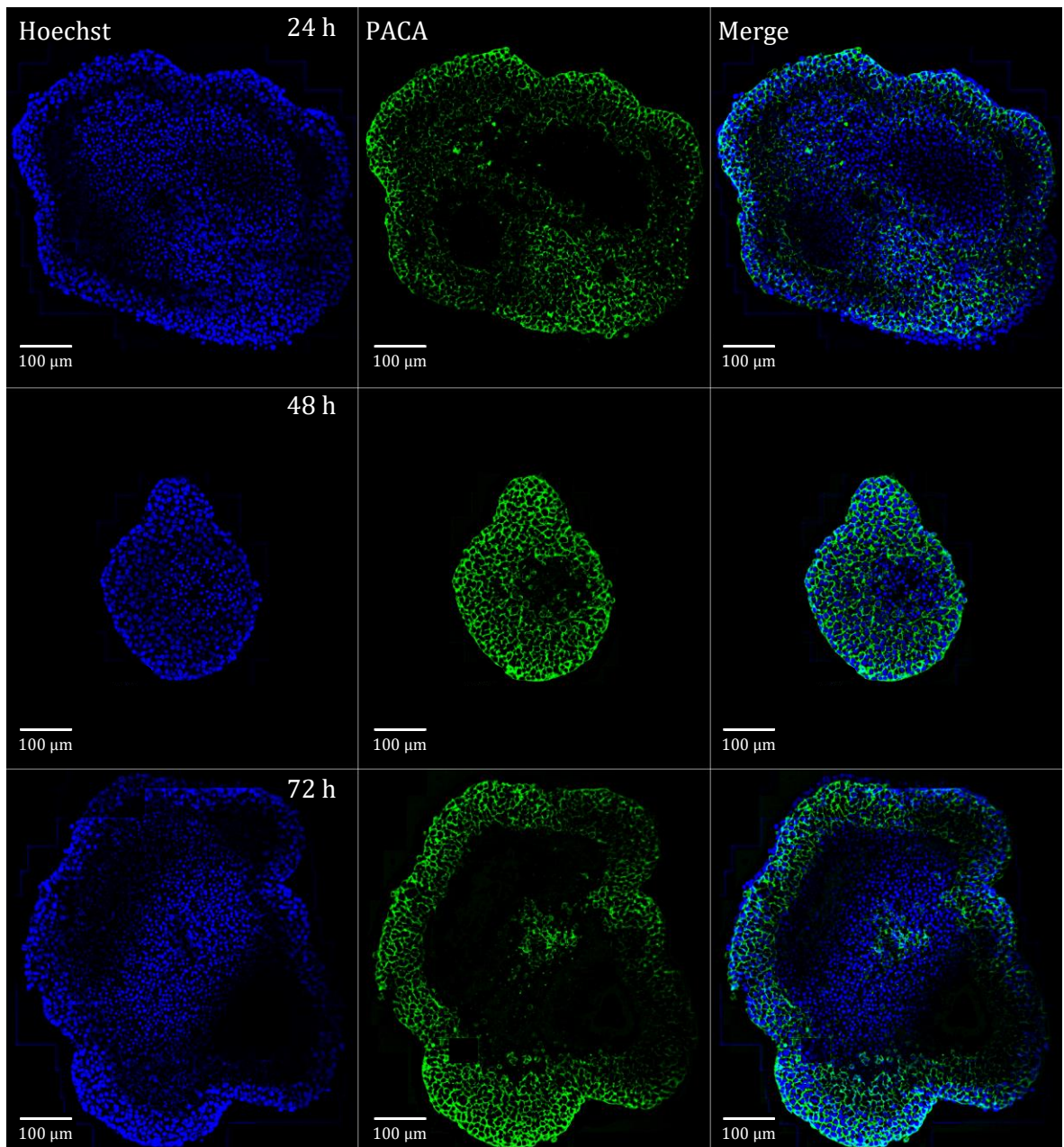


Figure 5.5. Colour confocal images of spheroids treated with 50 µg/ml of PACA for 24 h, 48 h, and 72 h. Spheroids were stained with Hoechst (nuclei – blue, 1:1000), treated with PACA (green), and merged to show the localisation of PACA through the spheroids.

For PACA, Figure 5.4, spheroids were treated with 10 µg/ml for 24 h, 48 h, and 72 h. As was seen in Figure 4.14, PACA does not penetrate to the core of the spheroid at 24 h. However, by 48 h, there is homogenous distribution of the NBM seen. By 72 h, while there appears to be some PACA at the core, it is predominately concentrated at the periphery, similar to the distribution pattern observed for low concentrations of LipImage at 72 h. By increasing the concentration to 50 µg/ml PACA finally penetrates the core at 24 h. However, at 48 h the core is not fully penetrated, as was previously

seen for lower concentrations. For 72 h, the NBM can be seen at the core, and at the periphery. Visual confirmation of the presence of the NMBs is useful and colour confocal images give an indication of the distribution of the NBM, using the raw intensity images will give quantifiable information about the NMBs.

5.2.3. Distribution of NMBs in HepG2 Spheroids

As previously mentioned, raw intensity images are required for quantitative data analysis of NMBs distribution and translocation in 3D hepatic spheroids. Figures 5.6 and 5.7 show the stitched, normalised intensity images for LipImage and PACA at their various concentrations, for three time points, 24, 48, and 72h, as described in Chapter 4, § 4.1.9. Here the images have been contrast-enhanced for visualisation purposes only.

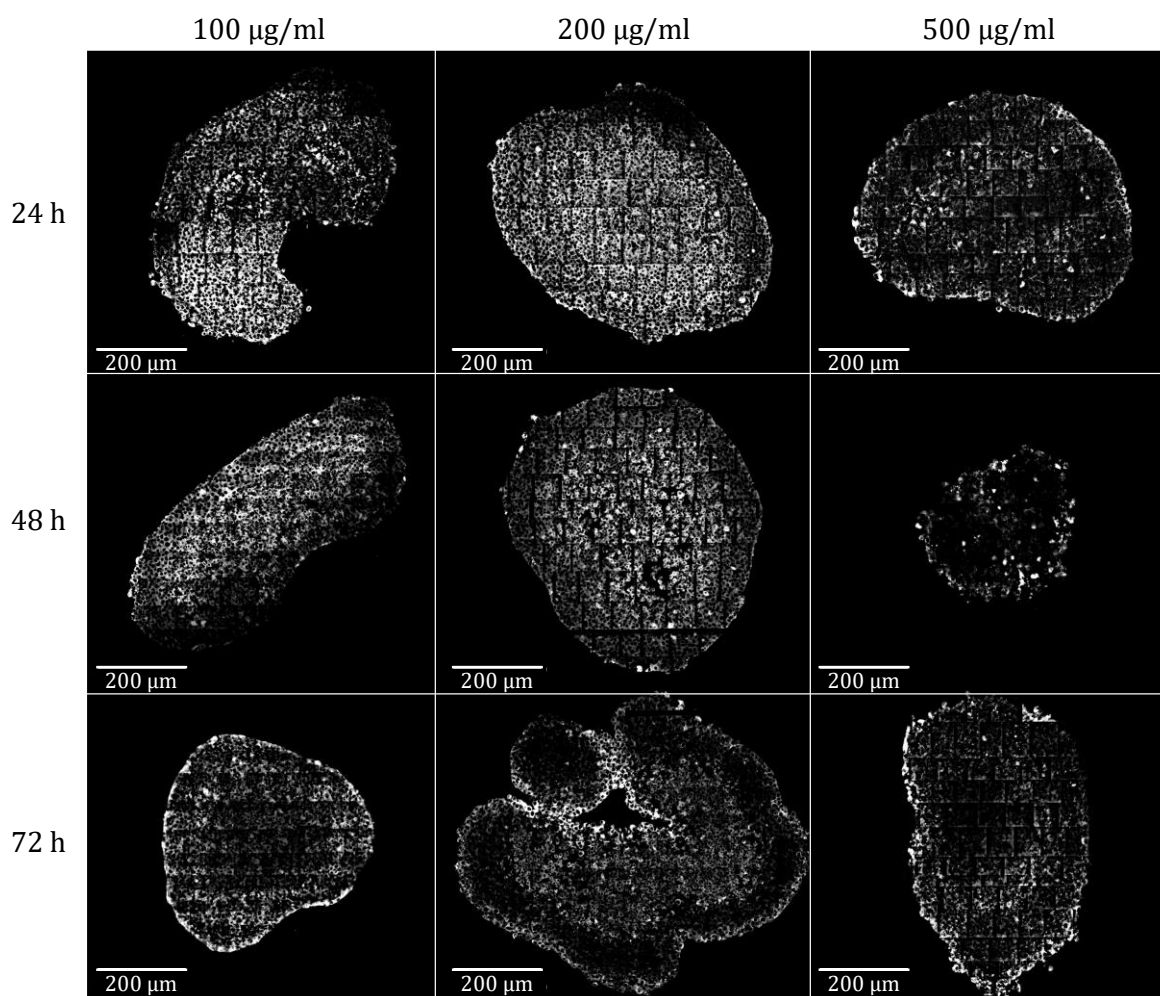


Figure 5.6. *Stitched, normalised intensity images of LipImage treated spheroids. HepG2 spheroids treated with 100, 200, and 500 $\mu\text{g/ml}$ of LipImage for 24 h, 48 h, and 72 h. Images acquired were $80 \times 80 \mu\text{m}^2$, that required normalisation and were subsequently stitched together for whole focal plane spheroid image analysis, as described in § 4.1.9. These images were used for all quantitative analysis carried out throughout this work. Here, images are enhanced.*

Further analysis of these images was carried out to establish if there is a pattern in the distribution of the NBMs through the core of the spheroid, and importantly, to probe if treatment time and concentration affect the translocation of the NBM across the spheroid.

Assuming a spheroid shape, the widest part of the spheroid was focused on, using brightfield microscopy. This will approximate the plane in the centre of the spheroid, as described in Figure 4.2, allowing analysis of the interaction of the NBM from the periphery to the core of the spheroid.

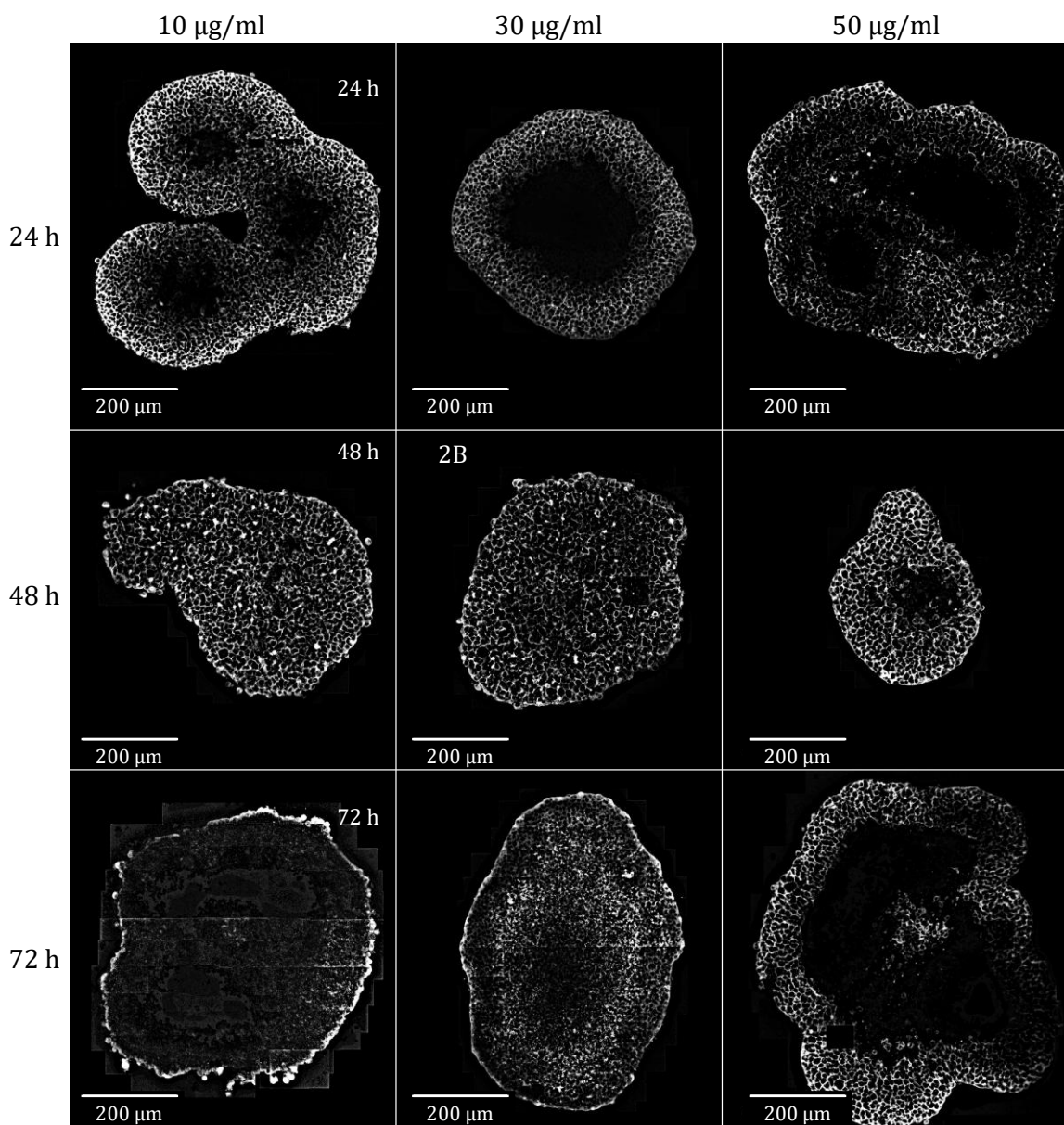


Figure 5.7. *Stitched, normalised intensity images of PACA treated spheroids. HepG2 spheroids treated with 10, 30, and 50 µg/ml of PACA for 24 h, 48 h, and 72 h. Images acquired were 80 × 80 µm², that required normalisation and were subsequently stitched together for whole focal plane spheroid image analysis, as described in § 4.1.9. These images were used for all quantitative analysis carried out throughout this work. Here, images are enhanced.*

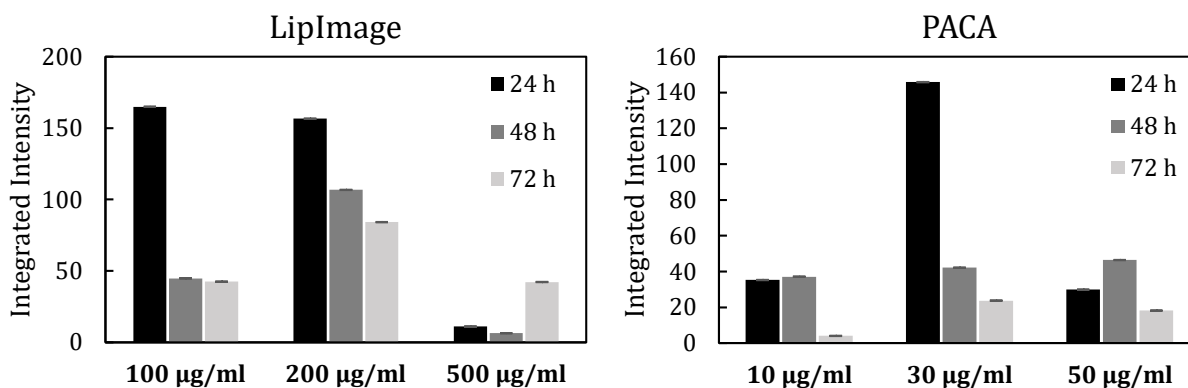


Figure 5.8. Integrated intensity for LipImage, and PACA. Stitched, normalised intensity images were used to measure the integrated intensity in the focal plane of the spheroids imaged. The mean intensity for each NBM is plotted, with the error bars representing the standard error of the mean.

Using the stitched, normalised intensity images from Figures 5.6 and 5.7, quantitative analysis of the translocation and distribution of the NBMs was carried out. Using the free hand tool in ImageJ, the periphery of each spheroid was marked, and the integrated fluorescence intensity was measured, as shown in Figure 5.8. LipImage, Figure 5.8A, has the lowest intensity observed at the highest concentration, 500 µg/ml, at all time points. This agrees with the normalised intensity images in Figure 5.6 (1C, 2C, and 3C) which show the distribution of the NBM to be less homogenous when compared to other concentrations. From Figure 5.8, 200 µg/ml has the highest intensity over all time points which again agrees with the images shown in Figure 5.6 .

PACA, on the other hand, despite not having a homogenous distribution, or the core of the spheroid being penetrated, has the highest intensity at 24 h for 30 µg/ml, with high intensity regions noted at the periphery of the spheroid. For all other time points, with the exception of 10 µg/ml at 72 h, there is little change in the intensity of PACA. While the intensity may not change, the distribution of the NBM is notably different over time and for different concentrations. By measuring the integrated fluorescence intensity of the whole image, neither LipImage or PACA appear to be well suited to treatment times of 72 h or beyond, as was concluded in Chapter 4. However, from the colour confocal images, 48 h appears to be an optimal treatment time, regardless of concentration.

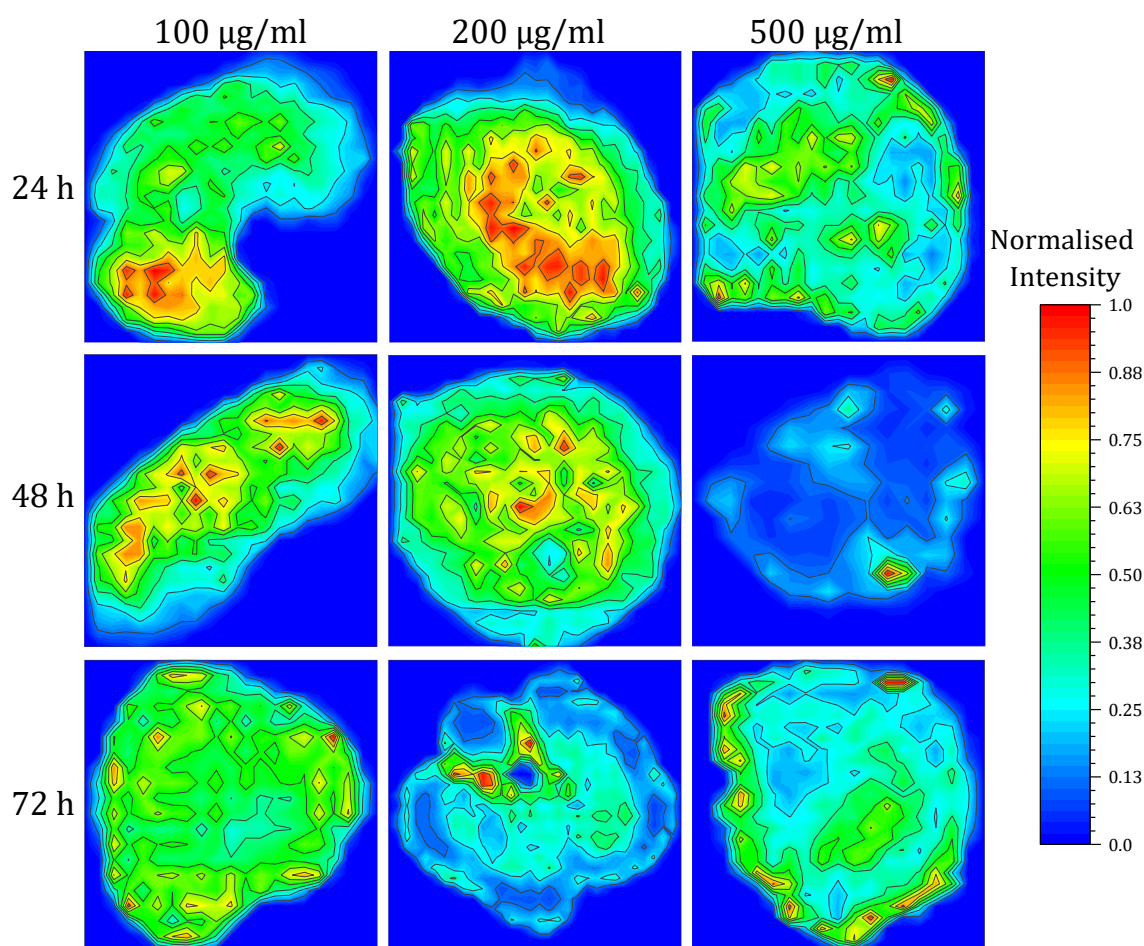


Figure 5.9. Colourmaps representing normalised LipImage translocation and penetration for 24 h, 48 h and 72 h, for 100 µg/ml, 200 µg/ml, and 500 µg/ml. Integrated intensity measurements of $26.7 \times 26.7 \mu\text{m}^2$ ($100 \text{ px} \times 100 \text{ px}$) area were made and plotted as colourmaps. Penetration to the core is noted at 24 h for all concentrations. By 48 h, distribution of LipImage has become almost homogenous. A notable change in distribution is noted at 72 h, with an increase in intensity observed at the periphery for 200 µg/ml and 500 µg/ml, and less NBM seen at the core. This could be due to the instability of the liposome housing the fluorescent dye.

Translocation of the NMBs and their penetrations to the core of the spheroid can be mapped by plotting colourmaps of the normalised integrated fluorescence intensity images. Integrated intensity measurements were made along the x - and y -axis of the spheroid, in an area about twice the size of an average cell. Using a bespoke MATLAB script, the integrated intensity images were rescaled using pixel binning ($100 \text{ px} \times 100 \text{ px}$), where the integrated intensity was then outputted as text file, imported into Origin and plotted as a colourmap. Figure 5.11 shows that for LipImage the core is indeed penetrated at 24 h, and with increasing concentration a more homogenous distribution is apparent. However, up to 72 h little NBM is seen at the core, in fact, it is mostly

concentrated at the periphery, in particular for the higher concentration. However, at 72 h 200 µg/ml, while degradation is observed at the periphery relative to the core, the core still has an intensity that is comparable to the core at 24 h. This was also seen in Chapter 4, § 4.2.5, where at 72 h a degradation in the LipImage was seen. At 72 h, 100 µg/ml, when compared to earlier time points, there is a more homogenous distribution of the NBM within the spheroid, but with some higher accumulation of the NBM observed at the periphery. The distribution pattern at 72 h comes with a significant decrease in intensity. From the colour maps of Figure 5.19, 24 h appears to be an optimum treatment time for LipImage.

Looking at PACA in Figure 5.12 the colourmaps indicate that at 24 h the NBM is concentrated at the periphery of the spheroid. Increasing the concentration increases the amount at the periphery, but also allows for some to penetrate to the core. However, it is not until 48 h, for all concentrations, that a homogenous distribution is noted. As seen with LipImage at 72 h, the distribution is more concentrated at the periphery than at the core, and in some instances, with both the 10 and 50 µg/ml showing very little at the core. While PACA is a more biopersistent NBM, neither NBM would be suitable for long exposure treatments. Ideally, LipImage would need no more than 48 h, and PACA would require at least 48 h to penetrate to the core, and have a homogenous distribution.

The colour maps for PACA are shown in Figure 5.10. As was seen in Chapter 4, PACA requires 48 h to reach the core of the spheroid with a homogenous distribution of the NBM through the spheroid. However, by increasing the concentration of PACA to 50 µg/ml the NBM can reach the core of the spheroid. At 72 h PACA, the intensity at the core for 10 µg/ml and 50 µg/ml, when compared to 30 µg/ml, appears to be very low, however, it is comparable when the line plots from Figure 5.10 are taken into consideration. In all cases, at 72 h there is a decrease in intensity through the core, and an accumulation at the periphery. This could be due to a degradation in the polymer shell of PACA. The size of PACA may also be a contributing reason to why higher intensities are seen at the periphery. PACA is larger than LipImage and would therefore have less room to manoeuvre within the tight intracellular space close to the core as discussed in Chapter 2.

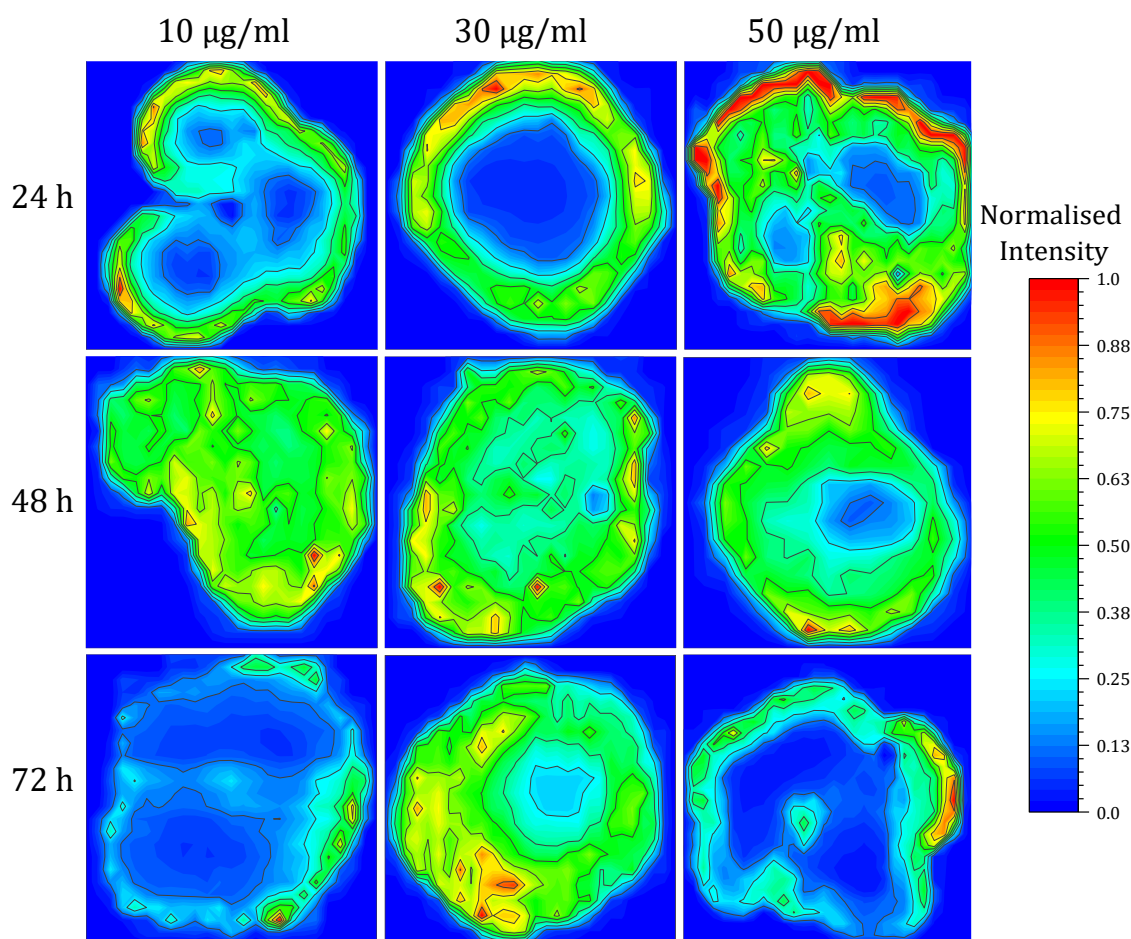


Figure 5.10. Colourmaps representing normalised PACA translocation and penetration for 24 h, 48 h, and 72 h, for 10 $\mu\text{g/ml}$, 30 $\mu\text{g/ml}$, and 50 $\mu\text{g/ml}$. Integrated intensity measurements of a $26.7 \times 26.7 \mu\text{m}^2$ ($100 \text{ px} \times 100 \text{ px}$) area were made and plotted as colourmaps. These maps indicate the translocation and penetration of PACA over time. After 24 h PACA is concentrated at the periphery of the spheroid, with concentrations requiring at least 48 h to penetrate to the core of the spheroids where a homogenous distribution can be seen. Again, at 72 h, a decrease in intensity seen at the core, with the majority of the NMB located at the periphery of the spheroid can be seen.

Overall, the colourmaps show the translocation of the NBMs, and their penetration to the core. The colour maps show that LipImage penetrates faster to the core of the spheroid, over all concentrations, and when combined with the information obtained from the line plots, achieves a more homogenous distribution when it is compared to PACA. This is in overall agreement with observations made in Chapter 4. It can also be said that increasing the concentration is not beneficial for LipImage, but lowering the concentration can achieve core penetration with a homogenous distribution. But for PACA, increasing the concentration will allow for core penetration at 24 h, and

lowering the concentration to 10 $\mu\text{g/ml}$ will give the same penetration and distribution at 24 h as those achieved with 30 $\mu\text{g/ml}$ at 48 h. Overall, differences in the translocation and distribution of the two NBMs was noted, something which has been seen in *in vivo* studies of polymeric and lipid-based nanoparticles by Åslund *et al.*, [162].

5.2.4. Fluorescence Lifetime Imaging Microscopy

While carrying out confocal microscopy, fluorescence lifetime imaging microscopy (FLIM) was carried simultaneously. Information obtained from the line plots and colourmaps suggested that degradation or quenching of the NBMs is occurring. FLIM can be used to determine if this is the case. Fluorescence lifetime is a fundamental property of a fluorophore, that does not depend on concentration [163] and is not typically affected by photobleaching [164]. It is, however, affected by other external factors, such as microenvironment, temperature, pH, and the presence of fluorescence quenchers [165,166].

From the lifetime data obtained, the average fluorescence lifetime decay curves were plotted and normalised, as shown in Figure 5.13. Using Equation 4.1, a one-exponential decay for LipImage [167], and Equation 4.2, a two-exponential decay for PACA [168,169], the normalised decay curves were fitted. The amplitudes and decay components, shown in Table 5.2 and 5.3, were extracted from the fitted decay curves. For LipImage, as a one-exponential fit was used, the average lifetime does not require calculation. For PACA, as a two-exponential fitted decay curve was used Equation 4.4 calculated the amplitude weighed average lifetime. Chapter 4 showed that for one concentration, there was no difference noted in the average lifetime for the two NBM a trend which is also seen in Tables 5.2 and 5.3.

Table 5.2. Table of data obtained from normalised fitted fluorescence lifetime decay graphs for LipImage, using a one-exponential fit, where τ_1 is the average decay.

Time (h)	Concentration ($\mu\text{g/ml}$)	τ_{avg} (ns)
24	100	1.0 ± 0.1
24	200	1.1 ± 0.1
24	500	1.1 ± 0.1
48	100	1.0 ± 0.1
48	200	0.9 ± 0.1
48	500	1.1 ± 0.1
72	100	1.1 ± 0.1
72	200	1.1 ± 0.1
72	500	1.0 ± 0.1

Table 5.3. Table of data obtained from normalised, fitted fluorescence lifetime decay graphs for PACA, using a two-exponential fit, where A_1 and A_2 are the amplitudes, and τ_1 and τ_2 are the fast and slow decay components. The amplitude weighted average lifetime for PACA was calculated using Equation 4.4

Time (h)	Concentration ($\mu\text{g/ml}$)	A_1	τ_1 (ns)	A_2	τ_2 (ns)	τ_{avg} (ns)
24	10	0	1.6	1	3.5	3.1 ± 0.3
24	30	1	2.4	0	6.2	3.7 ± 0.2
24	50	0	0.9	1	3.3	3.0 ± 0.8
48	10	0	1.1	1	3.4	3.1 ± 0.1
48	30	0	1.2	1	3.5	3.2 ± 0.3
48	50	0	0.9	1	3.3	3.0 ± 0.8
72	10	0	1.1	1	3.6	3.3 ± 0.1
72	30	0	1.4	1	3.9	3.5 ± 0.1
72	50	0	1.2	1	3.4	3.2 ± 0.1

The decay curves in Figure 5.11 show that LipImage has a much shorter lifetime when compared to PACA. A study by Nagy-Simon *et al.*, showed that IR780, the fluorescent dye in LipImage, has an average lifetime of 0.65 ns in Dymethylsulphoxide (DMSO) [152]. However, Bruun and Hille showed that encapsulating a dye in a liposome can increase the lifetime [170]. PACA has been shown by Sulheim *et al.*, to have a lifetime of 3.3 ns [171]. The lifetimes for both NBMs are within the ranges for both NBMs seen past studies [172,173].

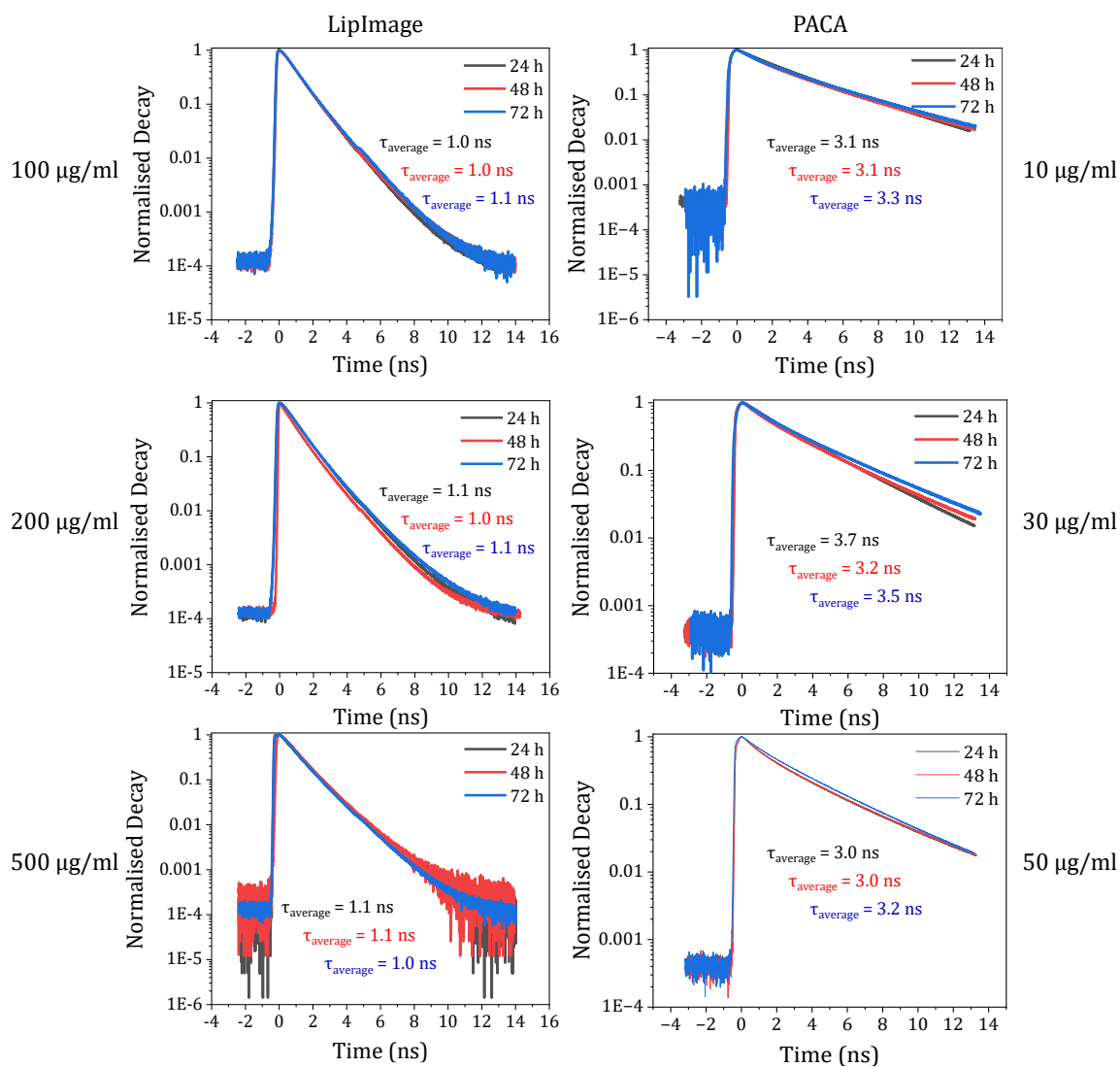


Figure 5.11. Fluorescence lifetime decay curves. Spheroids treated with LipImage and PACA, at 100 $\mu\text{g/ml}$, 200 $\mu\text{g/ml}$, and 500 $\mu\text{g/ml}$, and 10 $\mu\text{g/ml}$, 30 $\mu\text{g/ml}$, and 50 $\mu\text{g/ml}$ respectively. Using a non-linear, one- or two-exponential decay fitted curve, the amplitudes, and decay times were extracted, and using Equations 4.3 and 4.4, the average lifetime for both NBMs were calculated.

The lifetimes from Table 5.2 and Table 5.3 show that distribution and translocation of the NBM appears to have no effect on the lifetime of the NBM. However, the lifetimes shown in Tables 5.2 and 5.2 are average lifetime of the whole focal plane of the spheroid. There is a decrease in intensity and distribution noted between core and periphery for several concentrations and treatment time points. An examination of the lifetimes at the core and periphery of the spheroids was carried out to determine if there was any correlation, shown in Figure 5.12.

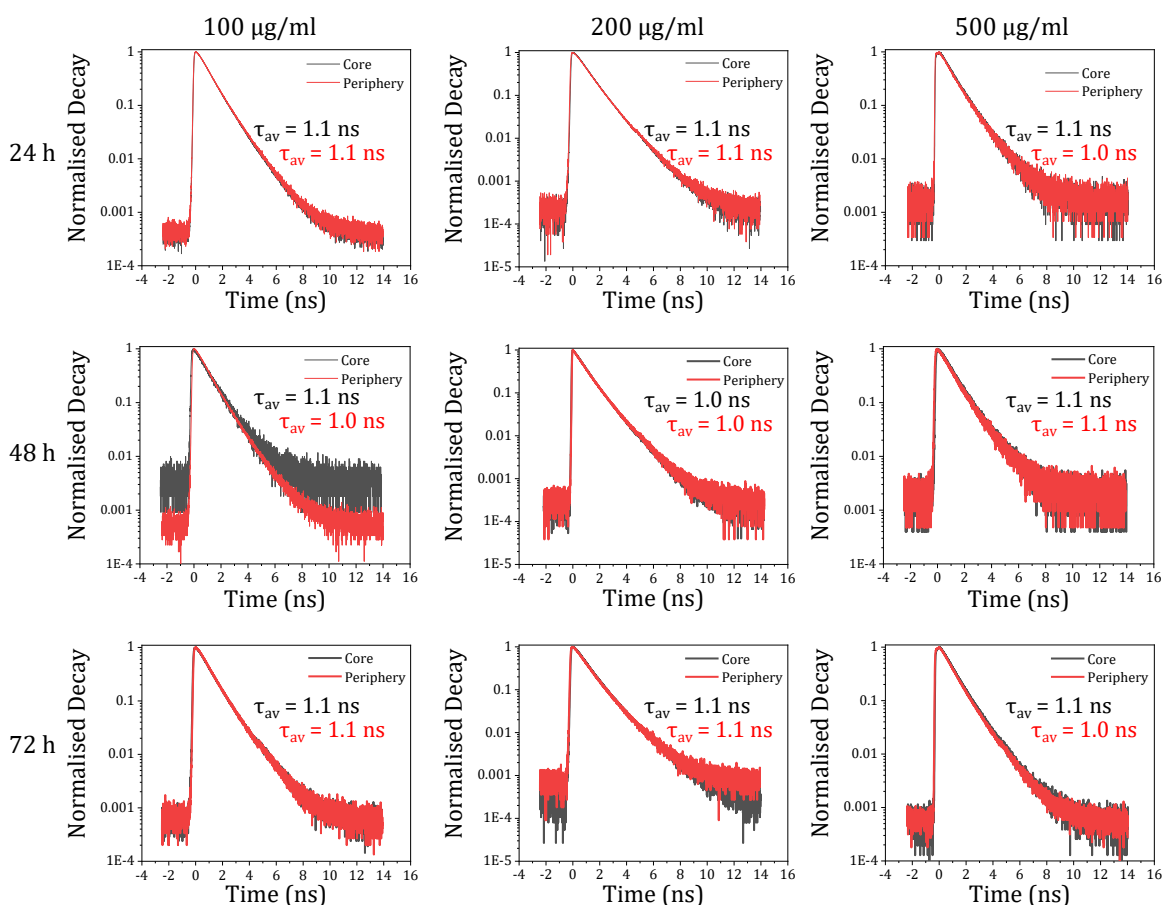


Figure 5.12. Fluorescence Lifetime Decay Curves for LipImage at the core and periphery of a spheroid, for 100 µg/ml, 200 µg/ml, and 500 µg/ml, at 24 h, 48 h, and 72 h. For each treatment time and concentration, an image, with an area of $80 \times 80 \mu\text{m}^2$, was selected at the periphery of the spheroid, and as close to the core as was possible, to determine if location of the NBM had an effect on the lifetime of the NBM.

A $80 \times 80 \mu\text{m}^2$ image was selected at or near the core of the spheroid, and at the periphery. Table 5.4 shows that there is no significant difference in the lifetimes observed at the core or at the periphery, in any case. This suggests that the decrease in the intensity observed for LipImage in Figure 5.8 and Figure 5.9 is quenching of the NBM due to degradation of the liposome and exposure of IR780 to water, and that distribution and translocation have no bearing on the lifetime of the NBM.

Table 5.4. Table of data obtained from normalised, fitted fluorescence lifetime decay graphs for LipImage using a one-exponential decay fit, where A_1 is the amplitude and τ_1 is the decay. For each time and concentration an image was selected at the core of the spheroid and at the periphery. The amplitude weighted average lifetime was calculated for each position.

Time (h)	Concentration ($\mu\text{g/ml}$)	Location	A_1	τ_1 (ns)	τ_{avg} (ns)
24	100	Core	1.1	1.1	1.1 ± 0.1
24	100	Periphery	1.1	1.1	1.1 ± 0.1
48	100	Core	1.0	1.1	1.1 ± 0.2
48	100	Periphery	1.1	1.0	1.0 ± 0.1
72	100	Core	1.1	1.1	1.1 ± 0.1
72	100	Periphery	1.1	1.1	1.1 ± 0.1
24	200	Core	1.1	1.1	1.1 ± 0.1
24	200	Periphery	1.1	1.1	1.1 ± 0.1
48	200	Core	1.0	1.0	1.0 ± 0.2
48	200	Periphery	1.0	1.0	1.0 ± 0.2
72	200	Core	1.1	1.1	1.1 ± 0.1
72	200	Periphery	1.0	1.1	1.1 ± 0.1
24	500	Core	1.1	1.1	1.1 ± 0.1
24	500	Periphery	1.0	1.0	1.0 ± 0.1
48	500	Core	1.1	1.1	1.1 ± 0.2
48	500	Periphery	1.0	1.1	1.1 ± 0.2
72	500	Core	1.1	1.1	1.1 ± 0.1
72	500	Periphery	1.0	1.0	1.0 ± 0.1

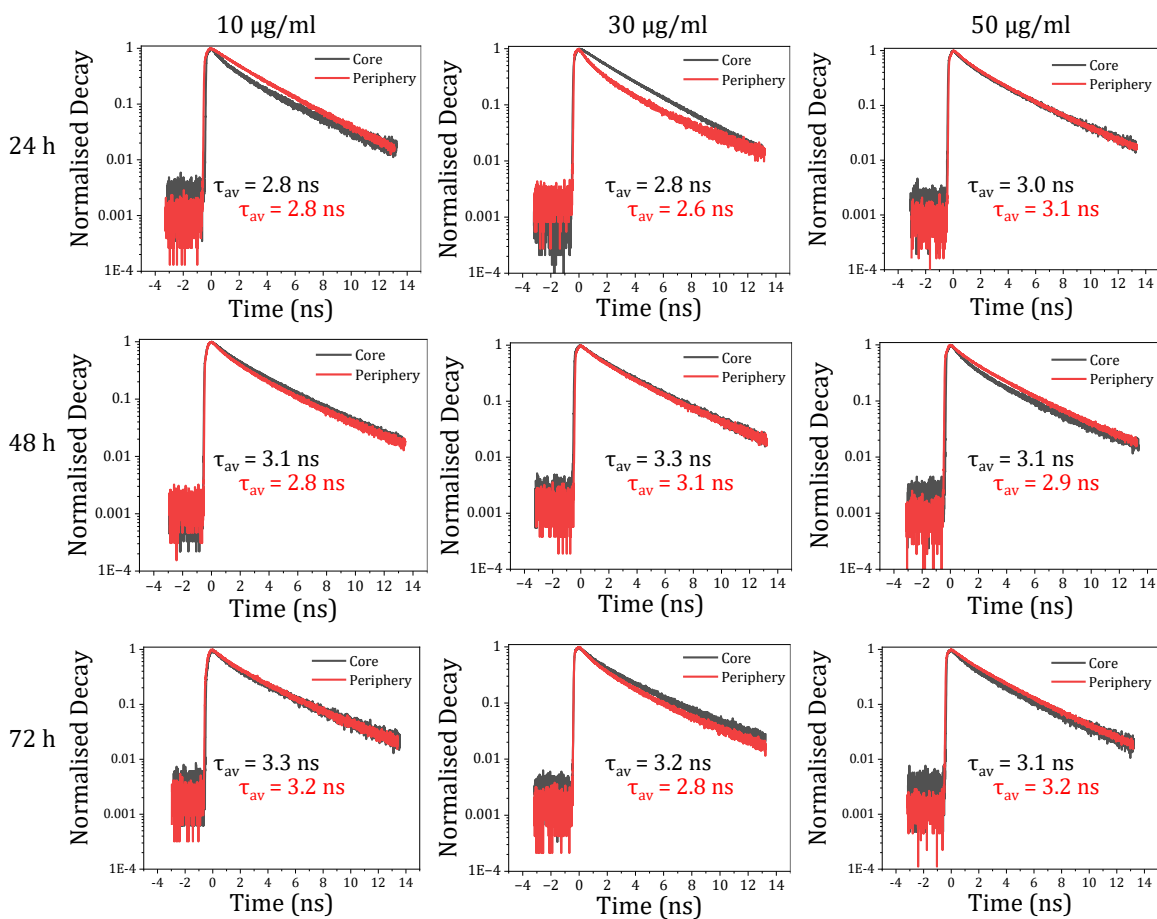


Figure 5.13. Fluorescence Lifetime Decay Curves for PACA at the core and periphery of a spheroid, for 10 µg/ml, 30 µg/ml, and 50 µg/ml, at 24 h, 48 h, and 72 h. For each treatment time and concentration, an image, with an area of $80 \times 80 \mu\text{m}^2$, was selected at the periphery of the spheroid, and as close to the core as was possible, to determine if location of the NBM had an effect on the lifetime of the NBM. With the exception of 30 µg/ml at 24 h and 72 h, and 50 µg/ml at 72 h, the decay curves, fitted with a two-exponential decay curve, show close agreement.

Similarly, the lifetime decay of PACA, shown in Figure 5.13, was examined at the core and periphery of spheroids, shown in Table 5.5. Again, no significant difference was observed between the core and the periphery.

Table 5.5. Table of data obtained from normalised, fitted fluorescence lifetime decay graphs for PACA using a two-exponential decay fit, where A_1 and A_2 are the amplitudes, and τ_1 and τ_2 are the slow and fast decay components. For each time and concentration an image was selected at the core of the spheroid, and at the periphery. The amplitude weighted average lifetime was calculated for each position.

Time (h)	Concentration ($\mu\text{g/ml}$)	Location	A_1	τ_1 (ns)	A_2	τ_2 (ns)	τ_{avg} (ns)
24	10	Core	0	0.8	0.6	3.1	2.8 ± 0.1
24	10	Periphery	-	-	1.0	2.8	2.8 ± 0.3
48	10	Core	0	1.1	0.7	3.4	3.1 ± 0.3
48	10	Periphery	0	1.0	0.6	3.1	2.8 ± 0.2
72	10	Core	0	1.0	0.6	3.7	3.3 ± 0.4
72	10	Periphery	0	1.1	0.7	3.5	3.2 ± 0.1
24	30	Core	-	-	2.0	2.8	2.8 ± 0.3
24	30	Periphery	1	0.8	0.5	3.0	2.6 ± 0.2
48	30	Core	0	1.3	0.7	3.6	3.3 ± 0.8
48	30	Periphery	0	1.1	0.7	3.4	3.1 ± 0.4
72	30	Core	0	1.0	0.6	3.6	3.2 ± 0.4
72	30	Periphery	1	0.9	0.6	3.3	2.8 ± 0.2
24	50	Core	0	0.9	0.6	3.3	3.0 ± 0.2
24	50	Periphery	0	1.0	0.7	3.4	3.1 ± 0.2
48	50	Core	0	1.0	0.7	3.3	3.1 ± 0.2
48	50	Periphery	1	0.9	0.5	3.3	2.8 ± 0.2
72	50	Core	0	0.9	0.6	3.4	3.1 ± 0.2
72	50	Periphery	0	1.3	0.7	3.5	3.2 ± 0.1

5.3. Diffusion

Using the Stokes Einstein equation, Equation 5.1, the diffusion constant was calculated for both NBMs at both 20 °C, room temperature, and at 37 °C, incubation temperature. From this, the root mean square displacement, Equation 5.2 was calculated, giving an estimate of the diffusion of the NBMs over a 24 hour period. Table 5.2 shows the radius of the spheroids used in this work with Table 5.3 showing the diffusion of the NBMs at both RT and treatment temperature for 24 h, 48 h, and 72h. An increase in the diffusion of the NBMs was observed at the higher temperature. From these calculations, it could be estimated how far into the spheroid the NBMs can potentially travel. These calculations are based on a spheroid with the NBMs unimpeded due to no internal structures.

$$D = \frac{k_B T}{6\pi\eta r}$$

Equation 5.1

where

η = dynamic viscosity (mPa s) (water – 1 mPa s)

r = radius of the spherical particle (nm)

k_B = Boltzmann constant = $1.38 \times 10^{-23} \text{ J}\cdot\text{K}^{-1}$

T = Absolute temperature (K)

Table 5.6. Diffusion Constant for LipImage and PACA at room temperature, 20 °C, and treatment temperature, 37 °C

NBM	Temperature (°C)	NBM radius (nm)	Diffusion Constant (m ² /s)
LipImage	20	50	4.29×10^{-12}
LipImage	37	50	4.54×10^{-12}
PACA	20	140	1.53×10^{-12}
PACA	37	140	1.62×10^{-12}

$$\sqrt{\langle r^2 \rangle} = \sqrt{6Dt}$$

Equation 5.2

where

D = diffusion constant (m²/s)

t = time

Table 5.7. Distance NBMs can potentially travel at both room temperature and treatment temperature for 24 h, 48 h, and 72 h.

	LipImage (μm)	PACA (μm)
24 h @ RT	192.5	115.1
24 h @ 37 °C	198.1	118.3
24 h @ RT	272.3	162.7
24 h @ 37 °C	280.1	167.3
24 h @ RT	335.0	199.0
24 h @ 37 °C	343.0	204.9

From these calculations, it can be seen that the time required to penetrate to the core of the spheroid is spheroid size dependent. The spheroids used varied in size, independently of the concentration of the NBM. From Table 5.7, and Table 5.8, penetration of LipImage to the core of the spheroid could be achieved for the spheroid treated with 500 $\mu\text{g}/\text{ml}$ for 48 h. Similarly, PACA could penetrate to the core of the spheroid treated with 50 $\mu\text{g}/\text{ml}$ for 48 h. However, it has already been seen that LipImage can penetrate to the core of the spheroid for low concentrations at 24 h, seen in Figure 5.11. While PACA does require 48 h, it can be achieved at a lower concentration, seen in Figure 5.12. This suggests that there is an mechanism within the spheroid that is adding with the diffusion of the NBMs, and requires further study.

Table 5.8. The measured *radius* for each spheroid .

LipImage			PACA		
Time (h)	Concentration ($\mu\text{g/ml}$)	Radius (μm)	Time (h)	Concentration ($\mu\text{g/ml}$)	Radius (μm)
24	100	277.15	24	10	297.29
24	200	318.39	24	30	252.32
24	500	313.59	24	50	331.62
48	100	310.39	48	10	279.55
48	200	294.77	48	30	239.50
48	500	177.82	48	50	161.27
72	100	236.70	72	10	290.77
72	200	395.16	72	30	232.29
72	500	210.27	72	50	320.40

5.4.Conclusion

Using the direct imaging method explored in Chapter b 4, and expanding the experimental parameters to include both higher and lower concentrations for both NBMs over the same treatment time, the translocation and penetration of the NBMs in a 3D hepatic *in vitro* model was investigated. In Chapter 4 it was observed that LipImage only required 24 h. Here, it was seen that this is still valid, with lower concentrations of 100 $\mu\text{g/ml}$ allowing for penetration of the core. However, there was a more homogenous distribution and translocation of the NBM seen at 48 h. This was also the case for PACA, at 48 h and 10 $\mu\text{g/ml}$ penetration to the core of the spheroid was achieved. PACA also showed for higher concentrations, 50 $\mu\text{g/ml}$, penetration to the core was achieved at 24 h, however, the majority of the NBM is still located at the periphery of the spheroid, and there is not a homogenous distribution, with areas the NBM has not fully reached. 72 h, for both NBMs, at higher or lower concentrations, as

was previously seen, results in inhomogeneous distribution, and decrease in overall fluorescence intensity, making both NBMs unsuitable for treatment up to, and beyond 72 h.

No significant change in fluorescence lifetime was observed in either of the NBMs. When this is compared to the translocation and biodistribution of the NBM, it may be expected that a decrease in the lifetime might be observed where there is a decrease in intensity, or a less homogenous distribution seen. This is not the case, with no change seen at the core or periphery. Therefore, the decrease in intensity noted for both NBMs at 72 h can be attributed to a degradation of the liposome or polymeric shell housing the fluorescence dyes, and their subsequent quenching in water.

Diffusion of the NBMs into the spheroid was examined by calculating the diffusion constant and root mean displacement of the NBMs using a simple diffusion model. From this it was observed that the NBMs diffuse to the core of the spheroid faster than the model suggests. This implies another mechanism adding the diffusion of the NBMs into the spheroid.

Chapter 6 Conclusion and Future Work

The main focus of this work was the optical characterisation of nanoparticles (NPs) used in two distinct areas: nanoimprint lithography of thin film gratings, and bioimaging of nanobiomaterials (NBMs) in a 3D hepatic *in vivo* model (spheroid).

Metallic nanoparticle ink was investigated in Chapter 3 by using a solution based nanoimprint lithography method to fabricate a silver thin film grating from silver nanoparticle ink. The properties of silver nanoparticle ink grating and planar samples, with and without a PMMA layer, were compared with thermally evaporated silver on nanoimprinted PMMA. The grating pattern was successfully fabricated using nanoimprint lithography with AgNPI directly onto a glass substrate, and on a PMMA layer. The use of the PMMA was found to adversely affect the structural, optical, and electrical properties of the silver nanoparticle planar surfaces, and gratings. However, the gratings nanoimprinted directly into AgNPI on a glass substrate were found to have similar performance to gratings produced by thermal evaporation, and benefit from an easier fabrication process. The AgNPI showed promise for the fabrication of patterned silver thin films, and may be useful for upscaling and roll-to-roll processes. Further exploration of the fabrication of the mould, by changing the grating periodicity, shape, or height of the nanostructures could lead to enhancement in photoluminescence, or increased reflectivity.

Chapter 4 investigated the translocation and trafficking of two NBMs, one a liposome, and one a polymer, both loaded with fluorescent dyes. The main objective of this work was to investigate the use of a direct imaging method, to determine the penetration and distribution of the NBMs within a hepatic 3D *in vivo* model. Previously, work carried out, and indeed the gold standard of fluorescence microscopy, relies on the use of fluorescently labelling the NBM. However, the use of the direct imaging method not only saves time and resources, but also reduces the risk of introducing contaminants into the culture process, and also takes full advantage of the near-IR dye encapsulated by the NBM, LipImage. This chapter showed that the detection of the NBMs, directly imaged, without fluorescent labelling was achievable. However, despite this there were some drawbacks. The fluorescent dye encapsulated within the liposome was highly sensitive to photobleaching, and due to the nature of the imaging system, and the

requirement for overlapping of imaging, an amount of photobleaching was introduced into the final image. However, the overall results were not affected. For this work, one treatment concentration, and three treatment time points were selected for each NBM. It was determined that for LipImage, the shortest treatment time was adequate for the NMB to penetrate to the core. Longer treatment times, of up to 72 h, were determined to be not suitable for LipImage, due to possible degradation of the liposome, and the releasing of the encapsulated dye, IR780, which was subsequently quenched by the water within the spheroid. Homogenous distribution was realised at 48 h treatment. While looking at PACA, it was seen that 24 h was an insufficient treatment time to allow the NBM to fully penetrate to the core. After 48 h, core penetration was achieved, along with a homogenous distribution of the NBM. Similarly to that seen for LipImage, at treatment times of up to 72 h, and beyond, a decrease in the NBM was visualised, and it was determined that for this concentration, this was also an unsuitable treatment time.

Chapter 5 expanded the experimental parameters of Chapter 4 by introducing a higher and lower concentration of the NMBs. For LipImage, no advantage to increasing or decreasing the concentration was observed at 24 h, with the original concentration proving to be sufficient for that time point. However, lowering the concentration allowed penetration to the core to be achieved, and provided a more homogenous distribution of the NBM. However, increasing the concentration, while penetration to the core was achieved, clusters of the NMB were observed at the periphery, which was not previously noted. These observations were also noted for 48 h treatment time, but with a more homogenous distribution seen for the lower concentration. Again for high concentrations, the NBM was located mostly close to the periphery. Despite the longer treatment time, a lower concentration showed a uniform distribution of the NBM, while at increased concentrations, degradation was noted, and the NBM was once more located at the periphery of the spheroid.

Overall for PACA, while maintaining the treatment time at 48 h, the treatment concentration did not have an effect on the translocation of the NMB, with homogenous distribution noted, and penetration of the core achieved. At 24 h, increasing the treatment concentration allowed for the core of the spheroid to be penetrated, however, there appears to be a lot of clustering observed around the periphery of the

spheroid, and no homogenous distribution seen, with areas appearing to have no NBM.

The lifetimes of the NBMs do not appear to be affected by the internal structure, concentration, treatment time, or by the distribution and translocation of the NBMs. The decrease in intensity noted at longer treatment times can be attributed to the degradation of the liposome and polymeric shell housing the fluorescent dyes. The degradation will release the fluorescent dyes, which will become quenched in the presence of water.

6.1. Future Work

The work on spheroids and NBMs has shown that small NPs have the ability to penetrate to the core of a spheroid, and potentially to the core of a tumour. By utilising a direct imaging method to localise LipImage, full advantage of a near-IR fluorescent dye was achieved, i.e., imaging within the biological window. Near-IR fluorescence imaging (NIRF) is becoming a convenient alternative to other non-invasive imaging modalities, such as computed tomography (CT), magnetic resonance imaging (MRI), and positron emission tomography (PET). These imaging modalities play key roles in pre-clinical assessments, but also in clinical diagnosis, evaluation of disease, as well as treatment of tumours. NIRF allows for low NIR absorption and scattering by tissue, and low auto-fluorescence from surrounding tissues in tumour detections [174–177] and shows promising results in clinical image-guided oncological surgery [178–180]. In this thesis it has been shown that the chosen NBMs are stable within a 3D *in vivo* model, for up to 72 h, before degradation occurs. This makes them an ideal candidate for both pre-clinical and clinical NIRF.

The work in this thesis could be further expanded by carrying out live cell imaging to determine the diffusion coefficient. From calculations presented in this work in Chapter 5, the migration of the NBMs using a simple diffusion process determined the distance into the spheroids the NBMs could travel over a period of time. However, these calculations did not take into account internal structures, or the different densities that the NBMs could encounter within the spheroid. By using Fluorescence Recovery After Photobleaching (FRAP), and Fluorescence Correlation Spectroscopy (FCS), two powerful fluorescence techniques, the mobility of the NBMs, and the diffusion coefficient of the NBMs can be accurately determined. FRAP allows for the study of the

mobility of the NBMs within the spheroid. An area within the spheroid is exposed to a high intensity laser, photobleaching the NBMs. The area is then repeatedly imaged until the fluorescence has recovered, or the NBMs have repopulated the area. FCS measures the fluctuations in fluorescence intensity of the NBMs that pass through a confocal volume over time. By using FCS, the diffusion coefficient of the NBMs can be accurately determined. Using the FRAP and FCS information, in combination with the aforementioned diffusion calculations, a numerical model could be explored to map the diffusion of the NBMs into the spheroid, and aid in the design of future NBMs. Lipid and polymer based nanoparticles have been used as drug delivery systems [181]. By loading the nanoparticles with chemotherapeutic drugs, NIRF could be used to locate the lipid nanoparticles within tumours to ensure drug delivery.

References

- [1] R. and M. ltd, Global Nanotechnology Market (by Component and Applications), Funding & Investment, Patent Analysis and 27 Companies Profile & Recent Developments - Forecast to 2024, (2018). <https://www.researchandmarkets.com/reports/4520812/global-nanotechnology-market-by-component-and> (accessed February 6, 2023).
- [2] E. Inshakova, A. Inshakova, A. Goncharov, Engineered nanomaterials for energy sector: market trends, modern applications and future prospects, IOP Conf. Ser. Mater. Sci. Eng. 971 (2020) 032031. <https://doi.org/10.1088/1757-899X/971/3/032031>.
- [3] M. Nasrollahzadeh, S.M. Sajadi, M. Sajjadi, Z. Issaabadi, Chapter 4 - Applications of Nanotechnology in Daily Life, in: M. Nasrollahzadeh, S.M. Sajadi, M. Sajjadi, Z. Issaabadi, M. Atarod (Eds.), Interface Sci. Technol., Elsevier, 2019: pp. 113–143. <https://doi.org/10.1016/B978-0-12-813586-0.00004-3>.
- [4] M. De, P.S. Ghosh, V.M. Rotello, Applications of Nanoparticles in Biology, Adv. Mater. 20 (2008) 4225–4241. <https://doi.org/10.1002/adma.200703183>.
- [5] J. Jeevanandam, A. Barhoum, Y.S. Chan, A. Dufresne, M.K. Danquah, Review on nanoparticles and nanostructured materials: history, sources, toxicity and regulations, Beilstein J. Nanotechnol. 9 (2018) 1050–1074. <https://doi.org/10.3762/bjnano.9.98>.
- [6] A. Ali, A. Mitra, B. Aïssa, Metamaterials and Metasurfaces: A Review from the Perspectives of Materials, Mechanisms and Advanced Metadevices, Nanomaterials. 12 (2022) 1027. <https://doi.org/10.3390/nano12061027>.
- [7] C.L. Holloway, E.F. Kuester, J.A. Gordon, J. O'Hara, J. Booth, D.R. Smith, An Overview of the Theory and Applications of Metasurfaces: The Two-Dimensional Equivalents of Metamaterials, IEEE Antennas Propag. Mag. 54 (2012) 10–35. <https://doi.org/10.1109/MAP.2012.6230714>.
- [8] H.H. Hsiao, C.H. Chu, D.P. Tsai, Fundamentals and Applications of Metasurfaces, Small Methods. 1 (2017) 1600064. <https://doi.org/10.1002/smt.201600064>.
- [9] L. La Spada, Metasurfaces for Advanced Sensing and Diagnostics, Sensors. 19 (2019) 355. <https://doi.org/10.3390/s19020355>.

- [10] Y. Sun, G. Ren, S. Han, X. Zhang, C. Liu, Z. Li, D. Fu, W. Guo, Improving light harvesting and charge extraction of polymer solar cells upon buffer layer doping, *Sol. Energy*. 202 (2020) 80–85. <https://doi.org/10.1016/j.solener.2020.03.105>.
- [11] N. Yu, F. Capasso, Optical Metasurfaces and Prospect of Their Applications Including Fiber Optics, *J. Light. Technol.* 33 (2015) 2344–2358. <https://doi.org/10.1109/JLT.2015.2404860>.
- [12] V.C. Su, C.H. Chu, G. Sun, D.P. Tsai, Advances in optical metasurfaces: fabrication and applications [Invited], *Opt. Express*. 26 (2018) 13148–13182. <https://doi.org/10.1364/OE.26.013148>.
- [13] W. Bogaerts, V. Wiaux, D. Taillaert, S. Beckx, B. Luyssaert, P. Bienstman, R. Baets, Fabrication of photonic crystals in silicon-on-insulator using 248-nm deep UV lithography, *IEEE J. Sel. Top. Quantum Electron.* 8 (2002) 928–934. <https://doi.org/10.1109/JSTQE.2002.800845>.
- [14] L.A. Giannuzzi, F.A. Stevie, A review of focused ion beam milling techniques for TEM specimen preparation, *Micron*. 30 (1999) 197–204. [https://doi.org/10.1016/S0968-4328\(99\)00005-0](https://doi.org/10.1016/S0968-4328(99)00005-0).
- [15] H. Morimoto, Y. Sasaki, K. Saitoh, Y. Watakabe, T. Kato, Focused ion beam lithography and its application to submicron devices, *Microelectron. Eng.* 4 (1986) 163–179. [https://doi.org/10.1016/0167-9317\(86\)90009-2](https://doi.org/10.1016/0167-9317(86)90009-2).
- [16] A.A. Tseng, A. Notargiacomo, T.P. Chen, Nanofabrication by scanning probe microscope lithography: A review, *J. Vac. Sci. Technol. B Microelectron. Nanometer Struct. Process. Meas. Phenom.* 23 (2005) 877–894. <https://doi.org/10.1116/1.1926293>.
- [17] J. Fischer, M. Wegener, Three-dimensional optical laser lithography beyond the diffraction limit, *Laser Photonics Rev.* 7 (2013) 22–44. <https://doi.org/10.1002/lpor.201100046>.
- [18] S.Y. Chou, Nanoimprint lithography, US5772905A, 1998. <https://patents.google.com/patent/US5772905A/en> (accessed August 7, 2018).
- [19] Y. Zou, L. Moreel, H. Lin, J. Zhou, L. Li, S. Danto, J.D. Musgraves, E. Koontz, K. Richardson, K.D. Dobson, Solution Processing and Resist-Free Nanoimprint Fabrication of Thin Film Chalcogenide Glass Devices: Inorganic–Organic Hybrid Photonic Integration, *Adv. Opt. Mater.* 2 (2014) 759–764.

- [20] R. Tao, H. Ning, J. Chen, J. Zou, Z. Fang, C. Yang, Y. Zhou, J. Zhang, R. Yao, J. Peng, Inkjet Printed Electrodes in Thin Film Transistors, *IEEE J. Electron Devices Soc.* 6 (2018) 774–790. <https://doi.org/10.1109/JEDS.2018.2852288>.
- [21] J.S. Kang, H.S. Kim, J. Ryu, H. Thomas Hahn, S. Jang, J.W. Joung, Inkjet printed electronics using copper nanoparticle ink, *J. Mater. Sci. Mater. Electron.* 21 (2010) 1213–1220. <https://doi.org/10.1007/s10854-009-0049-3>.
- [22] A. Kamyshny, M. Ben-Moshe, S. Aviezer, S. Magdassi, Ink-Jet Printing of Metallic Nanoparticles and Microemulsions, *Macromol. Rapid Commun.* 26 (2005) 281–288. <https://doi.org/10.1002/marc.200400522>.
- [23] E.-U. Kim, K.-J. Baeg, Y.-Y. Noh, D.-Y. Kim, T. Lee, I. Park, G.-Y. Jung, Templated assembly of metal nanoparticles in nanoimprinted patterns for metal nanowire fabrication, *Nanotechnology.* 20 (2009) 355302. <https://doi.org/10.1088/0957-4484/20/35/355302>.
- [24] R. Wakamatsu, J. Taniguchi, Nanoscale metal pattern-transfer technique using silver ink, *Microelectron. Eng.* 123 (2014) 94–99. <https://doi.org/10.1016/j.mee.2014.05.021>.
- [25] K. Rajan, I. Roppolo, A. Chiappone, S. Bocchini, D. Perrone, A. Chiolerio, Silver nanoparticle ink technology: state of the art, *Nanotechnol. Sci. Appl.* 9 (2016) 1–13. <https://doi.org/10.2147/NSA.S68080>.
- [26] S. Jeong, H.C. Song, W.W. Lee, Y. Choi, B.H. Ryu, Preparation of aqueous Ag Ink with long-term dispersion stability and its inkjet printing for fabricating conductive tracks on a polyimide film, *J. Appl. Phys.* 108 (2010) 102805. <https://doi.org/10.1063/1.3511686>.
- [27] S.K. Park, Y.-H. Kim, J.-I. Han, High-resolution patterned nanoparticulate Ag electrodes toward all printed organic thin film transistors, *Org. Electron.* 10 (2009) 1102–1108. <https://doi.org/10.1016/j.orgel.2009.05.024>.
- [28] H.W. Tan, J. An, C.K. Chua, T. Tran, Metallic Nanoparticle Inks for 3D Printing of Electronics, *Adv. Electron. Mater.* 5 (2019) 1800831. <https://doi.org/10.1002/aelm.201800831>.
- [29] M. Singh, H.M. Haverinen, P. Dhagat, G.E. Jabbour, Inkjet Printing-Process and Its Applications, *Adv. Mater.* 22 (2010) 673–685. <https://doi.org/10.1002/adma.200901141>.

- [30] A. Kamyshny, S. Magdassi, Conductive nanomaterials for 2D and 3D printed flexible electronics, *Chem. Soc. Rev.* 48 (2019) 1712–1740. <https://doi.org/10.1039/C8CS00738A>.
- [31] N. Tsai, B. Lee, A. Kim, R. Yang, R. Pan, D.-K. Lee, E.K. Chow, D. Ho, Nanomedicine for Global Health, *SLAS Technol.* 19 (2014) 511–516. <https://doi.org/10.1177/2211068214538263>.
- [32] J. Cancino-Bernardi, V.S. Marangoni, V. Zucolotto, Nanomedicine, in: *Nanosci. Its Appl.*, Elsevier, 2017: pp. 71–92. <https://doi.org/10.1016/B978-0-323-49780-0.00003-X>.
- [33] J.A. Barreto, W. O'Malley, M. Kubeil, B. Graham, H. Stephan, L. Spiccia, Nanomaterials: Applications in Cancer Imaging and Therapy, *Adv. Mater.* 23 (2011) H18–H40. <https://doi.org/10.1002/adma.201100140>.
- [34] M.A. Krishnan, K. Yadav, P. Roach, V. Chelvam, A targeted near-infrared nanoprobes for deep-tissue penetration and imaging of prostate cancer, *Biomater. Sci.* 9 (2021) 2295–2312. <https://doi.org/10.1039/D0BM01970D>.
- [35] X. Dang, N.M. Bardhan, J. Qi, L. Gu, N.A. Eze, C.-W. Lin, S. Kataria, P.T. Hammond, A.M. Belcher, Deep-tissue optical imaging of near cellular-sized features, *Sci. Rep.* 9 (2019) 3873. <https://doi.org/10.1038/s41598-019-39502-w>.
- [36] R. Iqbal, S. Khan, H.M. Ali, M. Khan, S. Wahab, T. Khan, Application of nanomaterials against SARS-CoV-2: An emphasis on their usefulness against emerging variants of concern, *Front. Nanotechnol.* 4 (2022). <https://www.frontiersin.org/articles/10.3389/fnano.2022.1060756> (accessed February 6, 2023).
- [37] I. Khan, K. Saeed, I. Khan, Nanoparticles: Properties, applications and toxicities, *Arab. J. Chem.* 12 (2019) 908–931. <https://doi.org/10.1016/j.arabjc.2017.05.011>.
- [38] O. Salata, Applications of nanoparticles in biology and medicine, *J. Nanobiotechnology.* 2 (2004) 3. <https://doi.org/10.1186/1477-3155-2-3>.
- [39] H. Page, P. Flood, E.G. Reynaud, Three-dimensional tissue cultures: current trends and beyond, *Cell Tissue Res.* 352 (2013) 123–131. <https://doi.org/10.1007/s00441-012-1441-5>.
- [40] J. Lee, G.D. Lilly, R.C. Doty, P. Podsiadlo, N.A. Kotov, In vitro Toxicity Testing of Nanoparticles in 3D Cell Culture, *Small.* 5 (2009) 1213–1221. <https://doi.org/10.1002/smll.200801788>.

- [41] J. Lee, M.J. Cuddihy, N.A. Kotov, Three-Dimensional Cell Culture Matrices: State of the Art, *Tissue Eng. Part B Rev.* 14 (2008) 61–86. <https://doi.org/10.1089/teb.2007.0150>.
- [42] C.M. Sayes, K.L. Reed, D.B. Warheit, Assessing Toxicity of Fine and Nanoparticles: Comparing In Vitro Measurements to In Vivo Pulmonary Toxicity Profiles, *Toxicol. Sci.* 97 (2007) 163–180. <https://doi.org/10.1093/toxsci/kfm018>.
- [43] K. Tanner, M.M. Gottesman, Beyond 3D culture models of cancer, *Sci. Transl. Med.* 7 (2015) 283ps9-283ps9. <https://doi.org/10.1126/scitranslmed.3009367>.
- [44] C.M. Sayes, A.A. Marchione, K.L. Reed, D.B. Warheit, Comparative Pulmonary Toxicity Assessments of C60 Water Suspensions in Rats: Few Differences in Fullerene Toxicity in Vivo in Contrast to in Vitro Profiles, *Nano Lett.* 7 (2007) 2399–2406. <https://doi.org/10.1021/nl0710710>.
- [45] Y. Zhang, W. Chen, J. Zhang, J. Liu, G. Chen, C. Pope, In Vitro and In Vivo Toxicity of CdTe Nanoparticles, *J. Nanosci. Nanotechnol.* 7 (2007) 497–503. <https://doi.org/10.1166/jnn.2007.125>.
- [46] J.S. Kim, T.-J. Yoon, K.N. Yu, B.G. Kim, S.J. Park, H.W. Kim, K.H. Lee, S.B. Park, J.-K. Lee, M.H. Cho, Toxicity and Tissue Distribution of Magnetic Nanoparticles in Mice, *Toxicol. Sci.* 89 (2006) 338–347. <https://doi.org/10.1093/toxsci/kfj027>.
- [47] P. Wick, S. Grafmueller, A. Petri-Fink, B. Rothen-Rutishauser, Advanced human in vitro models to assess metal oxide nanoparticle-cell interactions, *MRS Bull.* 39 (2014) 984–989. <https://doi.org/10.1557/mrs.2014.219>.
- [48] N. Alépée, A. Bahinski, M. Daneshian, B. De Wever, E. Fritsche, A. Goldberg, J. Hansmann, T. Hartung, J. Haycock, H.T. Hogberg, L. Hoelting, J.M. Kelm, S. Kadereit, E. McVey, R. Landsiedel, M. Leist, M. Lübberstedt, F. Noor, C. Pellevoisin, D. Petersohn, U. Pfannenbecker, K. Reisinger, T. Ramirez, B. Rothen-Rutishauser, M. Schäfer-Korting, K. Zeilinger, M.-G. Zurich, State-of-the-art of 3D cultures (organs-on-a-chip) in safety testing and pathophysiology, *ALTEX.* 31 (2014) 441–477.
- [49] M.A. Saifi, W. Khan, C. Godugu, Cytotoxicity of Nanomaterials: Using Nanotoxicology to Address the Safety Concerns of Nanoparticles, *Pharm. Nanotechnol.* 6 (2018) 3–16. <https://doi.org/10.2174/2211738505666171023152928>.

- [50] I. M6, I.J. Sabino, D. de Melo-Diogo, R. Lima-Sousa, C.G. Alves, I.J. Correia, The importance of spheroids in analyzing nanomedicine efficacy, *Nanomed.* 15 (2020) 1513–1525. <https://doi.org/10.2217/nnm-2020-0054>.
- [51] E. Elje, E. Mariussen, O.H. Moriones, N.G. Bast6s, V. Puentes, Y. Kohl, M. Dusinska, E. Rund6n-Pran, Hepato(Geno)Toxicity Assessment of Nanoparticles in a HepG2 Liver Spheroid Model, *Nanomaterials.* 10 (2020) 545. <https://doi.org/10.3390/nano10030545>.
- [52] X. Zhang, T. Jiang, D. Chen, Q. Wang, L.W. Zhang, Three-dimensional liver models: state of the art and their application for hepatotoxicity evaluation, *Crit. Rev. Toxicol.* 50 (2020) 279–309. <https://doi.org/10.1080/10408444.2020.1756219>.
- [53] M. Dubiak-Szepietowska, A. Karczmarczyk, M. J6nsson-Niedzi6łka, T. Winckler, K.-H. Feller, Development of complex-shaped liver multicellular spheroids as a human-based model for nanoparticle toxicity assessment in vitro, *Toxicol. Appl. Pharmacol.* 294 (2016) 78–85. <https://doi.org/10.1016/j.taap.2016.01.016>.
- [54] E. Blanco, H. Shen, M. Ferrari, Principles of nanoparticle design for overcoming biological barriers to drug delivery, *Nat. Biotechnol.* 33 (2015) 941–951. <https://doi.org/10.1038/nbt.3330>.
- [55] J. Wolfram, M. Zhu, Y. Yang, J. Shen, E. Gentile, D. Paolino, M. Fresta, G. Nie, C. Chen, H. Shen, M. Ferrari, Y. Zhao, Safety of Nanoparticles in Medicine, *Curr. Drug Targets.* (2014). <https://doi.org/10.2174/1389450115666140804124808>.
- [56] S.D. Collins, G. Yuen, T. Tu, M.A. Budzinska, K.J. Spring, K. Bryant, N.A. Shackel, In vitro models of the liver: disease modeling, drug discovery and clinical applications, 2019. <https://doi.org/10.15586/hepatocellularcarcinoma.2019.ch3>.
- [57] S.S. Bale, L. Verneti, N. Senutovitch, R. Jindal, M. Hegde, A. Gough, W.J. McCarty, A. Bakan, A. Bhushan, T.Y. Shun, I. Golberg, R. DeBiasio, O.B. Usta, D.L. Taylor, M.L. Yarmush, In vitro platforms for evaluating liver toxicity, *Exp. Biol. Med.* 239 (2014) 1180–1191. <https://doi.org/10.1177/1535370214531872>.
- [58] K. Bischoff, M. Mukai, S.K. Ramaiah, Chapter 15 - Liver Toxicity, in: R.C. Gupta (Ed.), *Vet. Toxicol. Third Ed.*, Academic Press, 2018: pp. 239–257. <https://doi.org/10.1016/B978-0-12-811410-0.00015-5>.

- [59] D. Neshev, I. Aharonovich, Optical metasurfaces: new generation building blocks for multi-functional optics, *Light Sci. Appl.* 7 (2018) 58. <https://doi.org/10.1038/s41377-018-0058-1>.
- [60] N. Yu, F. Capasso, Flat optics with designer metasurfaces, *Nat. Mater.* 13 (2014) 139–150. <https://doi.org/10.1038/nmat3839>.
- [61] S.S. Bukhari, J. Vardaxoglou, W. Whittow, A Metasurfaces Review: Definitions and Applications, *Appl. Sci.* 9 (2019) 2727. <https://doi.org/10.3390/app9132727>.
- [62] G.-Y. Lee, G. Yoon, S.-Y. Lee, H. Yun, J. Cho, K. Lee, H. Kim, J. Rho, B. Lee, Complete amplitude and phase control of light using broadband holographic metasurfaces, *Nanoscale.* 10 (2018) 4237–4245. <https://doi.org/10.1039/C7NR07154J>.
- [63] E. Almeida, G. Shalem, Y. Prior, Subwavelength nonlinear phase control and anomalous phase matching in plasmonic metasurfaces, *Nat. Commun.* 7 (2016) 10367. <https://doi.org/10.1038/ncomms10367>.
- [64] I.P. Radko, V.S. Volkov, J. Beermann, A.B. Evlyukhin, T. Søndergaard, A. Boltasseva, S.I. Bozhevolnyi, Plasmonic metasurfaces for waveguiding and field enhancement, *Laser Photonics Rev.* 3 (2009) 575–590. <https://doi.org/10.1002/lpor.200810071>.
- [65] C.E. Petoukhoff, D.M. O’Carroll, Absorption-induced scattering and surface plasmon out-coupling from absorber-coated plasmonic metasurfaces, *Nat. Commun.* 6 (2015) 7899.
- [66] Z. Shen, D.M. O’Carroll, Nanoporous Silver Thin Films: Multifunctional Platforms for Influencing Chain Morphology and Optical Properties of Conjugated Polymers, *Adv. Funct. Mater.* 25 (2015) 3302–3313. <https://doi.org/10.1002/adfm.201500456>.
- [67] Z. Cheng, N. Javed, D.M. O’Carroll, Optical and Electrical Properties of Organic Semiconductor Thin Films on Aperiodic Plasmonic Metasurfaces, *ACS Appl. Mater. Interfaces.* 12 (2020) 35579–35587. <https://doi.org/10.1021/acsami.0c07099>.
- [68] J. Zaumseil, Recent Developments and Novel Applications of Thin Film, Light-Emitting Transistors, *Adv. Funct. Mater.* 30 (2020) 1905269. <https://doi.org/10.1002/adfm.201905269>.
- [69] A. Peter Amalathas, M.M. Alkaisi, Nanostructures for Light Trapping in Thin Film Solar Cells, *Micromachines.* 10 (2019) 619. <https://doi.org/10.3390/mi10090619>.

- [70] A. Tamang, A. Hongsingthong, V. Jovanov, P. Sichanugrist, B.A. Khan, R. Dewan, M. Konagai, D. Knipp, Enhanced photon management in silicon thin film solar cells with different front and back interface texture, *Sci. Rep.* 6 (2016) 29639. <https://doi.org/10.1038/srep29639>.
- [71] J.-H. Choi, S.-W. Lee, J.-H. Jeong, D.-G. Choi, E.-S. Lee, Direct imprint of conductive silver patterns using nanosilver particles and UV curable resin, *Microelectron. Eng.* 86 (2009) 622–627. <https://doi.org/10.1016/j.mee.2008.12.080>.
- [72] G. Cardoso, F. Hamouda, B. Dagens, Improved PDMS mold fabrication by direct etch with nanosphere self-assembly mask for Soft UV-NIL subwavelength metasurfaces fabrication, *Microelectron. Eng.* 258 (2022) 111755. <https://doi.org/10.1016/j.mee.2022.111755>.
- [73] S. Sardar, P. Wojcik, E.S. H. Kang, R. Shanker, M. P. Jonsson, Structural coloration by inkjet-printing of optical microcavities and metasurfaces, *J. Mater. Chem. C* 7 (2019) 8698–8704. <https://doi.org/10.1039/C9TC02796C>.
- [74] N. Kooy, K. Mohamed, L.T. Pin, O.S. Guan, A review of roll-to-roll nanoimprint lithography, *Nanoscale Res. Lett.* 9 (2014) 320.
- [75] H. Lim, K. Choi, G. Kim, S. Lee, H. Park, J. Ryu, S. Jung, J. Lee, Roll-to-roll nanoimprint lithography for patterning on a large-area substrate roll, *Microelectron. Eng.* 123 (2014) 18–22. <https://doi.org/10.1016/j.mee.2014.03.037>.
- [76] D. Ito, K. Masuko, B.A. Weintraub, L.C. McKenzie, J.E. Hutchison, Convenient preparation of ITO nanoparticles inks for transparent conductive thin films, *J. Nanoparticle Res.* 14 (2012) 1274. <https://doi.org/10.1007/s11051-012-1274-x>.
- [77] S.Y. Chou, P.R. Krauss, P.J. Renstrom, Nanoimprint lithography, *J. Vac. Sci. Technol. B Microelectron. Nanometer Struct. Process. Meas. Phenom.* 14 (1996) 4129–4133.
- [78] D.K. Oh, T. Lee, B. Ko, T. Badloe, J.G. Ok, J. Rho, Nanoimprint lithography for high-throughput fabrication of metasurfaces, *Front. Optoelectron.* 14 (2021) 229–251. <https://doi.org/10.1007/s12200-021-1121-8>.
- [79] H. Schiff, Nanoimprint lithography: An old story in modern times? A review, *J. Vac. Sci. Technol. B Microelectron. Nanometer Struct. Process. Meas. Phenom.* 26 (2008) 458–480.

- [80] L.J. Guo, Nanoimprint lithography: methods and material requirements, *Adv. Mater.* 19 (2007) 495–513.
- [81] B.D. Gates, Q. Xu, M. Stewart, D. Ryan, C.G. Willson, G.M. Whitesides, New Approaches to Nanofabrication: Molding, Printing, and Other Techniques, *Chem. Rev.* 105 (2005) 1171–1196. <https://doi.org/10.1021/cr030076o>.
- [82] S.H. Ko, I. Park, H. Pan, C.P. Grigoropoulos, A.P. Pisano, C.K. Luscombe, J.M.J. Fréchet, Direct Nanoimprinting of Metal Nanoparticles for Nanoscale Electronics Fabrication, *Nano Lett.* 7 (2007) 1869–1877. <https://doi.org/10.1021/nl070333v>.
- [83] A.R. Shafiq, A. Abdul Aziz, B. Mehrdel, Nanoparticle Optical Properties: Size Dependence of a Single Gold Spherical Nanoparticle, *J. Phys. Conf. Ser.* 1083 (2018) 012040. <https://doi.org/10.1088/1742-6596/1083/1/012040>.
- [84] C.M. Carter, J. Cho, A. Glanzer, N. Kamcev, D.M. O'Carroll, Cost, energy and emissions assessment of organic polymer light-emitting device architectures, *J. Clean. Prod.* 137 (2016) 1418–1431. <https://doi.org/10.1016/j.jclepro.2016.07.186>.
- [85] C. Nemes, D. Vijapurapu, C. Petoukhoff, G. Cheung, D. O'Carroll, Absorption and scattering effects by silver nanoparticles near the interface of organic/inorganic semiconductor tandem films, *J. Nanoparticle Res.* 15 (2013) 1–13. <https://doi.org/10.1007/s11051-013-1801-4>.
- [86] H.-C. Wang, K. Achouri, O.J.F. Martin, Robustness Analysis of Metasurfaces: Perfect Structures Are Not Always the Best, *ACS Photonics.* 9 (2022) 2438–2447. <https://doi.org/10.1021/acsp Photonics.2c00563>.
- [87] S. Sun, Z. Zhou, C. Zhang, Y. Gao, Z. Duan, S. Xiao, Q. Song, All-Dielectric Full-Color Printing with TiO₂ Metasurfaces, *ACS Nano.* 11 (2017) 4445–4452. <https://doi.org/10.1021/acsnano.7b00415>.
- [88] M.V. Rybin, K.B. Samusev, S.Y. Lukashenko, Y.S. Kivshar, M.F. Limonov, Transition from two-dimensional photonic crystals to dielectric metasurfaces in the optical diffraction with a fine structure, *Sci. Rep.* 6 (2016) 30773. <https://doi.org/10.1038/srep30773>.
- [89] M. Kato, T. Ito, Y. Aoyama, K. Sawa, T. Kaneko, N. Kawase, H. Jinnai, Three-dimensional structural analysis of a block copolymer by scanning electron microscopy combined with a focused ion beam, *J. Polym. Sci. Part B Polym. Phys.* 45 (2007) 677–683. <https://doi.org/10.1002/polb.21088>.

- [90] J. Cazaux, From the physics of secondary electron emission to image contrasts in scanning electron microscopy, *J. Electron Microsc. (Tokyo)*. 61 (2012) 261–284. <https://doi.org/10.1093/jmicro/dfs048>.
- [91] G. Palermo, M. Rippa, Y. Conti, A. Vestri, R. Castagna, G. Fusco, E. Suffredini, J. Zhou, J. Zyss, A. De Luca, L. Petti, Plasmonic Metasurfaces Based on Pyramidal Nanoholes for High-Efficiency SERS Biosensing, *ACS Appl. Mater. Interfaces*. 13 (2021) 43715–43725. <https://doi.org/10.1021/acsami.1c12525>.
- [92] P.J. James, M. Antognozzi, J. Tamayo, T.J. McMaster, J.M. Newton, M.J. Miles, Interpretation of Contrast in Tapping Mode AFM and Shear Force Microscopy. A Study of Nafion, *Langmuir*. 17 (2001) 349–360. <https://doi.org/10.1021/la000332h>.
- [93] S.N. Magonov, V. Elings, M.-H. Whangbo, Phase imaging and stiffness in tapping-mode atomic force microscopy, *Surf. Sci.* 375 (1997) L385–L391. [https://doi.org/10.1016/S0039-6028\(96\)01591-9](https://doi.org/10.1016/S0039-6028(96)01591-9).
- [94] X. Wang, J. Jian, S. Diaz-Amaya, C. E. Kumah, P. Lu, J. Huang, D. Gen Lim, V. G. Pol, J. P. Youngblood, A. Boltasseva, L. A. Stanciu, D. M. O’Carroll, X. Zhang, H. Wang, Hybrid plasmonic Au–TiN vertically aligned nanocomposites: a nanoscale platform towards tunable optical sensing, *Nanoscale Adv.* (2019). <https://pubs.rsc.org/en/content/articlelanding/2019/na/c8na00306h> (accessed February 1, 2019).
- [95] J.M. Pitarke, V.M. Silkin, E.V. Chulkov, P.M. Echenique, Theory of surface plasmons and surface-plasmon polaritons, *Rep. Prog. Phys.* 70 (2007) 1–87. <https://doi.org/10.1088/0034-4885/70/1/R01>.
- [96] H. Raether, *Surface Plasmons on Smooth and Rough Surfaces and on Gratings*, Springer Berlin Heidelberg, Berlin, Heidelberg, 1988. <https://doi.org/10.1007/BFb0048317>.
- [97] L. Yang, L. Zhang, T.J. Webster, Nanobiomaterials: State of the Art and Future Trends, *Adv. Eng. Mater.* 13 (2011) B197–B217. <https://doi.org/10.1002/adem.201080140>.
- [98] M. Goldberg, R. Langer, X. Jia, Nanostructured materials for applications in drug delivery and tissue engineering, *J. Biomater. Sci. Polym. Ed.* 18 (2007) 241–268. <https://doi.org/10.1163/156856207779996931>.

- [99] L. Yang, T.J. Webster, Nanotechnology controlled drug delivery for treating bone diseases, *Expert Opin. Drug Deliv.* 6 (2009) 851–864. <https://doi.org/10.1517/17425240903044935>.
- [100] P.A. McCarron, W.M. Marouf, R.F. Donnelly, C. Scott, Enhanced surface attachment of protein-type targeting ligands to poly(lactide-co-glycolide) nanoparticles using variable expression of polymeric acid functionality, *J. Biomed. Mater. Res. A.* 87A (2008) 873–884. <https://doi.org/10.1002/jbm.a.31835>.
- [101] D.P. Cormode, T. Skajaa, Z.A. Fayad, W.J.M. Mulder, Nanotechnology in Medical Imaging, *Arterioscler. Thromb. Vasc. Biol.* 29 (2009) 992–1000. <https://doi.org/10.1161/ATVBAHA.108.165506>.
- [102] European Commission Revised the Definition of Nanomaterials - Regulatory News - Chemicals - CIRS Group, (2022). <https://www.cirs-group.com/en/chemicals/european-commission-revised-the-definition-of-nanomaterials> (accessed March 2, 2023).
- [103] S. Bibi, R. Kaur, M. Henriksen-Lacey, S.E. McNeil, J. Wilkhu, E. Lattmann, D. Christensen, A.R. Mohammed, Y. Perrie, Microscopy imaging of liposomes: From coverslips to environmental SEM, *Int. J. Pharm.* 417 (2011) 138–150. <https://doi.org/10.1016/j.ijpharm.2010.12.021>.
- [104] C.M. Maguire, M. Rösslein, P. Wick, A. Prina-Mello, Characterisation of particles in solution – a perspective on light scattering and comparative technologies, *Sci. Technol. Adv. Mater.* 19 (2018) 732–745. <https://doi.org/10.1080/14686996.2018.1517587>.
- [105] A. Tchoryk, V. Taresco, R.H. Argent, M. Ashford, P.R. Gellert, S. Stolnik, A. Grabowska, M.C. Garnett, Penetration and Uptake of Nanoparticles in 3D Tumor Spheroids, *Bioconjug. Chem.* 30 (2019) 1371–1384. <https://doi.org/10.1021/acs.bioconjchem.9b00136>.
- [106] K. Juarez-Moreno, D. Chávez-García, G. Hirata, R. Vazquez-Duhalt, Monolayer (2D) or spheroids (3D) cell cultures for nanotoxicological studies? Comparison of cytotoxicity and cell internalization of nanoparticles, *Toxicol. In Vitro.* 85 (2022) 105461. <https://doi.org/10.1016/j.tiv.2022.105461>.
- [107] A. Adan, G. Alizada, Y. Kiraz, Y. Baran, A. Nalbant, Flow cytometry: basic principles and applications, *Crit. Rev. Biotechnol.* 37 (2017) 163–176. <https://doi.org/10.3109/07388551.2015.1128876>.

- [108] M. Kapałczyńska, T. Kolenda, W. Przybyła, M. Zajączkowska, A. Teresiak, V. Filas, M. Ibbs, R. Bliźniak, \Lukasz \Luczewski, K. Lamperska, 2D and 3D cell cultures—a comparison of different types of cancer cell cultures, *Arch. Med. Sci.* 14 (2018) 910–919.
- [109] J.B. Kim, Three-dimensional tissue culture models in cancer biology, *Semin. Cancer Biol.* 15 (2005) 365–377. <https://doi.org/10.1016/j.semcancer.2005.05.002>.
- [110] M. Wartenberg, H. Acker, Quantitative recording of vitality patterns in living multicellular spheroids by confocal microscopy, *Micron.* 26 (1995) 395–404. [https://doi.org/10.1016/0968-4328\(95\)00009-7](https://doi.org/10.1016/0968-4328(95)00009-7).
- [111] L.A. Gurski, N.J. Petrelli, X. Jia, M.C. Farach-Carson, 3D Matrices for Anti-Cancer Drug Testing and Development, *Oncol. Issues.* 25 (2010) 20–25. <https://doi.org/10.1080/10463356.2010.11883480>.
- [112] J.W. Lichtman, J.-A. Conchello, Fluorescence microscopy, *Nat. Methods.* 2 (2005) 910–919. <https://doi.org/10.1038/nmeth817>.
- [113] N.S. Claxton, T.J. Fellers, M.W. Davidson, Laser Scanning Confocal Microscopy, *Encycl. Med. Devices Instrum.* 21(1) (2006) 1–37.
- [114] E. Elje, M. Hesler, E. Rundén-Pran, P. Mann, E. Mariussen, S. Wagner, M. Dusinska, Y. Kohl, The comet assay applied to HepG2 liver spheroids, *Mutat. Res. Toxicol. Environ. Mutagen.* 845 (2019) 403033. <https://doi.org/10.1016/j.mrgentox.2019.03.006>.
- [115] E. Leary, C. Rhee, B.T. Wilks, J.R. Morgan, Quantitative Live-cell Confocal Imaging of 3D Spheroids in a High Throughput Format, *SLAS Technol.* 23 (2018) 231–242. <https://doi.org/10.1177/2472630318756058>.
- [116] S. Hiemstra, S.C. Ramaiahgari, S. Wink, G. Callegaro, M. Coonen, J. Meerman, D. Jennen, K. van den Nieuwendijk, A. Dankers, J. Snoeys, H. de Bont, L. Price, B. van de Water, High-throughput confocal imaging of differentiated 3D liver-like spheroid cellular stress response reporters for identification of drug-induced liver injury liability, *Arch. Toxicol.* 93 (2019) 2895–2911. <https://doi.org/10.1007/s00204-019-02552-0>.
- [117] S.M. Sagnella, H. Duong, A. MacMillan, C. Boyer, R. Whan, J.A. McCarroll, T.P. Davis, M. Kavallaris, Dextran-Based Doxorubicin Nanocarriers with Improved Tumor Penetration, *Biomacromolecules.* 15 (2014) 262–275. <https://doi.org/10.1021/bm401526d>.

- [118] J.S. Basuki, H.T.T. Duong, A. Macmillan, R.B. Erlich, L. Esser, M.C. Akerfeldt, R.M. Whan, M. Kavallaris, C. Boyer, T.P. Davis, Using Fluorescence Lifetime Imaging Microscopy to Monitor Theranostic Nanoparticle Uptake and Intracellular Doxorubicin Release, *ACS Nano*. 7 (2013) 10175–10189. <https://doi.org/10.1021/nn404407g>.
- [119] Z. Peng, K. Nie, Y. Song, H. Liu, Y. Zhou, Y. Yuan, D. Chen, X. Peng, W. Yan, J. Song, J. Qu, Monitoring the Cellular Delivery of Doxorubicin–Cu Complexes in Cells by Fluorescence Lifetime Imaging Microscopy, *J. Phys. Chem. A*. 124 (2020) 4235–4240. <https://doi.org/10.1021/acs.jpca.0c00182>.
- [120] D.B. Hall, P. Underhill, J.M. Torkelson, Spin coating of thin and ultrathin polymer films, *Polym. Eng. Sci.* 38 (1998) 2039–2045. <https://doi.org/10.1002/pen.10373>.
- [121] C.M. Carter, Device and metasurface designs for next-generation blue-emitting organic LEDs: cost, sustainability, efficiency, and stability, Rutgers University - School of Graduate Studies, 2018. <https://doi.org/10.7282/T33N26MW>.
- [122] H. Kang, J. Lee, J. Park, H.H. Lee, An improved method of preparing composite poly(dimethylsiloxane) moulds, *Nanotechnology*. 17 (2005) 197–200. <https://doi.org/10.1088/0957-4484/17/1/032>.
- [123] N. Lucas, S. Demming, A. Jordan, P. Sichler, S. Büttgenbach, An improved method for double-sided moulding of PDMS, *J. Micromechanics Microengineering*. 18 (2008) 075037.
- [124] Refractive index of Ag (Silver) - Johnson, *Refract. Index*. (2018). <https://refractiveindex.info/?shelf=main&book=Ag&page=Johnson> (accessed August 26, 2018).
- [125] G. Lévêque, O.J.F. Martin, Optimization of finite diffraction gratings for the excitation of surface plasmons, *J. Appl. Phys.* 100 (2006) 124301. <https://doi.org/10.1063/1.2401025>.
- [126] W.L. Barnes, A. Dereux, T.W. Ebbesen, Surface plasmon subwavelength optics, *Nature*. 424 (2003) 824.
- [127] J. Homola, I. Koudela, S.S. Yee, Surface plasmon resonance sensors based on diffraction gratings and prism couplers: sensitivity comparison, *Sens. Actuators B Chem.* 54 (1999) 16–24.

- [128] W. Zheng, S.-C. Wong, Electrical conductivity and dielectric properties of PMMA/expanded graphite composites, *Compos. Sci. Technol.* 63 (2003) 225–235. [https://doi.org/10.1016/S0266-3538\(02\)00201-4](https://doi.org/10.1016/S0266-3538(02)00201-4).
- [129] PMMA, (2020). <http://www.mit.edu/~6.777/matprops/pmma.htm> (accessed March 3, 2020).
- [130] Silver, dispersion product specification, (2018). https://www.sigmaaldrich.com/Graphics/COFAInfo/SigmaSAPQM/SPEC/73/736503/736503-BULK____ALDRICH_.pdf.
- [131] Silver, Ag, (2019). <https://www.matweb.com/search/DataSheet.aspx?MatGUID=63cbd043a31f4f739ddb7632c1443d33> (accessed March 6, 2019).
- [132] F. McGrath, J. Qian, K. Gwynne, C. Kumah, D. Daly, C. Hrelescu, X. Zhang, D.M. O'Carroll, A. Louise Bradley, Structural, optical, and electrical properties of silver gratings prepared by nanoimprint lithography of nanoparticle ink, *Appl. Surf. Sci.* 537 (2021) 147892. <https://doi.org/10.1016/j.apsusc.2020.147892>.
- [133] T. Jiang, H. Guo, Y.-N. Xia, Y. Liu, D. Chen, G. Pang, Y. Feng, H. Yu, Y. Wu, S. Zhang, Y. Wang, Y. Wang, H. Wen, L.W. Zhang, Hepatotoxicity of copper sulfide nanoparticles towards hepatocyte spheroids using a novel multi-concave agarose chip method, *Nanomed.* 16 (2021) 1487–1504. <https://doi.org/10.2217/nnm-2021-0011>.
- [134] T.D. Rane, A.M. Armani, Two-Photon Microscopy Analysis of Gold Nanoparticle Uptake in 3D Cell Spheroids, *PLOS ONE.* 11 (2016) e0167548. <https://doi.org/10.1371/journal.pone.0167548>.
- [135] R. Li, J. Liu, J. Ma, X. Sun, Y. Wang, J. Yan, Q. Yu, J. Diao, C. Yang, L.M. Reid, Y. Wang, Fibrinogen improves liver function via promoting cell aggregation and fibronectin assembly in hepatic spheroids, *Biomaterials.* 280 (2022) 121266. <https://doi.org/10.1016/j.biomaterials.2021.121266>.
- [136] I.S. Uroukov, M. Ma, L. Bull, W.M. Purcell, Electrophysiological measurements in three-dimensional in vivo-mimetic organotypic cell cultures: Preliminary studies with hen embryo brain spheroids, *Neurosci. Lett.* 404 (2006) 33–38. <https://doi.org/10.1016/j.neulet.2006.05.016>.
- [137] E. Bongaerts, T.S. Nawrot, T. Van Phee, M. Ameloot, H. Bove, Translocation of (ultra) fine particles and nanoparticles across the placenta; a systematic review

- on the evidence of in vitro, ex vivo, and in vivo studies, Part. *Fibre Toxicol.* 17 (20) 1–26. <https://doi.org/10.1186/s12989-020-00386-8>.
- [138] G. Bachler, S. Losert, Y. Umehara, N. von Goetz, L. Rodriguez-Lorenzo, A. Petri-Fink, B. Rothen-Rutishauser, K. Hungerbuehler, Translocation of gold nanoparticles across the lung epithelial tissue barrier: Combining in vitro and in silico methods to substitute in vivo experiments, Part. *Fibre Toxicol.* 12 (2015) 18. <https://doi.org/10.1186/s12989-015-0090-8>.
- [139] X. Dai, Z. Yue, M.E. Eccleston, J. Swartling, N.K.H. Slater, C.F. Kaminski, Fluorescence intensity and lifetime imaging of free and micellar-encapsulated doxorubicin in living cells, *Nanomedicine Nanotechnol. Biol. Med.* 4 (2008) 49–56. <https://doi.org/10.1016/j.nano.2007.12.002>.
- [140] G. Romero, Y. Qiu, R.A. Murray, S.E. Moya, Study of Intracellular Delivery of Doxorubicin from Poly(lactide- co -glycolide) Nanoparticles by Means of Fluorescence Lifetime Imaging and Confocal Raman Microscopy, *Macromol. Biosci.* 13 (2013) 234–241. <https://doi.org/10.1002/mabi.201200235>.
- [141] H.Y. Nam, S.M. Kwon, H. Chung, S.-Y. Lee, S.-H. Kwon, H. Jeon, Y. Kim, J.H. Park, J. Kim, S. Her, Y.-K. Oh, I.C. Kwon, K. Kim, S.Y. Jeong, Cellular uptake mechanism and intracellular fate of hydrophobically modified glycol chitosan nanoparticles, *J. Controlled Release.* 135 (2009) 259–267. <https://doi.org/10.1016/j.jconrel.2009.01.018>.
- [142] T. Pelras, H.T.T. Duong, B.J. Kim, B.S. Hawkett, M. Müllner, A ‘grafting from’ approach to polymer nanorods for pH-triggered intracellular drug delivery, *Polymer.* 112 (2017) 244–251. <https://doi.org/10.1016/j.polymer.2017.02.001>.
- [143] M.A. Tutty, Three-dimensional (3D) hepatic cell culture models to improve the clinical translation of nanobiomaterials (NBMs), Trinity College Dublin, 2021.
- [144] A. Sharma, M. Majdinasab, R. Khan, Z. Li, A. Hayat, J.L. Marty, Nanomaterials in fluorescence-based biosensors: Defining key roles, *Nano-Struct. Nano-Objects.* 27 (2021) 100774. <https://doi.org/10.1016/j.nanoso.2021.100774>.
- [145] I. Martinić, S.V. Eliseeva, S. Petoud, Near-infrared emitting probes for biological imaging: Organic fluorophores, quantum dots, fluorescent proteins, lanthanide(III) complexes and nanomaterials, *J. Lumin.* 189 (2017) 19–43. <https://doi.org/10.1016/j.jlumin.2016.09.058>.
- [146] A. Jacquart, M. Keramidias, J. Vollaie, R. Boisgard, G. Pottier, E. Rustique, F. Mittler, F. Navarro, J. Boutet, J.-L. Coll, I. Texier, LipImage™ 815: novel dye-

- loaded lipid nanoparticles for long-term and sensitive *in vivo* near-infrared fluorescence imaging, *J. Biomed. Opt.* 18 (2013) 101311. <https://doi.org/10.1117/1.JBO.18.10.101311>.
- [147] A. S. Klymchenko, E. Roger, N. Anton, H. Anton, I. Shulov, J. Vermot, Y. Mely, T. F. Vandamme, Highly lipophilic fluorescent dyes in nano-emulsions: towards bright non-leaking nano-droplets, *RSC Adv.* 2 (2012) 11876–11886. <https://doi.org/10.1039/C2RA21544F>.
- [148] C.M. Maguire, K. Sillence, M. Roesslein, C. Hannell, G. Suarez, J.-J. Sauvain, S. Capracotta, S. Contal, S. Cambier, N. El Yamani, M. Dusinska, A. Dybowska, A. Vennemann, L. Cooke, A. Haase, A. Luch, M. Wiemann, A. Gutleb, R. Korenstein, M. Riediker, P. Wick, P. Hole, A. Prina-Mello, Benchmark of Nanoparticle Tracking Analysis on Measuring Nanoparticle Sizing and Concentration, *J. Micro Nano-Manuf.* 5 (2017). <https://doi.org/10.1115/1.4037124>.
- [149] P. Hole, K. Sillence, C. Hannell, C.M. Maguire, M. Roesslein, G. Suarez, S. Capracotta, Z. Magdolenova, L. Horev-Azaria, A. Dybowska, L. Cooke, A. Haase, S. Contal, S. Manø, A. Vennemann, J.-J. Sauvain, K.C. Staunton, S. Anguissola, A. Luch, M. Dusinska, R. Korenstein, A.C. Gutleb, M. Wiemann, A. Prina-Mello, M. Riediker, P. Wick, Interlaboratory comparison of size measurements on nanoparticles using nanoparticle tracking analysis (NTA), *J. Nanoparticle Res.* 15 (2013) 2101. <https://doi.org/10.1007/s11051-013-2101-8>.
- [150] F. Caputo, A. Arnould, M. Bacia, W.L. Ling, E. Rustique, I. Texier, A.P. Mello, A.-C. Couffin, Measuring Particle Size Distribution by Asymmetric Flow Field Flow Fractionation: A Powerful Method for the Preclinical Characterization of Lipid-Based Nanoparticles, *Mol. Pharm.* 16 (2019) 756–767. <https://doi.org/10.1021/acs.molpharmaceut.8b01033>.
- [151] C.A. Schneider, W.S. Rasband, K.W. Eliceiri, NIH Image to ImageJ: 25 years of image analysis, *Nat. Methods.* 9 (2012) 671–675. <https://doi.org/10.1038/nmeth.2089>.
- [152] T. Nagy-Simon, M. Potara, A.-M. Craciun, E. Licarete, S. Astilean, IR780-dye loaded gold nanoparticles as new near infrared activatable nanotheranostic agents for simultaneous photodynamic and photothermal therapy and intracellular tracking by surface enhanced resonant Raman scattering imaging, *J. Colloid Interface Sci.* 517 (2018) 239–250. <https://doi.org/10.1016/j.jcis.2018.02.007>.

- [153] D.B. Warheit, W.J. Brock, K.P. Lee, T.R. Webb, K.L. Reed, Comparative Pulmonary Toxicity Inhalation and Instillation Studies with Different TiO₂ Particle Formulations: Impact of Surface Treatments on Particle Toxicity, *Toxicol. Sci.* 88 (2005) 514–524. <https://doi.org/10.1093/toxsci/kfi331>.
- [154] J. Liu, Y. Kang, S. Yin, B. Song, L. Wei, L. Chen, L. Shao, Zinc oxide nanoparticles induce toxic responses in human neuroblastoma SHSY5Y cells in a size-dependent manner, *Int. J. Nanomedicine.* 12 (2017) 8085–8099. <https://doi.org/10.2147/IJN.S149070>.
- [155] J.S. Tsuji, A.D. Maynard, P.C. Howard, J.T. James, C. Lam, D.B. Warheit, A.B. Santamaria, Research Strategies for Safety Evaluation of Nanomaterials, Part IV: Risk Assessment of Nanoparticles, *Toxicol. Sci.* 89 (2006) 42–50. <https://doi.org/10.1093/toxsci/kfi339>.
- [156] J.J. Li, S. Muralikrishnan, C.-T. Ng, L.-Y.L. Yung, B.-H. Bay, Nanoparticle-induced pulmonary toxicity, *Exp. Biol. Med.* 235 (2010) 1025–1033. <https://doi.org/10.1258/ebm.2010.010021>.
- [157] E.C. Costa, D. de Melo-Diogo, A.F. Moreira, M.P. Carvalho, I.J. Correia, Spheroids Formation on Non-Adhesive Surfaces by Liquid Overlay Technique: Considerations and Practical Approaches, *Biotechnol. J.* 13 (2018) 1700417. <https://doi.org/10.1002/biot.201700417>.
- [158] J.M. Lee, D.Y. Park, L. Yang, E.-J. Kim, C.D. Ahrberg, K.-B. Lee, B.G. Chung, Generation of uniform-sized multicellular tumor spheroids using hydrogel microwells for advanced drug screening, *Sci. Rep.* 8 (2018) 1–10. <https://doi.org/10.1038/s41598-018-35216-7>.
- [159] J.W. Dobrucki, D. Feret, A. Noatynska, Scattering of Exciting Light by Live Cells in Fluorescence Confocal Imaging: Phototoxic Effects and Relevance for FRAP Studies, *Biophys. J.* 93 (2007) 1778–1786. <https://doi.org/10.1529/biophysj.106.096636>.
- [160] M. Arık, N. Çelebi, Y. Onganer, Fluorescence quenching of fluorescein with molecular oxygen in solution, *J. Photochem. Photobiol. Chem.* 170 (2005) 105–111. <https://doi.org/10.1016/j.jphotochem.2004.07.004>.
- [161] J.R. Lakowicz, G. Weber, Quenching of Fluorescence by Oxygen. A Probe for Structural Fluctuations in Macromolecules, *Biochemistry.* 12 (1973) 4161–4170. <https://doi.org/10.1021/bi00745a020>.

- [162] A.K.O. Åslund, R.J. Vandebriel, F. Caputo, W.H. de Jong, C. Delmaar, A. Hyldbakk, E. Rustique, R. Schmid, S. Snipstad, I. Texier, K. Vernstad, S.E.F. Borgos, A comparative biodistribution study of polymeric and lipid-based nanoparticles, *Drug Deliv. Transl. Res.* 12 (2022) 2114–2131. <https://doi.org/10.1007/s13346-022-01157-y>.
- [163] A. Ahmed-Cox, A.M. Macmillan, E. Pandzic, R.M. Whan, M. Kavallaris, Application of Rapid Fluorescence Lifetime Imaging Microscopy (RapidFLIM) to Examine Dynamics of Nanoparticle Uptake in Live Cells, *Cells.* 11 (2022) 642. <https://doi.org/10.3390/cells11040642>.
- [164] K. Ehrlich, T.R. Choudhary, M. Ucuncu, A. Megia-Fernandez, K. Harrington, H.A.C. Wood, F. Yu, D. Choudhury, K. Dhaliwal, M. Bradley, M.G. Tanner, Time-Resolved Spectroscopy of Fluorescence Quenching in Optical Fibre-Based pH Sensors, *Sensors.* 20 (2020) 6115. <https://doi.org/10.3390/s20216115>.
- [165] H. Brismar, O. Trepte, B. Ulfhake, Spectra and fluorescence lifetimes of lissamine rhodamine, tetramethylrhodamine isothiocyanate, texas red, and cyanine 3.18 fluorophores: influences of some environmental factors recorded with a confocal laser scanning microscope., *J. Histochem. Cytochem.* 43 (1995) 699–707. <https://doi.org/10.1177/43.7.7608524>.
- [166] K. Suhling, L.M. Hirvonen, J.A. Levitt, P.-H. Chung, C. Tregidgo, A. Le Marois, D.A. Rusakov, K. Zheng, S. Ameer-Beg, S. Poland, S. Coelho, R. Henderson, N. Krstajic, Fluorescence lifetime imaging (FLIM): Basic concepts and some recent developments, *Med. Photonics.* 27 (2015) 3–40. <https://doi.org/10.1016/j.medpho.2014.12.001>.
- [167] E. Villatoro, L. Muñoz-Rugeles, J. Durán-Hernández, B. Salcido-Santacruz, N. Esturau-Escofet, J. G. López-Cortés, M. Carmen Ortega-Alfaro, J. Peón, Two-photon induced isomerization through a cyaninic molecular antenna in azo compounds, *Chem. Commun.* 57 (2021) 3123–3126. <https://doi.org/10.1039/D0CC08346A>.
- [168] J.A. Levitt, P.-H. Chung, K. Suhling, Spectrally resolved fluorescence lifetime imaging of Nile red for measurements of intracellular polarity, *J. Biomed. Opt.* 20 (2015) 096002. <https://doi.org/10.1117/1.JBO.20.9.096002>.
- [169] M.M.G. Krishna, Excited-State Kinetics of the Hydrophobic Probe Nile Red in Membranes and Micelles, *J. Phys. Chem. A.* 103 (1999) 3589–3595. <https://doi.org/10.1021/jp984620m>.

- [170] K. Bruun, C. Hille, Study on intracellular delivery of liposome encapsulated quantum dots using advanced fluorescence microscopy, *Sci. Rep.* 9 (2019) 10504. <https://doi.org/10.1038/s41598-019-46732-5>.
- [171] E. Sulheim, H. Baghirov, E. von Haartman, A. Bøe, A.K.O. Åslund, Y. Mørch, C. de L. Davies, Cellular uptake and intracellular degradation of poly(alkyl cyanoacrylate) nanoparticles, *J. Nanobiotechnology.* 14 (2016) 1. <https://doi.org/10.1186/s12951-015-0156-7>.
- [172] A. Cser, K. Nagy, L. Biczók, Fluorescence lifetime of Nile Red as a probe for the hydrogen bonding strength with its microenvironment, *Chem. Phys. Lett.* 360 (2002) 473–478. [https://doi.org/10.1016/S0009-2614\(02\)00784-4](https://doi.org/10.1016/S0009-2614(02)00784-4).
- [173] M.Y. Berezin, S. Achilefu, Fluorescence Lifetime Measurements and Biological Imaging, *Chem. Rev.* 110 (2010) 2641–2684. <https://doi.org/10.1021/cr900343z>.
- [174] J.V. Frangioni, In vivo near-infrared fluorescence imaging, *Curr. Opin. Chem. Biol.* 7 (2003) 626–634. <https://doi.org/10.1016/j.cbpa.2003.08.007>.
- [175] V. Ntziachristos, C. Bremer, R. Weissleder, Fluorescence imaging with near-infrared light: new technological advances that enable in vivo molecular imaging, *Eur. Radiol.* 13 (2003) 195–208. <https://doi.org/10.1007/s00330-002-1524-x>.
- [176] S.L. Gibbs, Near infrared fluorescence for image-guided surgery, *Quant. Imaging Med. Surg.* 2 (2012) 177–187. <https://doi.org/10.3978/j.issn.2223-4292.2012.09.04>.
- [177] Q. Cabon, D. Sayag, I. Texier, F. Navarro, R. Boisgard, D. Virieux-Watrelet, F. Ponce, C. Carozzo, Evaluation of intraoperative fluorescence imaging-guided surgery in cancer-bearing dogs: a prospective proof-of-concept phase II study in 9 cases, *Transl. Res.* 170 (2016) 73–88. <https://doi.org/10.1016/j.trsl.2015.12.001>.
- [178] S. Keereweer, J.D.F. Kerrebijn, P.B.A.A. van Driel, B. Xie, E.L. Kaijzel, T.J.A. Snoeks, I. Que, M. Hutteman, J.R. van der Vorst, J.S.D. Mieog, A.L. Vahrmeijer, C.J.H. van de Velde, R.J. Baatenburg de Jong, C.W.G.M. Löwik, Optical Image-guided Surgery—Where Do We Stand?, *Mol. Imaging Biol.* 13 (2011) 199–207. <https://doi.org/10.1007/s11307-010-0373-2>.
- [179] B.E. Schaafsma, J.S.D. Mieog, M. Hutteman, J.R. van der Vorst, P.J.K. Kuppen, C.W.G.M. Löwik, J.V. Frangioni, C.J.H. van de Velde, A.L. Vahrmeijer, The clinical use of indocyanine green as a near-infrared fluorescent contrast agent for image-

guided oncologic surgery, *J. Surg. Oncol.* 104 (2011) 323–332. <https://doi.org/10.1002/jso.21943>.

- [180] J.R. van der Vorst, A.L. Vahrmeijer, M. Hutteman, T. Bosse, V.T. Smit, C.J. van de Velde, J.V. Frangioni, B.A. Bonsing, Near-infrared fluorescence imaging of a solitary fibrous tumor of the pancreas using methylene blue, *World J. Gastrointest. Surg.* 4 (2012) 180–184. <https://doi.org/10.4240/wjgs.v4.i7.180>.
- [181] S.A. Dilliard, D.J. Siegwart, Passive, active and endogenous organ-targeted lipid and polymer nanoparticles for delivery of genetic drugs, *Nat. Rev. Mater.* 8 (2023) 282–300. <https://doi.org/10.1038/s41578-022-00529-7>.

Appendix A

1. A.1 – Text file to Tiff Image (Intensity and Lifetime)

```
# -*- coding: utf-8 -*-
```

```
"""
```

```
Created on Fri Aug 19 06:49:07 2022
```

```
"""
```

```
from pylab import *
```

```
import os
```

```
from PIL import Image
```

```
close('all')
```

```
folder = r'C:\Users\fumcg\Dropbox\PhD\Experimental\PhD Data\Live  
Cell\FCS\Images' # the folder which contains the .dat files
```

```
files = [n for n in os.listdir(folder) if n.endswith('.dat') if n.count('.')==1] # finds the  
.dat files in the folder
```

```
for file in files:
```

```
    data=[]
```

```
    data_intens=[]
```

```
    data_lifetime=[]
```

```

with open(folder+'\\'+file) as f:

for i, line in enumerate(f):

    line = line.strip()

    data.append(line)

if line == 'Intens..':

    intens_start = i+1

if line == 'Aver. LT.':

    lifetime_start = i+1

    intens_end = i

lifetime_end = i

for line in data[intens_start:intens_end]:

    data_intens.append([int(float(n)) for n in line.split()])

data_intens = array(data_intens)

data_intens = data_intens.astype('uint16')

print(folder, '\t', file, '\t', data_intens.min(), '\t', data_intens.max())

im = Image.fromarray(data_intens)

```

```
im.save(folder+'\\'+file[:-4]+'_'+'.join(folder.split('\\')[-3:])+'_INT_'+str(data_intens.min())+'_'+str(data_intens.max())+'.tiff')
```

```
for line in data[lifetime_start:]:
```

```
    data_lifetime.append([float(n) for n in line.split()])
```

```
data_lifetime = array(data_lifetime)
```

```
im = Image.fromarray(data_lifetime)
```

```
im.save(folder+'\\'+file[:-4]+'_'+'.join(folder.split('\\')[-3:])+'_LT'+'.tiff')
```

2. A.2 – Image Stitcher

```
# -*- coding: utf-8 -*-
```

```
"""
```

```
Created on Sun Aug 21 08:55:54 2022
```

```
"""
```

```
from pylab import *
```

```
import os
```

```
import PublicationFigures as pf
```

```
from PIL import Image
```

```
import matplotlib.patches as patches
```

```
import openpyxl
```

```
close('all')
```

```
# COPY PATH
```

```
xls_file = r"C:\Users\fumcg\Desktop\730 - Analysis\fumcg_Desktop_730 -  
Coords.xlsx" # The Excel file containing the image coordinates
```

```
# COPY PATH
```

```
image_path = r"C:\Users\fumcg\Desktop\730"# the RAW images with the ACTUAL  
intensity values
```

```
im_width = 300 # pixels
```

```
im_height = 300 # pixels
```

```
#####
```

```

# Extract the coordinate data from the Excel File

#*****

wb = openpyxl.load_workbook(xls_file)

ws = wb.active

data = []

for i in range(0, ws.max_row):

    store = []

    for col in ws.iter_cols(1, ws.max_column):

        store.append(col[i].value)

    if None not in store:

        data.append(store)

im_list = []

x_coord = []

y_coord = []

for line in data[1:]:

    im_list.append(line[0])

    x_coord.append(int(line[1]))

    y_coord.append(int(line[2]))

```

```

#*****
x_coord = array(x_coord)+min(x_coord)*(-1) # the x-coordinates of the reference
point on each image

y_coord = array(y_coord)+min(y_coord)*(-1)+im_height # the y-coordinates of the
refernce point on each image

im_list = [image_path+'\\'+n for n in im_list] # List of images that will be imported

x_range = (min(x_coord), max(x_coord)+300) # start and end of the width of the image
y_range = (min(y_coord), max(y_coord)+300) # start and end of the height of the image

x_dim = x_range[1]-x_range[0] # total width of the image canvas
y_dim = y_range[1]-y_range[0] # total height of the iamge canvas

y_coord = y_dim-y_coord # invert the y coordinate dimension to account for 0 being at
the top of the image

I = zeros((y_dim, x_dim), dtype='uint16') # the canvas on to which the individual
images will be positioned

# Images positioned on the canvas image

for i, v in enumerate(im_list):

    img = Image.open(v)

```



```

img = asarray(img)

I[y_coord[i]:y_coord[i]+im_height, x_coord[i]:x_coord[i]+im_width] = img

In = Image.fromarray(I) # convert the numpy array back into a 16 bit image

In.save(xls_file.replace(' - Coords.xlsx', '.tiff')) # Name of Exported Image

#*****

# Plot the individual images on the canvas for tracing

#*****

fig, ax = subplots()

pf.pos()

ax.imshow(flipud(In), cmap='gray')

ax.invert_yaxis()

ax.set_xlim(0, x_dim)

ax.set_ylim(0, y_dim)

colors = ['r', 'g', 'b', 'c', 'm', 'y']

n = 0

for i in range(len(x_coord)):

```

```
rect = patches.Rectangle((x_coord[i], y_dim-y_coord[i]-im_height), im_width,
im_height, linewidth=1, edgecolor=colors[n], facecolor='none')
```

```
ax.add_patch(rect)
```

```
ax.plot(x_coord[i], y_dim-y_coord[i]-im_height, color=colors[n], marker='.')
```

```
ax.text(x_coord[i], y_dim-y_coord[i]-im_height, f'({x_coord[i]}, {y_dim-y_coord[i]-
im_height})', color=colors[n])
```

```
ax.text(x_coord[i]+im_width/2, y_dim-y_coord[i]-im_height+im_height/2,
im_list[i].split('\\')[1],
```

```
color=colors[n], ha='center', va='center', rotation=-45)
```

```
n += 1
```

```
if n > (len(colors)-1):
```

```
n = 0
```

```
*****
```